

6240

}

An Experimental Study of Passive Control of Hypersonic Cavity Flow Oscillations

Final Report for the Period October 1, 1994 - September 30, 1997
Grant F49620-95-1-0001

Approved for public release,
Distribution unlimited

D.S. Dolling, S.W. Perng and Y.L. Leu

Center for Aeromechanics Research, WRW 220
Department of Aerospace Engineering & Engineering Mechanics
The University of Texas at Austin
Austin, Texas 78712-1085
Telephone: (512) 471-4596
Fax: (512) 471-1730
e-mail: ddolling@mail.utexas.edu

Approved for public release,
Distribution unlimited

REPORT DOCUMENTATION PAGE

Public reporting burden for this collection of information is estimated to average 1 hour per response, including the time to data needed, and completing and reviewing this collection of information. Send comments regarding this burden estimate to Washington Headquarters Services, Directorate for Information Operations and Reports, 1215 Jefferson L. and Budget, Paperwork Reduction Project (0704-0188), Washington, DC 20503.

0240
Sustaining the
is for reducing
of Management

1. AGENCY USE ONLY (Leave blank)	2. REPORT DATE	3. REPORT TYPE AND DATES COVERED	
	March 1, 1998	Final (1 Oct 94 - 30 Sep 97)	
4. TITLE AND SUBTITLE		5. FUNDING NUMBERS	
An Experimental Study of Passive Control of Hypersonic Cavity Flow Oscillations		G F49620-95-1-1001	
6. AUTHOR(S)		8. PERFORMING ORGANIZATION REPORT NUMBER	
D.S. Dolling, S.W. Perng & Y.L. Leu		none assigned	
7. PERFORMING ORGANIZATION NAME(S) AND ADDRESS(ES)		9. SPONSORING / MONITORING AGENCY NAME(S) AND ADDRESS(ES)	
Dept. of Aerospace Engineering & Engineering Mechanics The University of Texas at Austin Austin, Texas 78712-1085		10. SPONSORING / MONITORING AGENCY REPORT NUMBER	
11. SUPPLEMENTARY NOTES		12a. DISTRIBUTION / AVAILABILITY STATEMENT	
none		Available to public	
13. ABSTRACT (Maximum 200 Words)		12b. DISTRIBUTION / AVAILABILITY STATEMENT	
An experimental study of open cavity flow has been made in a high Reynolds number, Mach 5 turbulent boundary layer. The majority of measurements made were of fluctuating wall pressures. The objectives were: (i) examine how effective changes in front and rear wall geometry were at attenuating the pressure oscillations, (ii) explore how impingement of a shock wave (variable strength and position) affected the cavity flow and (iii) how stores (different geometries and positions) affected the cavity flow. In addition, techniques which were judged effective at attenuating pressure oscillations for the empty cavity were used with shock impingement and with stores in order to explore their effectiveness under perturbed flow conditions.		Approved for public release, distribution unlimited	
14. SUBJECT TERMS		15. NUMBER OF PAGES	
Turbulent High Speed Cavity flow, passive control, pressure oscillations, influence of stores.		16. PRICE CODE	
17. SECURITY CLASSIFICATION OF REPORT UNCLASSIFIED		18. SECURITY CLASSIFICATION OF THIS PAGE UNCLASSIFIED	
19. SECURITY CLASSIFICATION OF ABSTRACT UNCLASSIFIED		20. LIMITATION OF ABSTRACT	

NSN 7540-01-280-5500

19980317118
DTIC QUALITY INSPECTED 2
Standard Form 298 (Rev. 2-89)
Prescribed by ANSI Std. Z39-18
200-102

An Experimental Study of Passive Control of Hypersonic Cavity Flow Oscillations

Final Report for the Period October 1, 1994 - September 30, 1997
Grant F49620-95-1-0001

D.S. Dolling, S.W. Perng and Y.L. Leu

Center for Aeromechanics Research, WRW 220

Department of Aerospace Engineering & Engineering Mechanics

The University of Texas at Austin

Austin, Texas 78712-1085

Telephone: (512) 471-4596

Fax: (512) 471-1730

e-mail: ddolling@mail.utexas.edu

Executive Summary

An experimental study of open cavity flow has been made in a high Reynolds number, Mach 5 turbulent boundary layer. The majority of measurements made were of fluctuating wall pressures. The objectives were: (i) examine how effective changes in front and rear wall geometry were at attenuating the pressure oscillations, (ii) explore how impingement of a shock wave (variable strength and position) affected the cavity flow and (iii) how stores (different geometries and positions) affected the cavity flow. In addition, techniques which were judged effective at attenuating pressure oscillations for the empty cavity were used with shock impingement and with stores in order to explore their effectiveness under perturbed flow conditions.

The results show that vented and slotted walls, and spoilers are ineffective. A "3-D" rear wall (swept in both planes and symmetric about the center-line) attenuated the strongest oscillations by factors of up to 7 compared to the baseline rectangular cavity. Regardless of shock impingement position, shock strength, store position, store dimensions, store to cavity volume ratio and asymmetric store arrangement the cavity oscillation frequencies remain essentially unchanged. Based on the mean and rms pressure distributions (whose magnitude varies substantially but whose basic shape does not change significantly) and surface flow patterns it appears that the essential flow structure also remains largely unchanged. These similarities suggest that control techniques developed for the empty cavity flow should be effective with shock impingement or store-release. Tests using two "passive control" rear walls in perturbed cavity flow support this conclusion.

Table of Contents

Executive Summary

1	Introduction.....	1
1.1	Background	
1.2	Objectives	
1.3	Reporting of Results	
1.4	Final Report Format	
2	Experimental Program.....	5
2.1	Wind Tunnel and Flow Conditions	
2.2	Models	
2.2.1	Baseline Cavity Model	
2.2.2	Passive Control Geometries	
2.2.3	Boundary Layer Spoilers	
2.2.4	Shock Generators	
2.2.5	Store Models	
2.2.6	Block Inserts	
2.3	Instrumentation and Data Acquisition	
2.4	Flow Visualization	
2.5	Test Program	
2.6	Uncertainty	
3	Baseline Cavity Oscillation Investigation	27
3.1	Mean Pressure and Standard Deviation Distributions	
3.2	Surface Flow Patterns and Cavity Flow Structure	
3.3	General Power Spectra Characteristics	
3.4	Effect of the Cavity Length/Depth	
3.5	Compressibility Effect on the Shear Layer	
3.6	Impingement Shock Detection	
3.7	Acoustic Wave and Model of Oscillation Prediction	
4	Passive Control Investigation.....	60
4.1	Effects of Changes in Front Wall Geometry	
4.2	Effects of Changes in Rear Wall Geometry	
4.3	Effects of Incoming Boundary layer Spoilers	
4.4	Effects of an Internal Obstacle	
4.5	Scale-Up Discussion	
5	Shock/Cavity Interaction.....	84
5.1	Surface Flow Visualization	
5.2	Mean Pressure and Pressure Standard Deviation	
5.3	Mode Frequencies	
5.4	Changing Shock Strength	
5.5	Summarizing Remarks	

6	Store/Cavity Interaction	100
6.1	Surface Flow Visualization	
6.2	Mean Pressure and Pressure Standard Deviation	
6.3	Mode Frequencies	
6.4	More Discussion on Store Position	
6.5	Summarizing Remarks	
7	Passive Control for Perturbed Cases	114
7.1	Surface Flow Visualization	
7.2	Mean Pressure and Standard Deviation	
7.3	Power Spectra	
7.4	Summarizing Remarks	
8	Concluding Remarks	127

References

1. INTRODUCTION

1.1 Background

Internal carriage of weapons and stores offers many benefits for transonic and supersonic fighter/bomber aircraft. These benefits include elimination of weapon aerodynamic heating, reduction of aircraft aerodynamic drag and radar signature greater maneuverability and enlarged flight envelope. The reduction in radar signature is particularly important since "stealth" gives the advantage of surprise and enhances survivability of the parent aircraft. Stealth warplanes such as the F-117 "Nighthawk" and B-2 "Spirit" are already in the US military aircraft inventory and stealth is a key element of future aircraft such as the F-22 "Raptor". Currently there is interest in the USAF in releasing weapons/stores from aircraft flying at supersonic speeds. Eliminating the need to decelerate to high subsonic or transonic speeds for weapons release reduces time-over-target and enhances survivability. Due to the complex fluid dynamics of weapons bay (cavity) flows, designing weapons bays poses severe challenges.

Extensive analytical, experimental; and computational studies over the past forty years have shown that air flow past cavities, such as aircraft weapons bays, can induce intense self-sustaining pressure fluctuations in and around the cavities. These pressure fluctuations consist of broadband small amplitude pressure oscillations as well as discrete large amplitude resonances which can, in turn, excite vibration of the local bay structure or the store components inside the bay. This can result in instrumentation failure and structural fatigue, damage to the stores and can increase aerodynamic loading of the aircraft. It may also have detrimental effects of the stable release of weapons and their trajectories. The peak pressure levels inside the cavity can be very high. From preliminary experiments in the current study, for an empty cavity with its length-to-depth ratio equal to 3 and at a freestream Mach number equal to 5, it was found that although the mean pressure on the rear cavity floor is only about 64% higher than the freestream static pressure, the peak pressure levels can be as high as 2.3 times $\overline{P_\infty}$.

While the oscillation frequencies may be roughly predicted by the semi-empirical formula initially proposed by Rossiter (1964) and subsequently improved by Heller et. al. (1975), no simple analytic or empirical formulae or computational method can predict the associated amplitude of the fluctuating pressure. With the present interest in releasing stores at supersonic speeds, a better understanding of the high speed flow

inside and around a cavity is necessary. In particular, since high amplitude loads are a natural feature of cavity flow, methods also need to be developed to suppress the flow oscillations. Some introductory comments on "control" are made in the following section and several control techniques tested by previous researchers are discussed in greater detail in Perng (1996). Further, in spite of a considerable number of earlier works to understand various aspects of the flow behavior and pressure fluctuations in empty cavities, there is very little information on how a projectile emerging from a high speed cavity affects the flow dynamics and loading. It is this subject that motivates the current study.

1.2 Objectives

The objectives of this study can be considered in two inter-related parts.

a) Part 1:

- (i) understand the flow structure and dynamics of the Mach 5 "baseline" cavity flow. [Here "baseline" means an empty cavity with rectangular walls for which the flow is of the "open" type. "Open" means that the shear layer bridges the cavity - this is the type most often found in applications].
- (ii) explore the effectiveness of passive control techniques (front and rear wall geometry changes) on attenuating the amplitude of the cavity pressure oscillations.

b) Part 2:

In part 2 of the study the primary focus was on examining the effects of "perturbations" (impinging shock waves, stores in the cavity) on the cavity flow structure and dynamics. Specifically:

- (i) how is the flow structure and feedback process in an empty cavity flow altered by the presence of a generic store on the cavity centerline or by the impingement of a 2-D shock wave?
- (ii) how effective are the passive control techniques developed for the empty cavity flow when a store is on the cavity centerline or when a 2-D shock wave impinges on the cavity.

Two additional questions have also been addressed:

- (iii) how is the flow structure/dynamics affected by asymmetrical store arrangements and,

(iv) how does store diameter, length and volume (relative to cavity volume) affect the flow structure/dynamics.

1.3 Reporting of Results:

To date the results of this work have been reported in two doctoral dissertations and three papers presented at national/international Technical Conferences. The results of part 1 appear primarily in References 1-3 below, while those of Part 2 appear in Refs 4 and 5.

1. Perng, S.W., "Passive Control of Pressure Oscillations in Hypersonic Cavity Flow," Ph.D. Dissertation, Dept. of Aerospace Engineering and Engineering Mechanics, The University of Texas at Austin, Austin, TX, Dec. 1996.
2. Perng, S.W., and Dolling, D.S., "Passive Control of Pressure Oscillations in Hypersonic Cavity Flows", AIAA 96-0444, 34th Aerospace Sciences Meeting and Exhibit, Reno, NV, Jan. 1996.
3. Perng, S.W., and Dolling, D.S., "Attenuation of Pressure Oscillations in High Speed Cavity Flow through Geometry Changes," AIAA paper 97-1802, 28th Fluid Dynamics Conference, Snowmass, CO, June 20-July 2, 1997.
4. Leu, Y.L., "Experimental Study of Perturbed High Speed Cavity Flow", Ph.D. dissertation, Dept. of Aerospace Engineering and Engineering Mechanics, The University of Texas at Austin, Austin, TX Dec. 1997.
5. Leu, YL., and Dolling, D.S., "Passive Control of Pressure Oscillations in Cavity Flow with Store Release," paper No. 15, CEAS European Forum on Wind Tunnels and Wind Tunnel Test Techniques, Cambridge, UK., April 14-16, 1997.

Two articles for submission to archival journals, based on the work presented in the dissertations, are presently in preparation.

1.4 Final Report Format:

A very large volume of work was carried out under the present grant. Although the grant provided support for one graduate research assistant, two worked on the project. One of them, Dr. S.W. Perng, was funded privately by the Taiwanese government. Because of this, additional experiments were carried out, beyond the original, anticipated scope of the project. All of these results cannot be presented in this Final Report. The Report focuses on a description of the experiments themselves and the most significant results. For a detailed discussion of the mean and unsteady characteristics of cavity flowfields, physics of the self sustaining oscillation, factors

which influence cavity flows, and techniques which influence the oscillation amplitudes the reader is referred to the Literature Review provided in Perng's dissertation (1996). For a review of the effects of perturbations on cavity flowfields, including impinging shocks and stores, the reader is referred to Leu's dissertation (1997).

2. EXPERIMENTAL PROGRAM

2.1 Wind Tunnel and Flow Conditions:

The high Reynolds number, Mach 5 tunnel has a test section which is 6 inch wide by 7 inch high and 30 inch long with two removable side doors to allow access. A total of about 140 ft³ of air at a pressure of about 2500 psia is provided by a Worthington HB4 four-stage compressor and is stored in external tanks. The compressed air supply provides a run time up to about 70 secs for the test conditions of the current program. Upstream of the stagnation chamber, the air is heated by two 420 kW nichrome wire resistive heaters to increase the total temperature. The total temperature is monitored with a J-type thermocouple inserted into the flow in the plenum section. The stagnation chamber pressure and temperature for these initial experiments were approximately 332 ± 2 psia and 643 ± 7 °R respectively. About 20 seconds after start-up, the flow inside the tunnel becomes stable.

The incoming turbulent BL underwent natural transition and developed under approximately adiabatic wall temperature conditions. The nominal properties of the incoming free-stream flow and some basic quantities of the undisturbed turbulent boundary layer on the tunnel centerline are given in Table 3.1. The displacement thickness, δ^* , and momentum deficit thickness, θ , were calculated from the calculated profiles of u/U_∞ and ρ/ρ_∞ obtained from pitot surveys assuming an adiabatic wall and constant static pressure ($P(y) = P_\infty$) conditions. The skin friction coefficient, C_f , and the wake strength, Π , were obtained from fits u^+ vs y^+ of the velocity profile to the law of the wall-law of the wake.

M_∞	4.95	4.95
U_∞	765 m/s	2509 ft/s
Re_∞	$50 \times 10^6 / m$	$15.24 \times 10^6 / ft$
Re_θ	3.8×10^4	3.8×10^4
P_0	$2.275 \times 10^6 N/m^2$	332 psia
T_0	355 K	643 °R
δ	1.93 cm	0.76 in
δ^*	0.91 cm	0.36 in
θ	0.076 cm	0.030 in
$H = \delta^*/\theta$	12	12
Π	0.44	0.44
C_f	7.6×10^{-4}	7.6×10^{-4}

Table 2.1 Incoming Flow Conditions

2.2 Models:

The cavity model was designed so that both the baseline flowfield and the effectiveness of the passive control methods could be investigated using common components.

2.2.1 Baseline Cavity Model:

The cavity model was designed in modular form primarily so that the rectangular upstream and downstream walls of the baseline case could be replaced rapidly and economically with different geometry FWs and RWs. The model shown in figure 2.1(a) consists of nine parts (one is not shown) plus two thrust bearings (not shown). The cavity floor (4) is 3 inch x 3 inch and 0.5 inch thick and the height of the surrounding walls (2, 3) is 1 inch. The ratio of L/H can be changed by using the large bolt (7) which can raise or lower the support (5) which is 3 inch x 3 inch and 1 in thick. A shallow empty space (3 inch x 2.2 inch x 0.5 inch) formed by the cavity floor (4) and the support (5) is reserved for mounting the pressure transducers which are about 0.6 inch to 0.8 inch long. After moving the cavity floor (4) to a particular position, the large bolt is then locked by the lock nut (8) as shown in figure 3.1(a). This allows changes of the ratio of L/H to be made from outside the wind tunnel. Alternatively, as was the case for this initial study, the floor position can be fixed at $H = 1$ inch and either the FW (2) or RW (3) removed.

The baseline cavity geometry, dimensions, and the coordinate system are shown schematically in figure 2.1(b). The origin of the coordinate system is on the cavity floor in the middle of the FW as shown in the figure. The length (L) can be varied from 3 inch to 5 inch whereas the width (W) is fixed at 3 inch. The depth (H) can also be adjusted and has a maximum value of 1 inch. In this study, measurements were made for three ratios of L/H, namely 3, 4, and 5. In most cases H was fixed at 1 inch. The longitudinal symmetry plane is at $z = 0$. The side walls are at $z = \pm W/2$. FW and RW refer to the walls at $x = 0$ and $x = L$ respectively. The available ranges of L/H, δ/H , and W/H are given in Table 2.2.

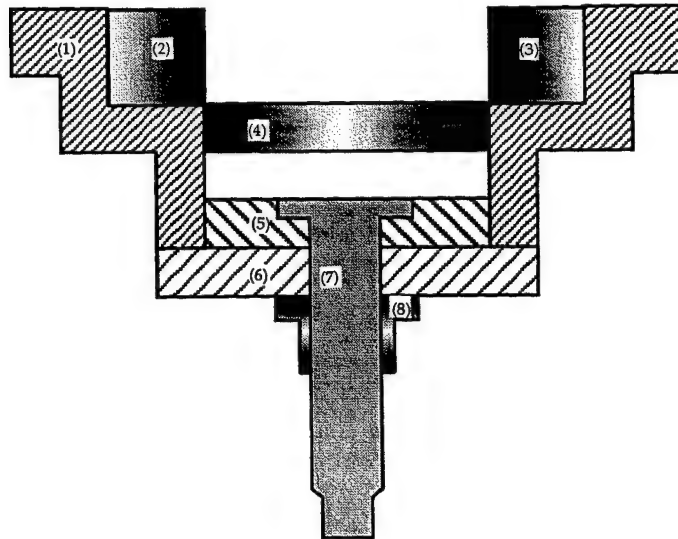


Figure 2.1(a) Modular Cavity Model

The mean and unsteady characteristics of the cavity floor pressure were measured by flush-mounted wall pressure transducers. These transducers were made by Kulite Semiconductor Company and will be described in detail in section 2.3. The distribution of Kulite transducer ports (33 in total) and their coordinates are shown in figure 2.1(c). In this study, the cavity flow was found to be symmetric about the centerline with the help of the flow visualization. All baseline and passive control investigations were discussed based on the centerline pressure measurements. Four, nineteen, and ten ports were machined on the FW, the cavity floor, and the RW respectively. Of the 19 ports on the floor, 8 were placed off centerline in order to examine the symmetric properties of the 3-D cavity flow.

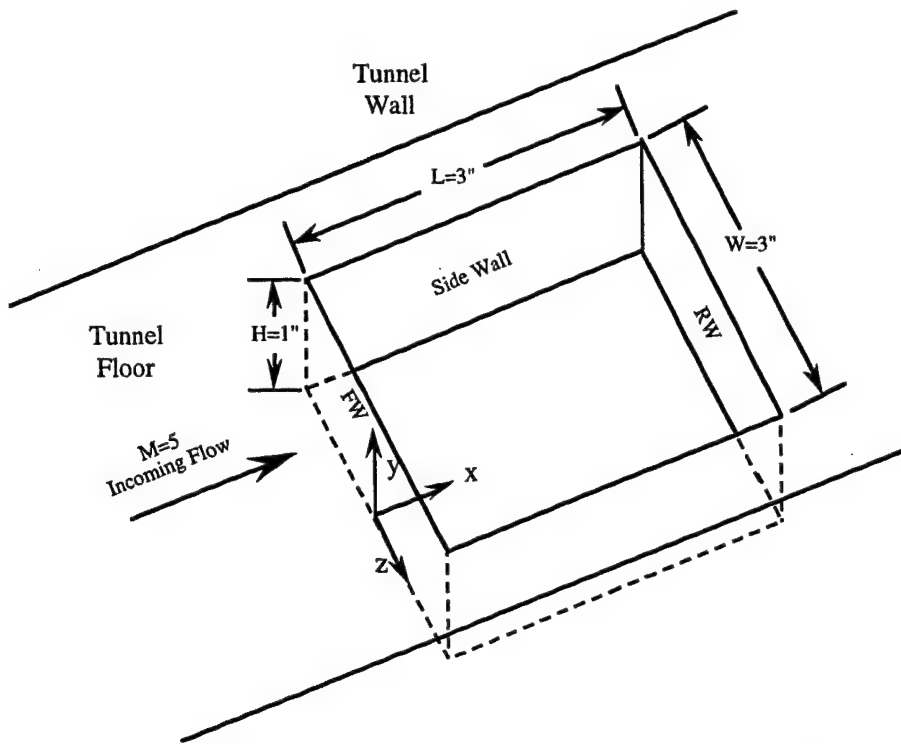


Figure 2.1(b) Cavity Geometry and Coordinate System

Factor	Range
L/H	≥ 3
δ/H	≥ 0.76
W/H	≥ 3

Table 2.2 Ranges of L/H , δ/H , and W/H

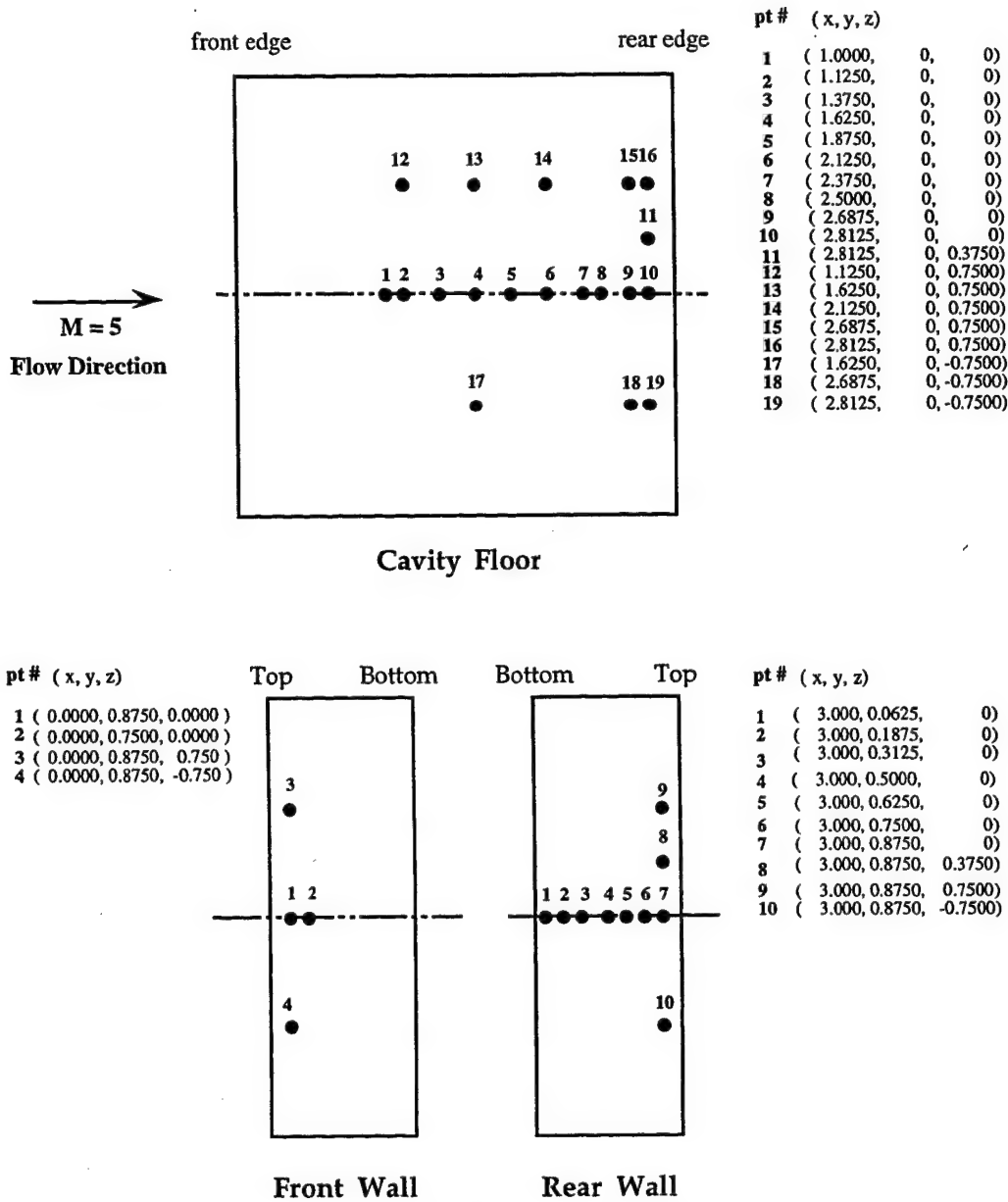


Figure 2.1(c) Kulite Ports and Their Coordinates

2.2.2 Passive Control Geometries:

Understanding the flow structure responsible for the pressure fluctuations and the feedback mechanism in the baseline cavity flow is important to understanding how to attenuate the strength of the self-sustaining oscillations. From the review of the literature, three major phenomena are believed to dominate the fluctuating pressure field inside the cavity, namely, (1) the trailing-edge vortex, (2) the SL impingement on the RW, and (3) the flow recompression near the RW corner/floor junction. These three phenomena are strongly linked and form an oscillation cycle. When the SL deflects downward below the top edge of the RW, there is an inflow of high-energy

external flow into the cavity, which causes a transient flow impingement and a shock wave near the trailing edge of the cavity. This shock wave/impingement “event” causes an acoustic (or compression) wave to propagate away from the impingement region towards the FW (Tam and Block, 1978). According to Rossiter (1964), such a forward going acoustic wave can induce shedding of a small vortex from the leading edge of the FW and this shedding vortex grows as it moves downstream. Due to the instability of the shedding vortex, the SL deflects upward and then downwards resulting in another shock/impingement event on the RW. In contrast, Heller and Bliss (1975) proposed that the reflection of the acoustic pressure wave off the FW rather than the shedding vortex deflected the SL up and down. However, in both models, the shock impingement event results in mass flow into the cavity which causes the generation of the acoustic wave and provides the energy required for the self-sustaining vortices. Therefore, in either case the RW plays a very important role. On the other hand, if Rossiter’s result is correct, the shedding vortex is one of the key factors. Therefore three kinds of attenuation techniques to control the pressure oscillation were examined: (1) changing the FW geometry, (2) changing the RW geometry, and (3) changing the incoming BL properties.

When changing the wall geometry, the external surfaces of the FW and RW were maintained parallel to the cavity floor in all cases since in applications (with bay doors in place) it is unlikely that the external surface would be indented or have protrusions. Seven walls were tested, namely (1) Vented Wall, (2) Slotted Wall, (3) “Beak” Wall, (4) “Valley” Wall, (5) Slanted Wall 1 (SW1) (6) Slanted Wall 2 (SW2), and (7) Slanted Wall 3 (SW3). Of these, the Beak Wall and Valley Wall (the terminology will be explained later) are geometrically 3-D walls and the others are all geometrically 2-D walls. They are described briefly below:

- (1) Vented Wall: This passive venting method, as shown in figure 2.2(a), represents an attempt to relieve the high pressure near the top of the RW. Earlier work on *open* cavity flow ($L/H < 10$) in which the SL flows over or bridges the cavity, had shown that the highest mean pressure and largest amplitude pressure fluctuations occurred near the top of the RW (Stallings and Wilcox, 1987 and Zhang and Edwards, 1992). With this geometry, a number of ducts are immersed in the RW. It was anticipated that the pressure difference between the upper part of the inside RW and the flow downstream of the RW edge should force a fraction of the high energy flow out of the

cavity through the vents. It was also believed that this might attenuate the strength of the acoustic wave and, then, stabilize the SL above the cavity.

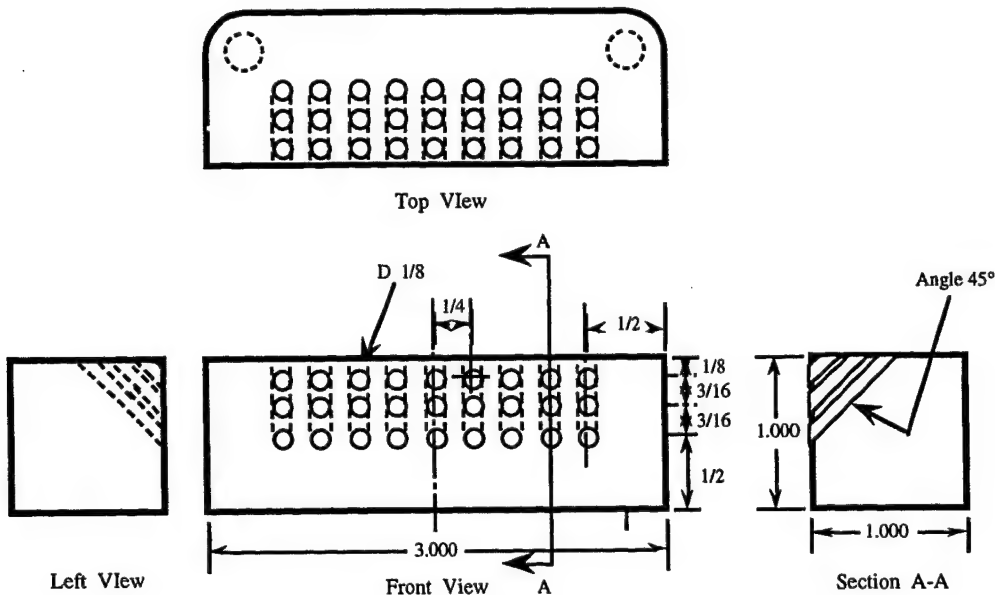


Figure 2.2(a) The Vented Wall

This vented wall has 27 small holes on its vertical face. This irregular surface shape should effect the generation of an acoustic wave or the reflection of an incoming acoustic wave. Because of the latter, this wall was tested as the FW also.

(2) Slotted Wall: The objective, as shown in figure 2.2(b), was to try to attenuate (or even eliminate) the generation of the forward-going acoustic wave which is the important source of inducing the instability of the SL above the cavity. Experiments by Shaw *et al* (1988) in supersonic cavity flow in which there was a slot in the RW for supporting an aircraft model suggested that such control might be feasible. Like the vented wall, the slotted wall has an irregular vertical surface that might interfere with the acoustic wave characteristics. On that basis it was anticipated that it might also interfere with the generation of the shedding vortex from the top edge of the FW, and was therefore also used as an FW.

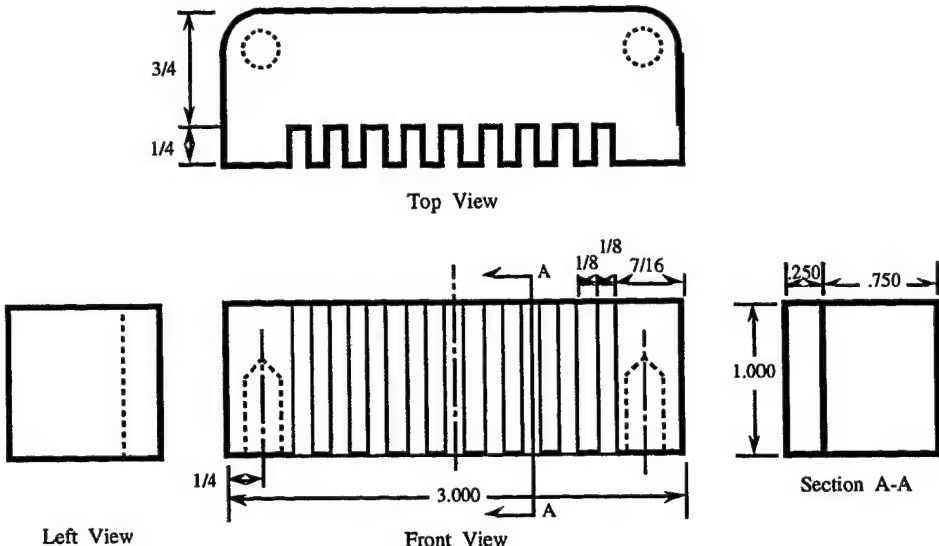


Figure 2.2(b) The Slotted Wall

(3) "Beak" Wall: This 3-D wall, as shown in figure 2.2(c), was designed to force the higher pressure air away from the center line and make it flow spanwise along the z direction. It is referred to as a "beak" because of the shape around the center part of the wall looks like a bird beak. For a regular cavity with rectangular walls Suhs (1987) and Rizzetta (1988) showed numerically the existence of symmetric lateral vortices which were generated upstream near the front top edges of the side walls ($x/L = 0.25$, $y/H = 1$, and $z/W = \pm 0.5$) and became bigger as they convected downstream. These lateral vortices might be induced by the pressure difference between the main free stream and the flow inside the cavity near both side walls. Owing to the side-wall friction on the flow impingement and lateral vortices, the impingement pressure around the side edges of the RW is lower than on center line. Due to the beak shape of the RW, the higher pressure flow should be swept along the 3-D slanted surface from the center portion to the lateral side-wall low-pressure regions and the impingement flow should be swept off the 3-D slanted surfaces. Since the edges of the beak RW are cut deeper than on centerline (see section A-A, figure 2.2(c)), this could also improve the performance of the slanted surface.

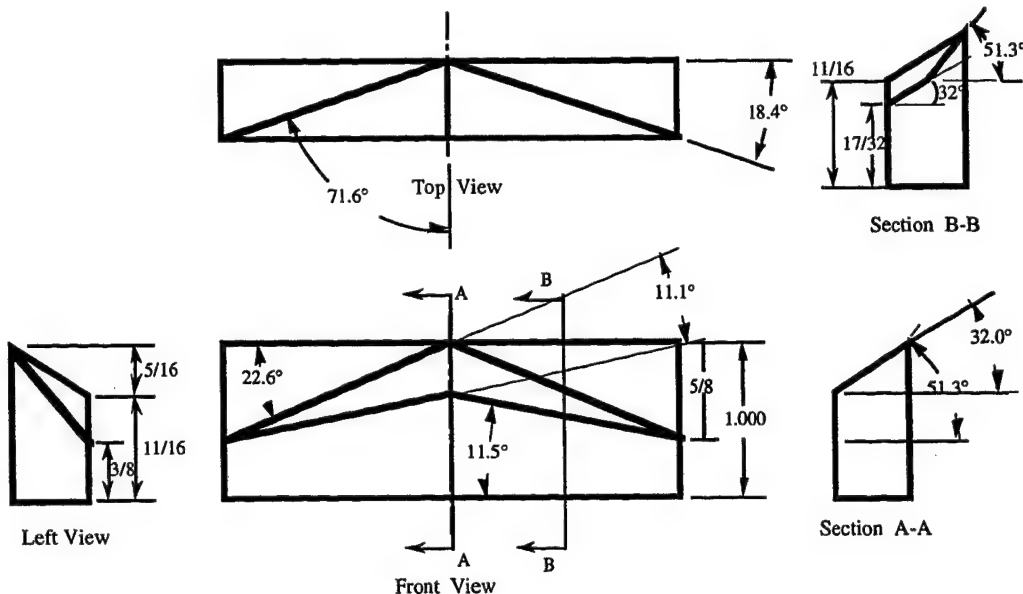


Figure 2.2(c) The Beak Wall

(4) "Valley" Wall: This idea, as shown in figure 2.2(d), evolved by considering the reverse geometry effect of the beak wall. The center line (see section A-A, figure 2.2(d)) of the valley wall was cut deeper than on the two edges (this is why it is named "valley") such that the impact flow is induced to move towards the centerline. Therefore the high energy flow after the impingement would be swept along the 3-D slanted surface from the lateral side-wall regions to the center portion. Beside the beak RW, the valley RW could be used to test which kinds of slanted surfaces and shape around the center part of the RW would be most effective for the attenuating the pressure fluctuation.

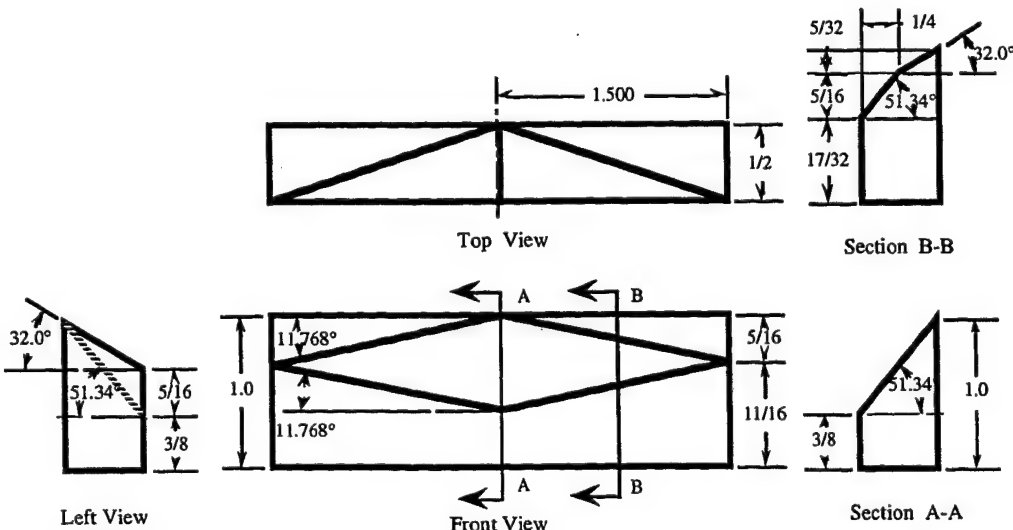


Figure 2.2(d) The Valley Wall

(5) Slanted Wall 1: Rockwell and Knisely (1979) conducted an experiment in a water channel in which they focused on flow impingement in a cavity with $L/H \approx 2$. From their flow visualization the shedding vortices may experience three possible types of impingement in the vicinity of the top edge of the RW: (a) complete clipping, (b) partial clipping, and (c) complete escape. In the supersonic flow case, visualization of the SL impingement by the infinite fringe interferogram technique (Zhang, 1987) shows that the high energy flow was partly clipped also. It was reasoned that if less high energy air flows into the cavity, the amplitudes of the pressure fluctuations should be smaller. The SW1, as shown in figure 2.2(e), was designed to change the angle of SL impingement to let the impingement flow move away easily and, hopefully, to reduce the fraction of the high-energy SL flowing into the cavity, *i.e.*, to weaken the pressure oscillation.

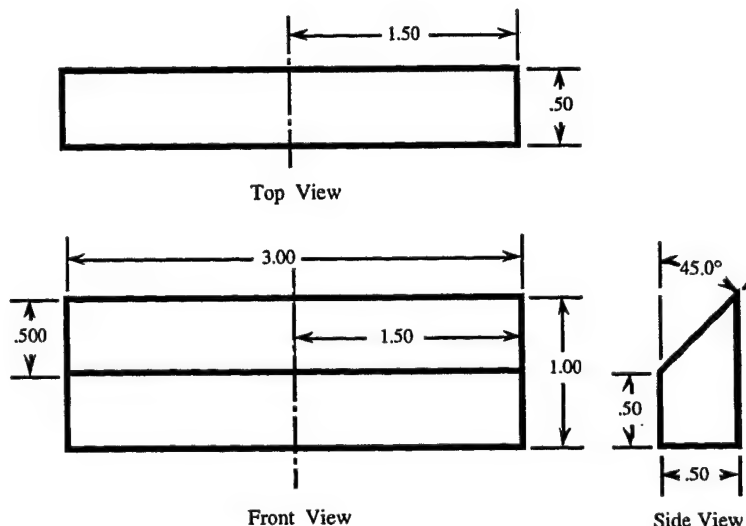


Figure 2.2(e) The Slanted Wall 1

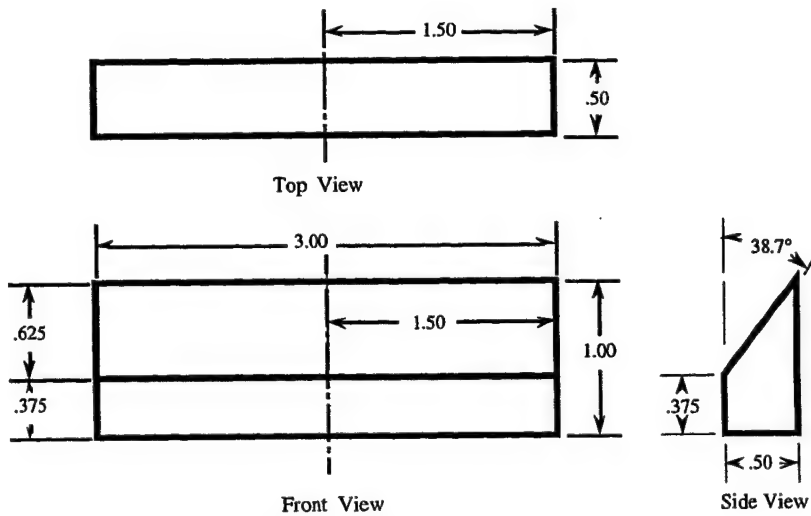


Figure 2.2(f) The Slanted Wall 2

Besides the slanted wall 1, two more slanted walls, namely 2 and 3, which have different slant angles were also tested. These three walls were designed to investigate how the RW angle attenuated the pressure fluctuations and if there was an optimum angle. The SW3 was cut deepest and had a 30.2^0 angle relative to the vertical direction. SW1 and 2 had angles of 45^0 and 38.7^0 respectively.

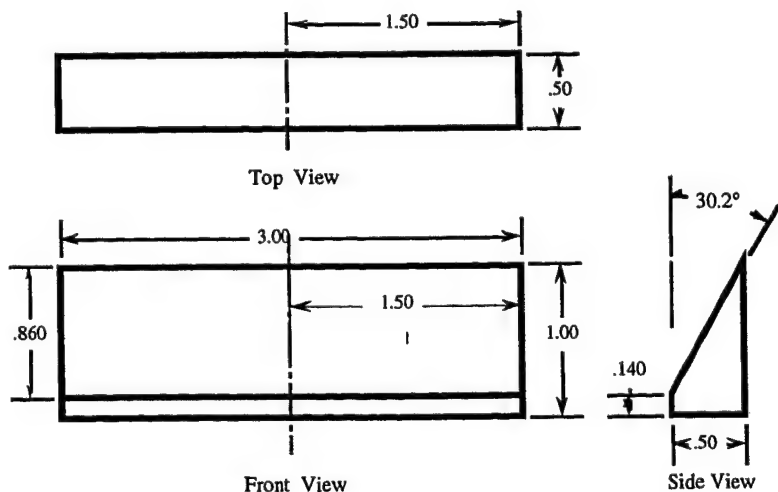


Figure 2.2(g) The Slanted Wall 3

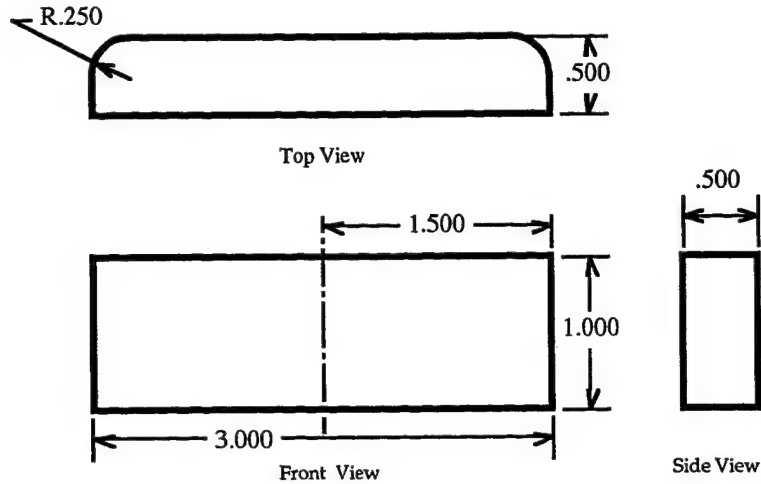


Figure 2.3 The Wall Base for Passive Control

It should be noted that for easy machining and installation several of these walls were designed to screw on to a wall base as shown in figure 2.3. Thus the entire assembly becomes the RW. This wall base was also used as an obstacle inside the cavity to investigate its effect on the cavity oscillation process.

2.2.3 Boundary Layer Spoilers:

Franke and Carr (1975), Clark *et al* (1980), Shaw *et al* (1988), Smith *et al* (1990), and Baysal *et al* (1994) put spoilers ahead of the cavity to alter the incoming BL properties and examine how the changes in the SL characteristics above the cavity affected the pressure fluctuations. Their spoilers included a saw-tooth fence, a small perforated fence, a wedge, and small vertical pins. Some of them were effective. The disturbed SL changed the pattern of the shedding vortices, reorganized its vorticity structure and, as desired, made a mismatch between its specific frequencies and the cavity acoustic frequencies.

In this study, two different BL spoilers were used. These were three Wheeler doublet type vortex generators (VG's) and a BL separator (*i.e.*, a wedge). The VG (0.2 inch x 1.2 inch x 1.75 inch), as shown in figure 2.4(a), was used to create counter-rotating vortices in the BL and further thicken the BL (Pearcey, 1961). On the other hand, the VG can also transfer high momentum flow from the free stream into the BL, thus increasing the turbulent fluctuations. Since the frequencies of the turbulent fluctuations shift to a higher band (Barter, 1995), the characteristics of the shedding vortices should also be modified. As the incoming BL is disturbed and energized, the SL after the separation point would be more energetic and the impingement point could move further downward on the RW.

The purpose of using a wedge is to separate the BL before the cavity. Only one wedge (0.4 inch x 0.2 inch x 5 inch), as shown in figure 2.4(b), was tested. The wedge was placed such that its trailing edge was 1 inch ahead of the leading edge of the cavity. The wedge angle is just high enough to separate the BL and induce an unsteady separation shock upstream of the wedge (Barter, 1995). The SL extends from the wedge trailing edge to a distance of 5 times of the height (0.2 inch) of the wedge before its reattachment near the leading edge of the cavity. It is expected that this turbulence-enhanced incoming BL should interfere with the generation of the shedding vortex and change the oscillation frequencies.

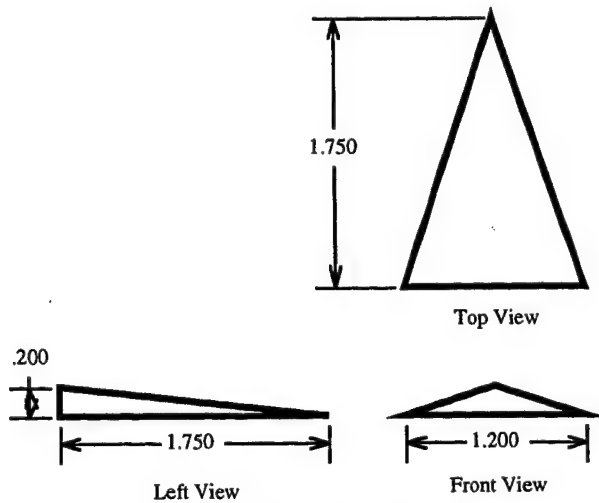


Figure 2.4(a) The Wheeler Doublet Type Vortex Generator

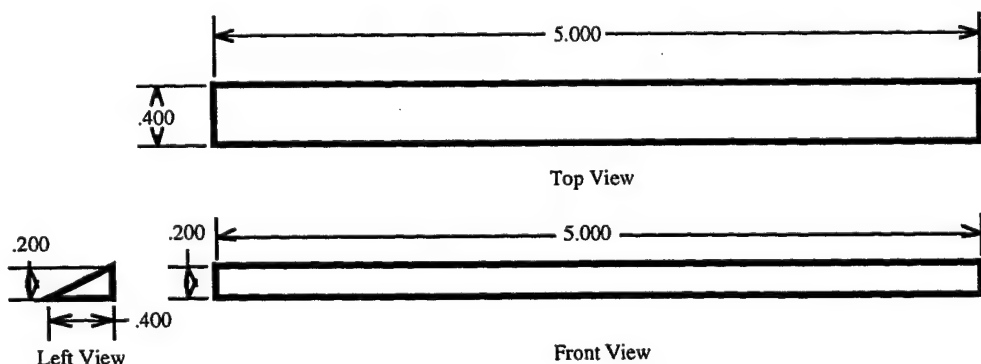


Figure 2.4(b) The Wedge

2.2.4 2-D Shock Generators

A) "Strong" Shock Generator

A thin flat plate with a hemi-cylindrical leading edge was used as the 2-D "strong" shock generator in the experiment. The plate is 6.8 inch long \times 4 inch wide \times 0.3 inch thick. It is wider than the cavity model to relieve edge effects on the cavity flow and is long enough to avoid the interference of the trailing-edge expansion wave with the cavity flow. The plate was attached to the tunnel ceiling as shown in Figure 2.3 by two stings with sharp leading and trailing edges. It could be adjusted streamwise to alter the impingement position of the shock wave on the shear layer. In this experiment, the impingement position of the shock wave is defined as the intersection of the shock wave and the upper surface of the shear layer assuming that the shear layer thickness is given by the undisturbed boundary layer thickness.

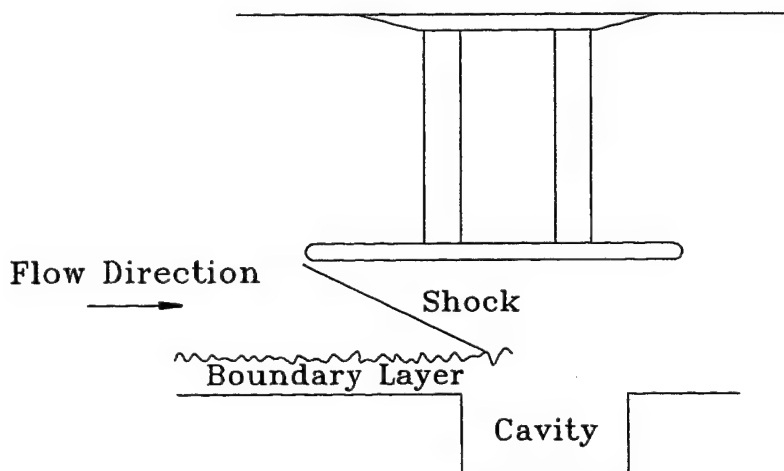


Figure 2.3 2-D "Strong" Shock Generator in the Tunnel

According to blast wave theory, the slope of the plate-generated shock wave is nearly constant beyond a distance approximately 1.8 inch away from the plate surface

which is about the distance between the lower surface of the shock generator and the upper surface of the shear layer. The theoretical shock angle and pressure ratio across the shock at this distance are 20.9° and 3.46 respectively. Because another shock wave with a smaller strength was also used in the experiment, the shock wave induced by this flat plate is referred to as the “strong” shock whereas the other case (described in the next paragraph) is referred to as the “weak” shock.

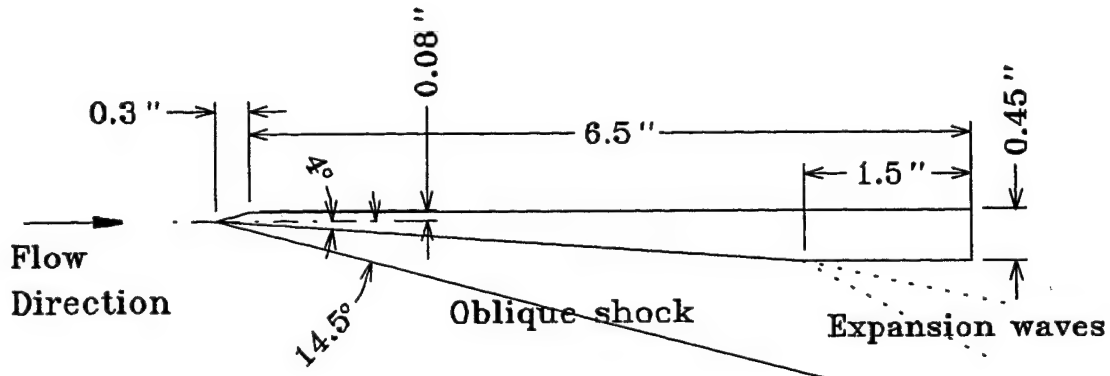


Figure 2.4 2-D “Weak” Shock Generator

B) “Weak” Shock Generator

A plate with a sharp leading edge whose lower surface forms a 4° wedge angle with the incoming freestream was used as the “weak” shock generator (Figure 2.4). Similar to the “strong” shock generator, the “weak” shock generator is wider than the cavity model to reduce the 3-D side effects and is long enough to avoid the interference of the expansion wave from the end of the wedge with the cavity flow. Also it was mounted above the cavity and could be adjusted streamwise in the same way as the “strong” shock generator. The theoretical shock angle and pressure ratio across the generated oblique shock are about 14.5° and 1.62 respectively. In order to compare the effects of different shock-induced pressure jumps on the cavity flow,

approximately the same pressure jump position at the bottom of the shear layer was used in both cases (to be discussed in a later section).

2.2.5 Store Models

The simplified baseline store model is a cylinder with a hemi-spherical nose. The store is 2.4 inch long and has a diameter of 0.5 inch. Thus the store-to-cavity length ratio, l/L , is $4/5$ and the store-diameter to cavity-depth ratio, d/H , is $1/2$. For the single store/cavity interaction experiment (one phase of the experiment), the store is mounted on the cavity centerline by two threaded rods projecting through two off-centerline holes on the cavity floor. The store axis is parallel to the undisturbed freestream and the position of the store could be adjusted vertically by the two threaded rods. The distance from the nose of the store to the front wall ($=0.3$ inch) is equal to that of the store base to the rear wall. The two threaded rods have a nominal diameter of 0.112 inch and their effects on the cavity flow are small compared to the store since their volume is relatively small. Surface flow visualization results, which will be discussed later, showed that the interference of the rods to be negligible.

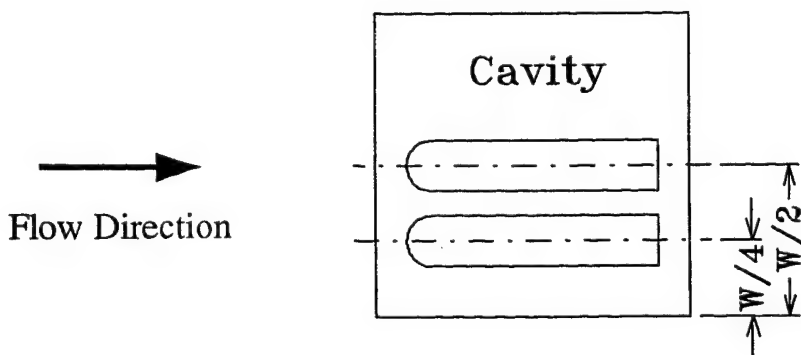


Figure 2.5 Top View of the Double Store/Cavity Interaction Configuration

For the double store/cavity interaction experiment (another phase of the experiment), two baseline stores were placed in the cavity, one on the centerline (as

described above) and the other on the left side of the cavity (looking upstream) with its axis parallel to the freestream and at $z=W/4$ (Figure 2.5). The off-centerline store was supported in the same way as the centerline store and the distance of the store nose to the front wall was the same as that of the centerline store.

To examine the effects of store dimensions on the cavity flow, two other store models were used. Compared to the baseline store, the first one had a different diameter (3/8 inch) but the same length (2.4 inches), i.e., $V/L=4/5$ and $d/H=3/8$, and the second one had a different length (1.8 inches) but the same diameter (0.5 inch), i.e., $V/L=3/5$ and $d/H=1/2$. They are shown in Figure 2.6.

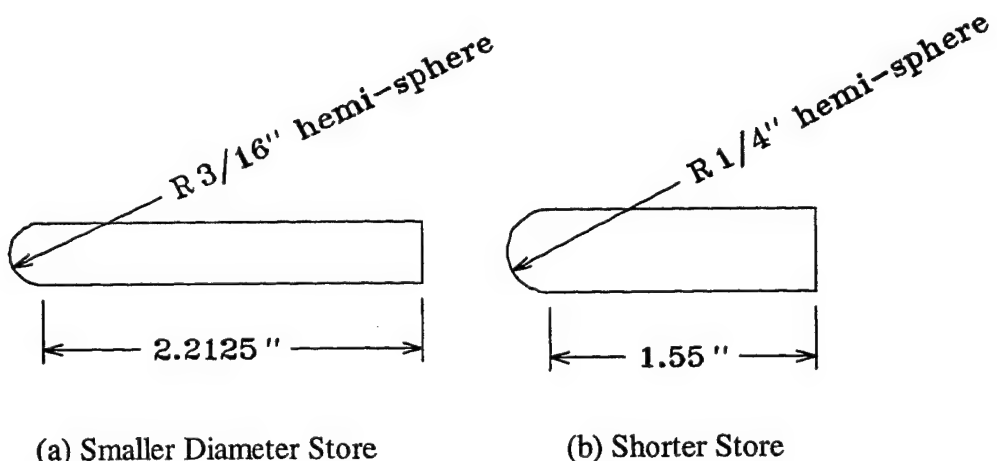


Figure 2.6 Other Store Models Used in the Experiment

2.2.6 Block Inserts

Two side blocks with dimensions of 3 inch \times 1 inch \times 1 inch as shown in Figure 2.7 could be inserted into both sides of the cavity model to reduce the width of the cavity to 1 inch. The effects of W/H and the store-to-cavity volume ratio on the cavity flow were examined by changing the width of the cavity.

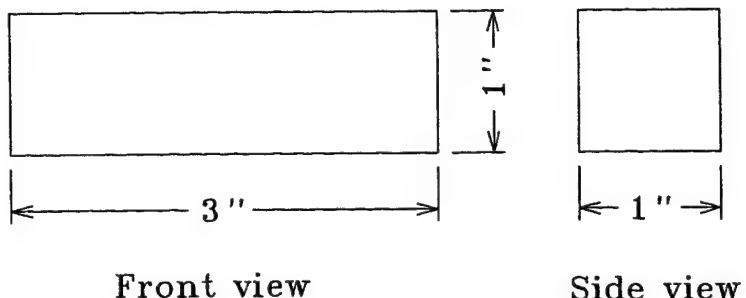
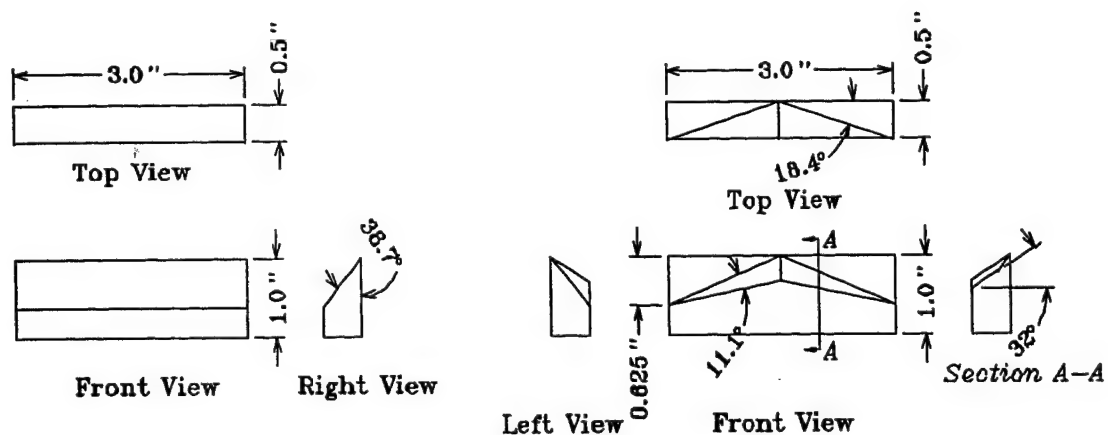


Figure 2.7 Block Inserts



(a) Slanted Rear Wall

(b) "Beak" Rear Wall

Figure 2.8 Passive Control Rear Walls (Perng and Dolling, 1996)

2.3 INSTRUMENTATION AND DATA ACQUISITION

Fluctuating surface pressure measurements on the cavity surface were made using Kulite Semiconductor Products, Inc., Model XCQ-062-15A and XCQ-062-50A transducers. The transducers have a nominal outer diameter of 0.0625 inch and a pressure-sensitive diaphragm of 0.028 inch in diameter. Perforated screens above the diaphragm protect the transducers from damage by dust particles but limit the frequency response of both models to about 50 kHz. The transducers were flush

mounted with the cavity surface and were calibrated using a Heise digital pressure gauge, Model 710A, which is accurate to 0.001 psia. Calibration was done by mounting a well-sealed calibration cap on the top of the cavity model. The calibration cap was connected to an air tank with valves permitting connection to a vacuum pump and/or the atmosphere. The calibration range varied for different ports and different cases depending on the anticipated pressure range at that port. The determination of the calibration ranges was a trial-and-error task.

Outputs from the transducers were amplified by Dynamics Model 7525, Measurements Group Model 2311 or PARC Model 113 amplifiers and then filtered by Ithaco Models 4113 or 4213 analog filters with the cut-off frequency set at 50 kHz or 25 kHz. Data acquisition was performed using two LeCroy analog-to-digital (A/D) converters (Model 6810 wave form recorders). The digitizers are 12 bit accurate and can sample up to eight channels simultaneously at 1 MHz. In this experiment, data were sampled at 1 MHz or 50 kHz depending on whether cross correlation or power spectra were required. That corresponds to a tunnel time of 0.524288 and 10.48576 seconds for 1 MHz and 50 kHz sampling rates respectively. A total of 512 records (524,288 data points) were obtained for each channel. Thus the bandwidth of the power spectral plots is around 49 Hz. Data from the A/D memory buffers were downloaded to an HP 9000 Model 380 workstation and stored on magnetic tapes for later analysis.

The experimental data were analyzed using a standard time-series analysis method which includes the calculation of mean, standard deviation, probability density function, cross correlation and power spectral density functions.

2.4 Flow Visualization:

Visualization of the surface flow pattern can be very helpful in exploring flowfield structure. The global overview offered by flow visualization can offer physical insight that cannot be obtained even from elaborate point measurements. In high speed flows, the kerosene-diesel-lampblack method is widely used. The amount of each component of the mixture depends on the tunnel conditions and the running time. If incorrect, the film can remain undried throughout a test and may become smeared when the tunnel is shut down. Generally, the volume ratio of diesel to kerosene is from about 2 to 4. In this method the mixture is painted on the model surfaces and the nearby tunnel floor. Then after shutting down the tunnel, the almost dried mixture is lifted off those surfaces on several sheets of transparent tapes. The full scale, undistorted, surface streaklines provide a record of the cavity flow characteristics, like surface flow directions, saddle (unstable) points, vortex foci, separation lines, and reattachment lines. Although this method is straightforward and useful, it must be remembered that the resulting pattern represents the direction of the mean surface shear stress and care is needed in interpreting the patterns in highly unsteady flows.

2.5 Test Program:

In the first phase, the baseline cavity ($L/H = 3, 4, \& 5$, $L = 3$ in) was tested to determine the cavity flow type (*i.e.*, open, transitional, or closed, Stallings and Wilcox, 1987) and the vortex structure. Flow visualization and instantaneous pressure measurements were performed to determine the number of vortices and to determine the oscillation frequencies of each mode. The experimentally obtained frequencies were compared with Rossiter's predictions.

In the second phase, the effect of cavity depth was examined. In Rossiter's formula, values of k_c and α depend on the motion of the shedding vortex. Therefore, changing the cavity depth from 1 in to 0.5 in, *i.e.*, $L/H = 3, 4, 5, \& 6$ ($L = 3$ in), should change the values of k_c and α such that the dominant oscillation frequencies shift. It was anticipated that this would indicate whether Rossiter's model, or Heller and Bliss's model (which does not include a shedding vortex) is more appropriate. In addition, a conditional sampling code and ensemble averaging technique were applied to detect SL impingement/shock event on the RW and to find the evidence of the traveling acoustic wave in the cavity.

In the third phase, the various walls described in section 2.2.2 were tested. Two were placed in the front of the cavity in an attempt to interfere with the generation of shedding vortices. All walls were then placed at the rear edge. Since the depths of those walls are 1 in, the ratio of L/H could only be fixed at 3 or 4 by changing the cavity length.

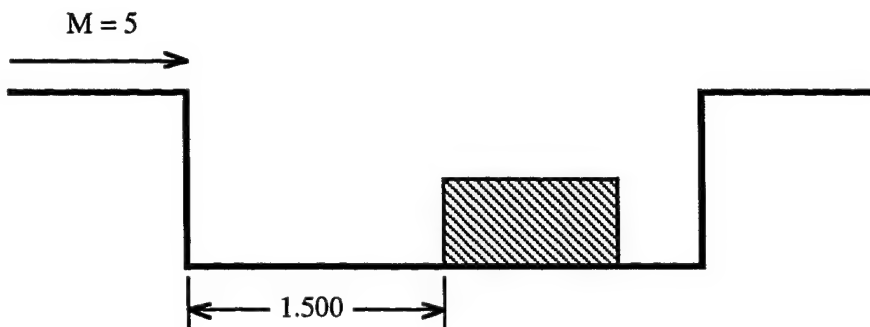


Figure 2.5(a) The Wall Base as an Obstacle inside the Cavity

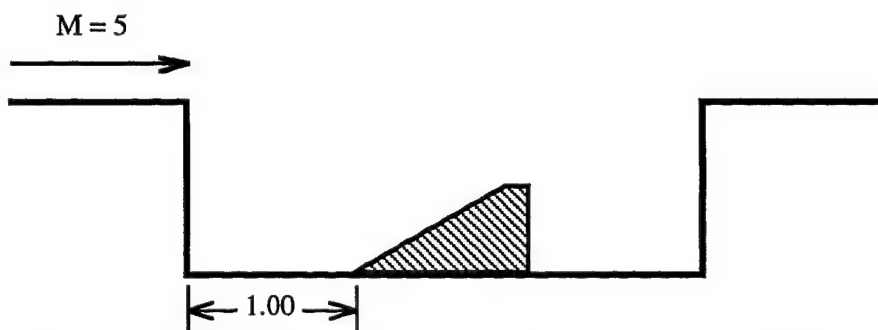


Figure 2.5(b) The Slanted RW3 as an Obstacle inside the Cavity

In the fourth phase, two BL spoilers (the wedge and 3 VG's) and two internal obstacles (the SW3 and the wall base) were used to explore their effect on the pressure oscillation amplitudes and frequencies. These spoilers were attached on the tunnel floor such that their trailing-edges were 1 in ahead of the cavity leading edge. The wall base used as one of the internal obstacles was placed in the middle of the cavity or 1.5 inch behind the cavity leading edge, as shown in figure 2.5(a), on the cavity floor with its front face downward. In addition, the SW3 with its slanted face upward and upstream (like a wedge shape obstacle) was mounted in the middle of the cavity, as shown in figure 2.5(b). A combination of the VG's spoiler and the wall base obstacle was tested simultaneously.

The experiments involving perturbed flow were conducted in five phases: shock/cavity interaction, single store/cavity interaction, effects of store dimensions and critical volume ratio, double store/cavity interaction and passive control techniques. Surface flow visualization was performed to help explore the corresponding flow structure. Of all these phases, only the double store/cavity interaction experiment involves an asymmetric cavity flowfield. Thus, in this phase pressure measurements were made not only on the longitudinal centerline of the cavity but also at some off-centerline ports. For the other phases, the flowfields are symmetric about the cavity centerline and for simplicity pressure measurements were made along the centerline only.

2.6 Uncertainty:

Experimental uncertainty has been examined largely through repeatability of the pressure measurements. In the pressure transducer calibration process, the deviation of curve fit from the data points is within 1%. The unavoidable drift problem associated with the amplifiers can affect the measured pressure signals primarily through shifts in the transducer zero rather than the sensitivity. Thus the primary effect of drift is on the mean values not the rms values. The gain of the amplifiers was typically set around 500 such that electronic noise was not more than ± 20 mv which was about 0.5% of the transducer's full-scale output. Unfortunately, about three of the amplifiers generated additional electronic noise such that there was increased energy in the low frequency range (about ≤ 0.5 kHz). In the worst case, the noise signal was sinusoidal with relatively very high amplitude. Accordingly, the peaks in the spectrum in this low frequency range were not considered as the natural oscillations of cavity flow. The room temperature of the laboratory was kept at about 75 $^{\circ}$ F but the temperature was not uniform due to the cold-air outlets of the air conditioning system. The temperature increase in the afternoon resulted in the output of amplifiers drifting. Therefore, every two tests, the transducers were recalibrated. In addition some measurements were repeated with different transducers on a different day. By checking the data at points FW1, F10, and R7 for cases of baseline ($L/H = 3$ & 4) and plate-separator cavities, the maximum differences in \bar{P}/P_{∞} and σ_p/P_{∞} from their individual averages are less than 8.9% and 3.4% respectively.

Chapter 3: Baseline Cavity Oscillation Investigation

In this chapter, mean and instantaneous properties of the baseline cavity flow will be discussed. In the baseline investigation, cases with $L/H = 3, 4$, and 5 (all open type cavity flows) have been explored. The vortex structure in the hypersonic cavity flow was determined from flow visualization and basic statistical analysis of the measured pressure signals. Pressure power spectra were calculated and the basic modes of oscillation determined and compared with Rossiter's (1964) and Heller and Bliss's (1975) models. The effects of the cavity length and depth were also investigated. In very high speed flow, the compressibility effect on the SL is important and was examined by detecting the flow impingement on the RW. Finally, the acoustic wave in the cavity which is linked to the flow impingement is shown to be a key factor causing pressure oscillations.

3.1 MEAN PRESSURE AND STANDARD DEVIATION DISTRIBUTIONS

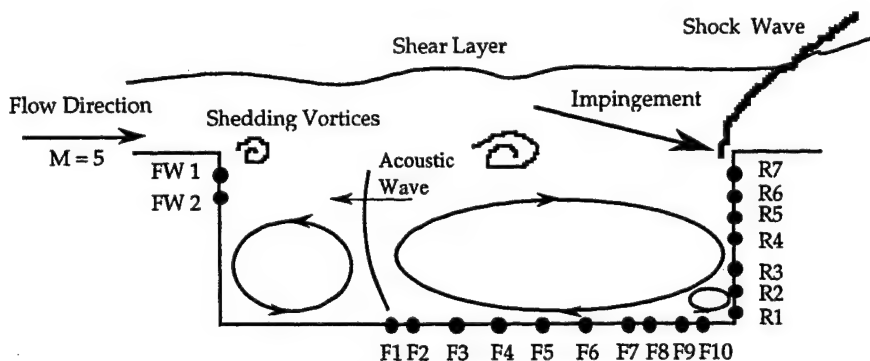


Figure 3.1 Distribution of Transducers and Vortices ($L/H=3$)

The transducer locations on the center line of the cavity for the case $L/H = 3$ ($L = 3$ inches) are shown in figure 3.1. The vortex structure is also shown and will be discussed later and in section 3.2. The distributions of normalized mean pressure and its standard deviation along the center line of the cavity are shown in figures 3.2(a) and 3.2(b), respectively for this case. The standard deviation is

calculated for the bandwidth 0.34 kHz to 25 kHz to eliminate electronic noise for reasons which will be explained later when the spectra are discussed in section 3.3. The upper edges of the FW and the RW are at -1 and +4 respectively on the abscissa; the front and rear of the cavity floor are at 0 and +3 respectively.

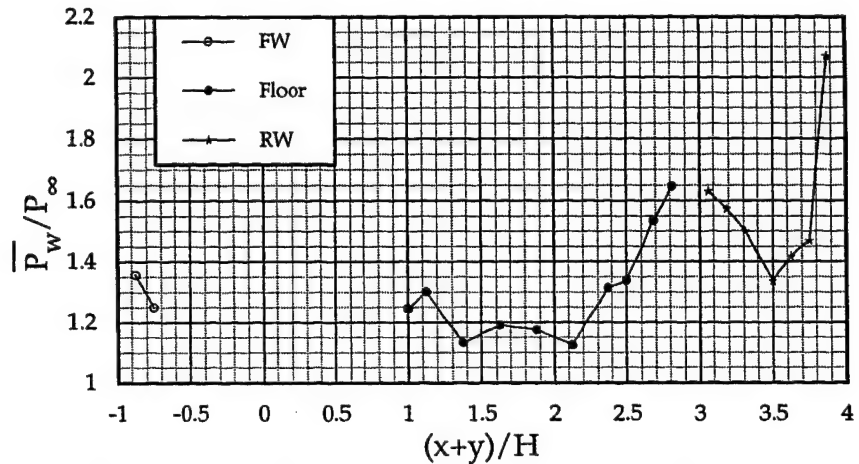


Figure 3.2(a) Mean Pressure Distribution (L/H=3)

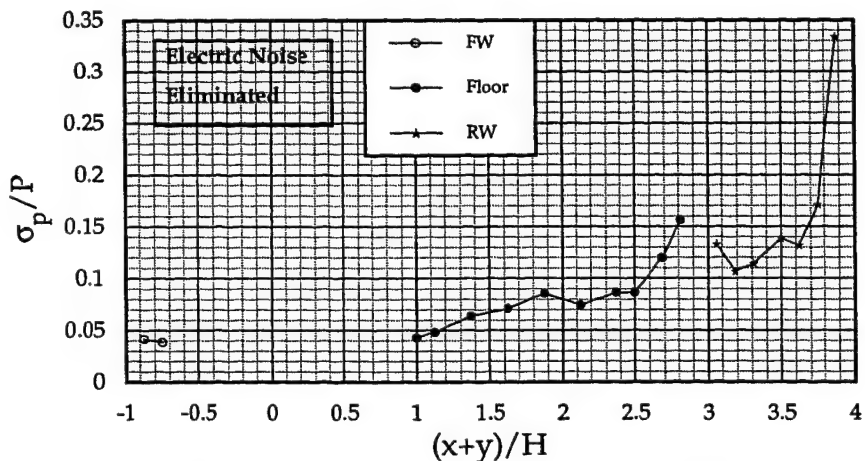


Figure 3.2(b) Normalized Standard Deviation (L/H=3)

As noted earlier, three major mechanisms dominate the mean pressure distribution inside the cavity, namely trailing-edge vortices, the flow recompression, and the SL impingement near the trailing edge (Zhang and

Edwards, 1990). The impingement occurs close to the top of the RW (*i.e.*, around point R7) and forces high-energy flow into the cavity. Then, a recompression process causes the pressure rise along the RW and the rearward portion of the cavity floor. Since the high energy inflow goes down the RW towards the trailing edge of the floor, the standard deviation values at points F8(2.5), F9(2.6875), and F10(2.8125) are higher as shown in figure 3.2(b). Note values in parentheses are values of $(x+y)/H$. However, the large trailing-edge vortex is very strong and results in a relatively low pressure area around the middle point (*i.e.*, point R4(3.5) on the RW). The small rear corner vortex is not evident in the mean pressure distribution but this is not surprising for it is very weak. It is evident in the visualization in section 3.2. However its influence is clear in the standard deviation distribution on the RW.

The standard deviation decreases from the middle point (R4) to the second point R2(3.1875), then increases from its lowest value at R2 to a larger value at the lowest point R1(3.0625). Since vortex motion causes larger variations in the pressure signal, an increased standard deviation here is indicative of a small vortex in the rear corner also. The region of influence of the large trailing-edge vortex is bracketed approximately between points F3 and F8 (*i.e.*, $1.375 < (x+y)/H < 2.5$) on the cavity floor and between points R3 and R5 (*i.e.*, $3.3125 < (x+y)/H < 3.625$) on the RW.

For the baseline case $L/H = 4$ ($L = 4$ inches), the distributions of normalized mean pressure and its standard deviation along the center line of the cavity floor and RW are shown in figures 3.3(a) and 3.3(b), respectively. The upper edges of the FW and the RW are at -1 and +5 respectively on the abscissa; the front and the rear of the floor are at 0 and +4 respectively. Since the $L = 4$ inches case is obtained by removing either the FW or the RW, the number of measuring points is increased to 17, rather than 10 on the cavity floor. In figure 3.3(a), there are some fairly large pressure variations around the 9th to 11th points (*i.e.*, $2.5 < (x+y)/H < 2.8125$). Although this phenomenon cannot presently be explained, it is repeatable, as shown by a subsequent test.

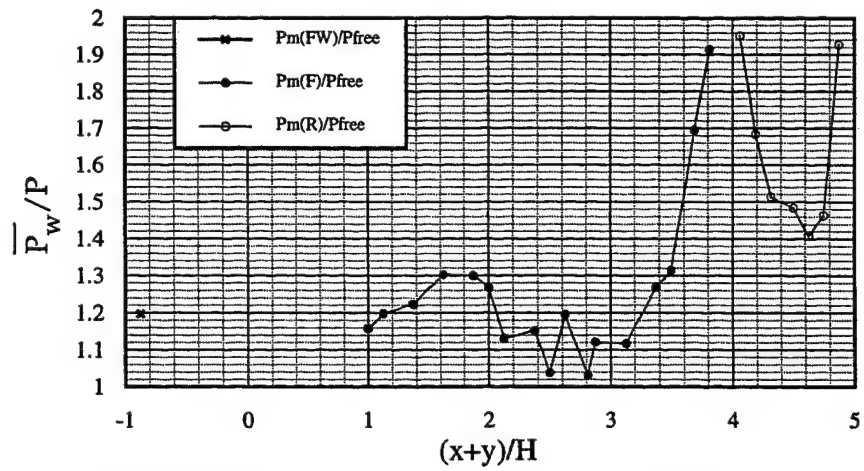


Figure 3.3(a) Mean Pressure Distribution (L/H=4)

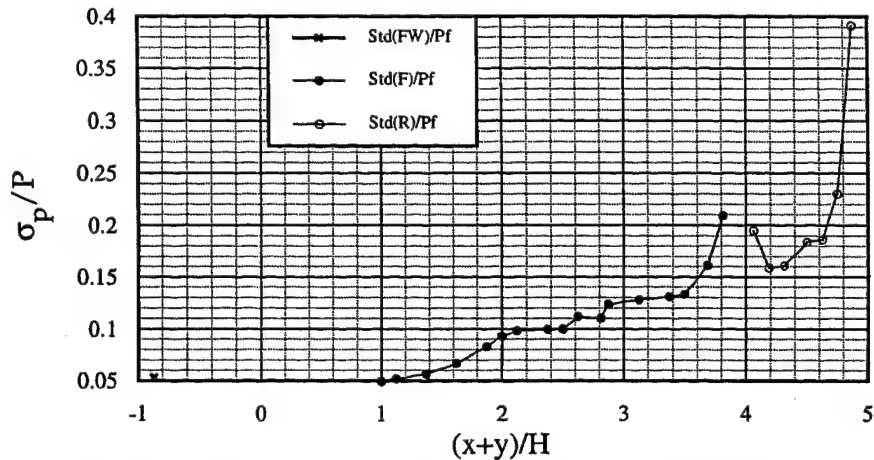


Figure 3.3(b) Normalized Standard Deviation (L/H=4)

Generally, the mean pressure distribution is similar to the case L/H = 3. Accordingly, a larger trailing-edge vortex is recognized and its influence is bracketed approximately between the 5th point and 15th point (*i.e.*, $1.875 < (x+y)/H < 3.5$) on the cavity floor and between points R3 and R5 (*i.e.*, $4.3125 < (x+y)/H < 4.625$) on the RW. A small corner vortex caused a high value of the standard deviation around the 17th point (3.8125) on the floor and point R1(4.0625) on the RW. It is interesting that the mean pressures at the 17th point on the floor and point R1 on the RW are large even compared to the point

R7(4.875) on the RW. This means that the recompression effect is strong and the impingement point is near the rear corner of the cavity. Similar distributions were obtained from Zhang and Edwards (1990) as shown in figure 2.3. As L increased, a thick SL approached the RW with less momentum which decreased the pressure level on the top of the RW. In addition, the normalized standard deviations at these two points are large too and are about 50% above values seen for $L/H = 3$. In this case the vortex structure from flow visualization result is similar to that of the case $L/H = 3$.

Stallings and Wilcox (1987) and Zhang and Edwards (1990) measured the mean pressures on the FW, the floor, the RW of the case $L/H = 3$ at lower Mach numbers. In Stallings and Wilcox's investigation, the mean pressure remained almost unchanged until a spike near the rear end of the cavity floor. Their pressure distributions on the cavity floor for several Mach numbers and several cavity depths (δ fixed at 0.2 in) showed no evidence of a vortex structure. Compared with their result, figure 3.2(a) has a clearly concave curvature from points F2 to F10 (*i.e.*, $1.125 < (x+y)/H < 2.8125$) driven by the large trailing-edge vortex. Such concave curvature is typical for an *open* type cavity flow (Charwat *et al.*, 1961). Similar concave curvature was obtained by Zhang and Edwards. In their test, δ/H was about 0.4 which is close to the 0.67 in this study. The δ/H in Stallings and Wilcox's test was less than 0.1 which is much smaller than 0.67. Thus a possible reason for the difference between the mean pressure distributions on the cavity floor is the ratio of δ/H .

3.2 SURFACE FLOW PATTERNS AND CAVITY FLOW STRUCTURE

The kerosene-diesel-lampblack method was used to visualize the time-average surface streaklines. For the $L/H = 3$ ($L = 3$ inches) case, the photo shown in figure 3.4(a) of the surface patterns on the cavity wall and floor was taken as an angle. Figure 3.4(b) is an exploded view manually traced from figure 3.4(a). The results show the mean cavity flow is 3-D and symmetric about the longitudinal center line. The flow structure over the central region deduced from figure 3.4 is shown in figure 3.1. From figure 3.4(b), the traced streaklines reveal the possible existence of a large clockwise-rotating trailing-edge vortex and a small

counterclockwise-rotating rear corner vortex. This small rear corner vortex has not been noted by many experimental supersonic cavity-flow researchers. However, it is very possible that this small corner vortex is not as important as the large vortex since it is only affiliated with the large one. In the forward part of the cavity, a counterclockwise vortex exists along the center portion. A straight separation line and a saddle point are located about 0.9 inch downstream of the FW as shown in figure 3.4(b), and separate the large trailing-edge vortex from the front vortex. Two stable foci are located near the FW but not on the center line of the cavity. Such a flow structure suggests there would be a finite yawing moment on a weapon during the release process if the weapon was not on the longitudinal center line. Since the streak lines reveal a 3-D flowfield symmetric about the center line, this gives some indication that a symmetric 3-D RW would be effective for passive control.

From the flow visualization of the case $L/H = 3$ ($L = 3$ inches), the 3-D cavity flow is symmetric in the mean and there should have pressure variations laterally (*i.e.*, $\pm z$ direction). Pressure signals on the two off center-line points shows that the mean pressure distribution is symmetric as is the standard deviation distribution. The mean pressures (normalized by the pressure at R7 on the center line) are 1.04 and 1.03 at $z/W = 0.25$ and -0.25 respectively. Similarly, the dimensionless ratios of the standard deviation are 1.66 and 1.60 (*i.e.*, $\sigma_p/(\sigma_p)_{center}$) respectively. This lateral variation of the pressure signals was also shown by Stallings & Wilcox (1987), Suhs (1987), and Rizzetta (1988).

For the longer cavity, $L/H = 4$ ($H = 1$ inch), other than there being a remarkable effect associated with the flow impingement on the top of the RW, as shown in figure 3.5, the 3-D symmetric flow structure is similar to that of the case $L/H = 3$. A large clockwise-rotating trailing-edge vortex and a small counterclockwise-rotating rear corner vortex are recognized too. On the centerline, about 1.3 inches downstream of the FW, a curved separation line and a saddle point are recognized. This limited trailing-edge vortex size correlates with the mean pressure distribution and the standard deviation distribution as shown in figures 3.3(a) and (b).

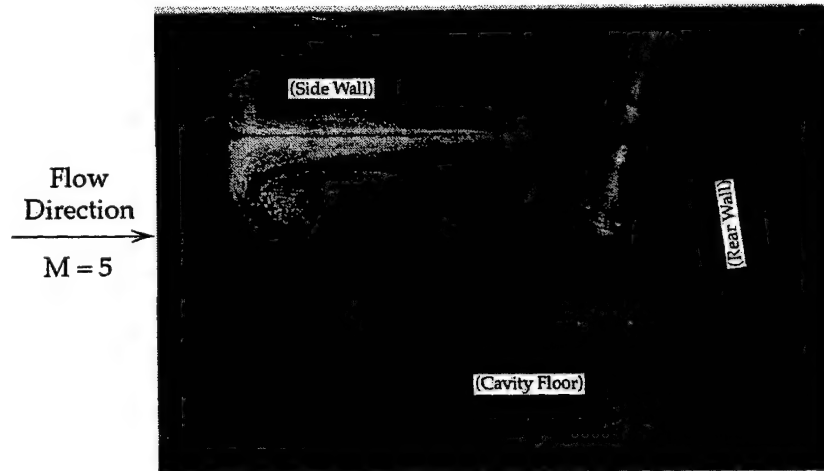


Figure 3.4(a) Flow Visualization

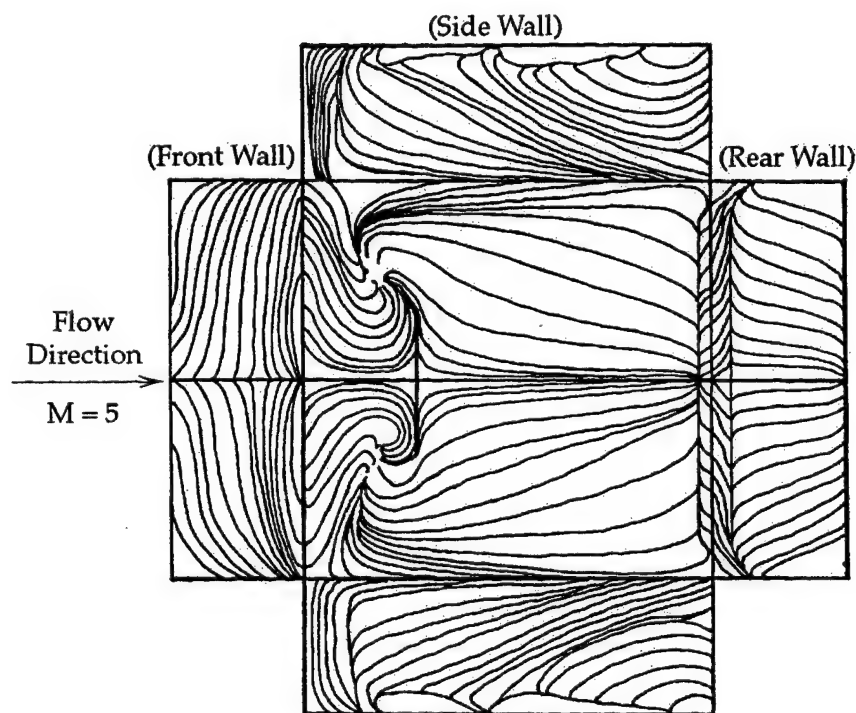


Figure 3.4(b) Exploded View Based on Measured Surface Flow Patterns ($L/H=3$)

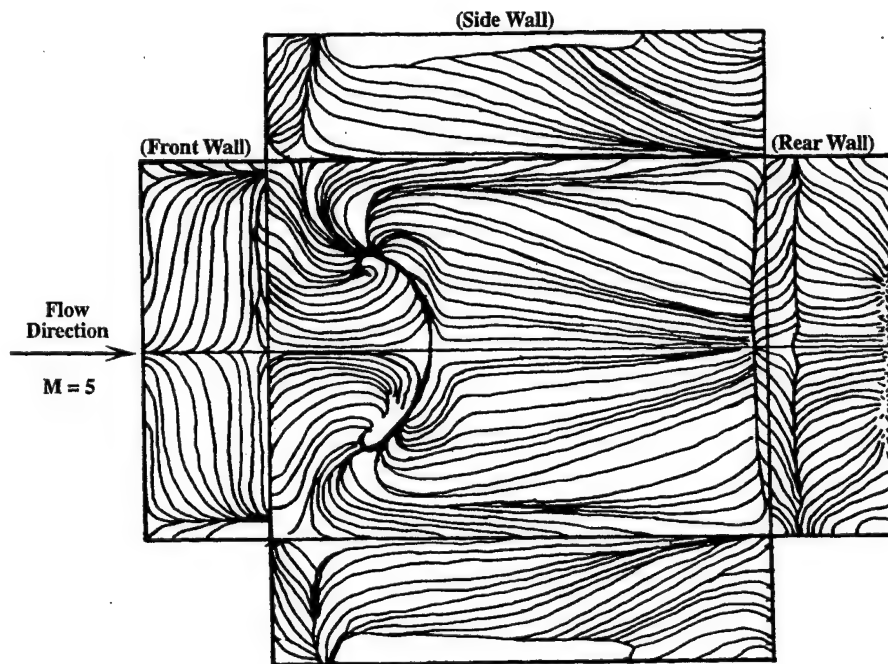


Figure 3.5 Exploded View Based on Measured Surface Flow Patterns ($L/H=4$)

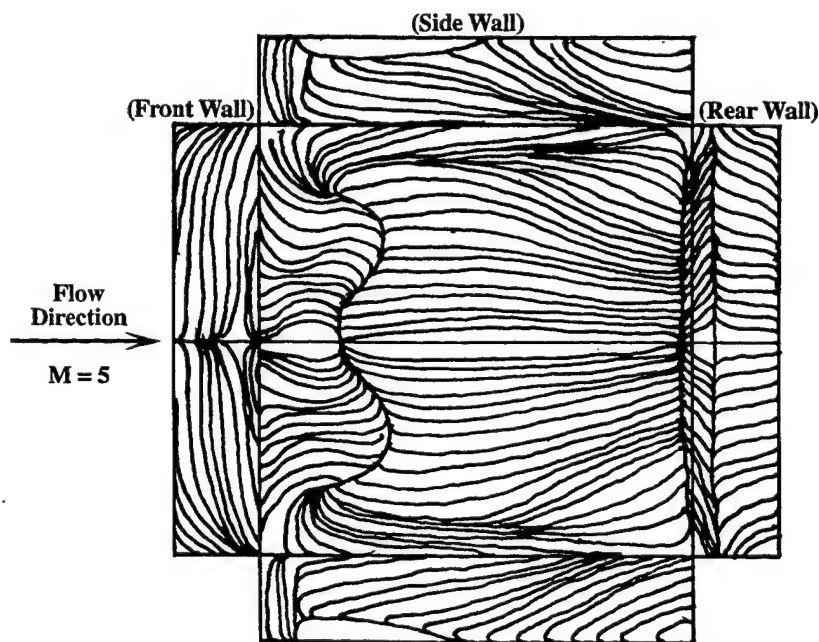


Figure 3.6 Exploded View Based on Measured Surface Flow Patterns ($L/H=5$)

By decreasing the depth of a cavity ($H = 0.6$ inches) the non-dimensional length can be increased to $L/H = 5$. The surface flow pattern is shown in figure 3.6. Its 3-D symmetric flow structure is similar to those for $L/H = 3$ & 4 ($H = 1$ inch). On the centerline, about 0.6 inches downstream of the FW, a curved separation line and a saddle point are recognized. From the flow visualizations of the three cavities ($L/H = 3, 4$, and 5) the relative size of the leading-edge vortex did not increase as the ratio of L/H increased. This result is different from Zhang and Edwards's (1992) result in which the relative size of the front vortex gets bigger as the ratio of L/H increases (described in section 2.2.2). Overall, with the visualization assistance, over the ranges $3 < L/H < 5$, $3 < W/H < 5$, and $0.76 < \delta/H < 1.27$ all these three cavities are identified as *open* cavity type again and have a weaker front vortex, a stronger trailing-edge vortex, and a small rear corner vortex.

3.3 GENERAL POWER SPECTRA CHARACTERISTICS

The power spectra of the pressure signals measured at several points on the cavity floor and the RW are shown in figure 3.7 for $L/H = 3$. $G(f)$ has units of $(\text{psi})^2/\text{Hz}$. Comparisons with spectra from the undisturbed incoming boundary layer show that the high energy fluctuations at frequencies less than 1 kHz are due to the incoming turbulent BL ($\delta/H \approx 0.76$). In addition there is some electronic noise (around 180 Hz) from the signal amplifiers. To examine the influence of the noise, the signal standard deviations were recalculated in selected frequency bands (from 0.34 kHz to 25 kHz and from 0.78 kHz to 25 kHz). The results show that the larger fraction of the "noise" was below 0.34 kHz and that elimination of this noise reduces the rms of the overall signal by about 10%. Four different oscillatory modes are seen at $n = 1, 2, 3$, and 4 for all cases, but the 4th mode is much stronger for $L/H = 4$ & 5 (not shown). The frequencies of the first three modes for $L/H = 3$ are approximately 2.15, 4.44, and 6.64 kHz respectively. The mode frequencies are strongly dependent on the acoustic wave which is a forward-going compression wave induced by the flow impingement on the RW. The acoustic wave speed based on the adiabatic temperature (320K) in the cavity

is 358.6 m/s and the time for it to travel from the RW to the FW is 212.5 μ sec. Thus one forward or backward acoustic wave induces a periodic oscillation whose frequency is about 4.706 kHz which is close to the second mode frequency.

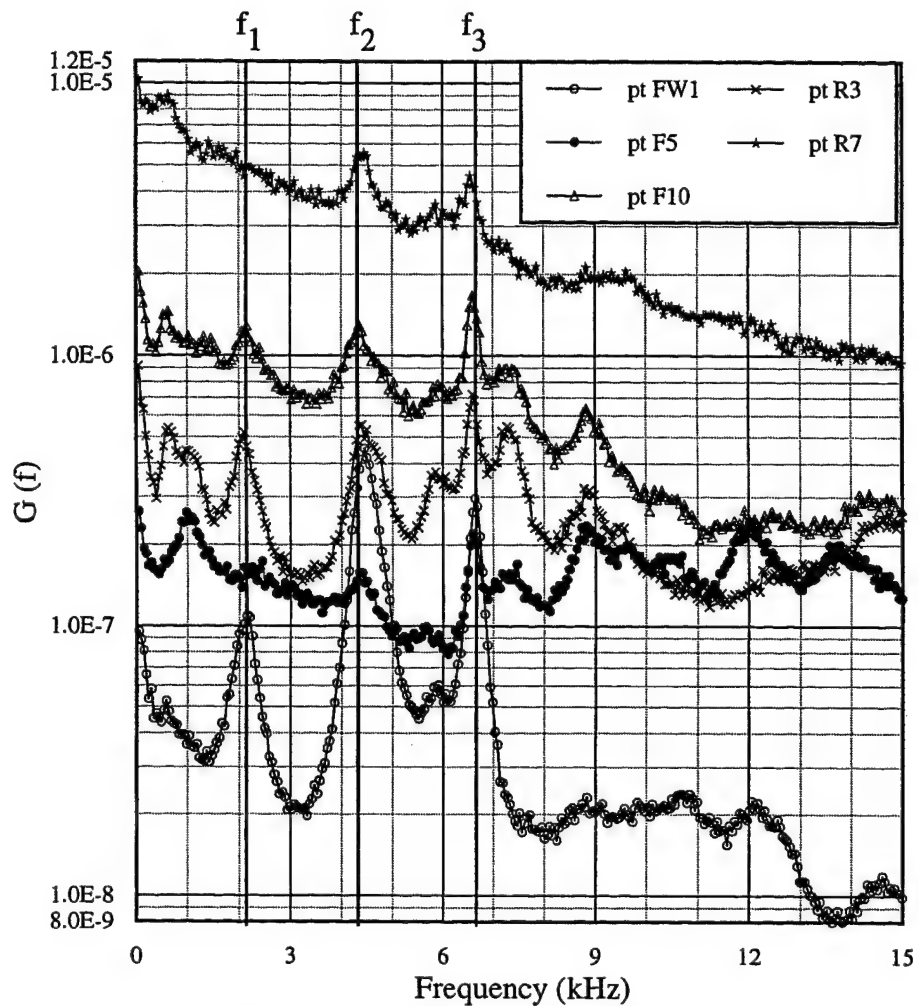


Figure 3.7 Power Spectra of the Baseline Cavity (L/H=3)

Two comparisons between the experimental and the calculated mode frequencies (by the modified Rossiter's formula) using two different sets of k_c and α are given in Table 3.1. It should be noted that the mode frequencies vary a little from station to station and the frequency values in the text and Table 3.1 are

values at points $(x+y)/H = 2.8125$ (F10), 3.8125 (17th point), and 2.875 (F5) for $L/H = 3, 4$, and 5 respectively. The reason for choosing point $(x+y)/H = 2.875$ as the station for $L/H = 5$ is that the first mode peak is not obvious at points further downstream. The first comparison is based on $k_c = 0.65$ and $\alpha = 0.3$ (the approximate averaged value of k_c and α from Rossiter (1964), Maciulaitis (1980), and Zhang and Edwards(1990)). The second comparison is made based on the explanation of Heller and Bliss (1975) for the cavity self-sustaining oscillation, namely that the reflected acoustic wave from the FW instead of the shedding vortex is the main cause of the impingement event on the RW. In this case, the value of k_c is the ratio of “the adiabatic temperature sound speed in the cavity” to “the free stream speed (U)”, *i.e.*,
$$\left(\frac{M}{\sqrt{1 + 0.5\beta(\gamma - 1)M^2}} \right)^{-1}$$
 which is 0.4682 ,

and the value of α is essentially zero. In the comparisons in Table 3.1, the discrepancy (last two columns) is defined as
$$\left(\frac{f_{\text{calculated}}}{f_{\text{experimental}}} - 1 \right) \times 100\%$$
.

From Table 3.1, the experimental second and third mode frequencies are about two and three times the first mode frequency, f_1 , respectively. Similar ratios were obtained by Morgenstern and Chokani (1994) in their numerical investigation of hypersonic cavity flowfields ($M = 6.3$). In the current study, the calculations based on $\alpha = 0$ (*i.e.*, $k_c = 0.4682$) agree better with the experimental values particularly for the first mode, with a maximum discrepancy of about 11%. The discrepancy based on $k_c = 0.65$ and $\alpha = 0.3$ is greater, up to about 27% for the first mode. The large discrepancy between the experiment and calculation for modified Rossiter prediction may be attributed to choosing inappropriate values of k_c and α . Exact values of k_c and α are difficult to determine since they vary with the various test conditions and ratio of L/H . Thus, from such comparisons alone it is difficult to say with certainty which model is correct. To explore the explanation of cavity self-sustaining oscillation given by Heller and Bliss (1975), the pressure signals on the FW and RW have been examined to determine if the forward acoustic waves generated by the SL impingement on the RW can be

detected. A conditional sampling program used to examine this coupling relation will be discussed in section 3.6.

<i>L/H</i>	<i>Frequency Modes (H=1")</i>	<i>Experimental Values (kHz)</i>	<i>Calculated Values (kHz)</i> ($k_c=0.65$) ($\alpha=0.3$)	<i>Calculated Values (kHz)</i> ($k_c=0.4682$) ($\alpha=0$)	<i>Discrepancy %</i> ($k_c=0.65$) ($\alpha=0.3$)	<i>Discrepancy %</i> ($k_c=0.4682$) ($\alpha=0$)
3	f_1	2.15	1.645	2.350	-23.42	9.40
3	f_2	4.35	3.996	4.701	-8.14	8.07
3	f_3	6.59	6.346	7.051	-3.70	7.00
3	f_4	8.84	8.696	9.402	-1.63	6.36
4	f_1	1.66	1.234	1.763	-25.66	6.20
4	f_2	3.17	2.997	3.526	-5.58	11.09
4	f_3	5.32	4.759	5.288	-10.58	-0.64
4	f_4	7.13	6.522	7.051	-8.51	-1.09
5	f_1	1.37	0.987	1.410	-27.80	3.15
5	f_2	2.54	2.397	2.820	-5.59	11.07
5	f_3	4.54	3.808	4.231	-16.12	-6.81
5	f_4	6.30	5.218	5.641	-17.17	-10.46

Table 3.1 Experimental and calculated mode frequencies for $k_c=0.65$ & 0.4682 with $H=1"$

3.4 EFFECT OF THE CAVITY LENGTH/DEPTH

L and *H* are two of the factors influencing cavity flow. Changing their values not only changes ratios of *L/H* and *W/H*, but also changes values of parameters of α and k_c in Rossiter's formula. In sections 3.1 and 3.2, mean pressure distributions and surface flow patterns demonstrated that the assumption of the *open* type cavity flow in the hypersonic speed was appropriate. In section 3.3, with *H* = 1 inch, *L* was varied from 3 to 5 inches and two models to predict oscillation frequencies were discussed. In order to explore the effect of *H* on oscillation frequencies further, four values of *H* were tested. They were 1, 0.75, 0.6, and 0.5 inches such that *L/H* = 3, 4, 5, and 6 (*L* = 1 inch). Rossiter's and Heller and Bliss's models were applied to calculate mode oscillation frequencies and discrepancies of these two models at point FW1 are shown in Table 3.2.

<i>L/H</i>	<i>Frequency Modes (L=3")</i>	<i>Experimental Values (kHz)</i>	<i>Calculated Values (kHz) (k_c=0.65) (α=0.3)</i>	<i>Calculated Values (kHz) (k_c=0.4682) (α=0)</i>	<i>Discrepancy % (k_c=0.65) (α=0.3)</i>	<i>Discrepancy % (k_c=0.4682) (α=0)</i>
3	<i>f</i> ₁	2.15	1.645	2.350	-23.49	9.30
3	<i>f</i> ₂	4.44	3.996	4.701	-9.95	5.88
3	<i>f</i> ₃	6.64	6.346	7.051	-4.40	6.19
3	<i>f</i> ₄	8.84	8.696	9.402	-1.61	6.36
4	<i>f</i> ₁	2.10	1.645	2.350	-21.67	11.90
4	<i>f</i> ₂	4.35	3.996	4.701	-8.09	8.07
4	<i>f</i> ₃	6.89	6.346	7.051	-7.87	2.34
4	<i>f</i> ₄	8.89	8.696	9.402	-2.16	5.76
5	<i>f</i> ₁	2.00	1.645	2.350	-17.75	17.5
5	<i>f</i> ₂	4.25	3.996	4.701	-5.93	10.61
5	<i>f</i> ₃	7.32	6.346	7.051	-13.28	-3.67
5	<i>f</i> ₄	9.33	8.696	9.402	-6.77	0.77
6	<i>f</i> ₁	2.00	1.645	2.350	-17.75	17.5
6	<i>f</i> ₂	4.15	3.996	4.701	-3.66	13.27
6	<i>f</i> ₃	7.42	6.346	7.051	-14.45	-4.97
6	<i>f</i> ₄	9.77	8.696	9.402	-10.97	-3.77

Table 3.2 Experimental and calculated mode frequencies for $k_c=0.65$ and 0.4682 with $L=3"$

Generally, mode frequencies calculated using both approaches are close to the experimental results except for the first mode. Since the value of α is 0.3, the calculated first mode frequency from the Rossiter's formula is always significantly less than the experimental value. Accordingly, the other three consecutive mode frequencies were underpredicted by the Rossiter's formula. The k_c effect is not as evident as the α . For Heller and Bliss's model, the calculated values were usually larger than experimental results. Since the actual temperature inside the cavity was not measured, it was estimated by assuming the adiabatic wall condition even though the flow inside the cavity was not uniform and not motionless. Therefore, the actual cavity air temperature could be less

than the adiabatic wall temperature such that the oscillation frequencies were overpredicted. However the prediction from the Heller and Bliss's model is a little better than that from the Rossiter's formula by comparing the maximum discrepancies, *i.e.*, 17.5% vs 23.5% and overall calculations of both models.

In sections 3.3 and 3.4, of all variations of L, H, and L/H, L is clearly the most important factor controlling oscillation frequencies. In Heller and Bliss's model, the acoustic wave travels between the FW and the RW. The value of L determines the travel time of the acoustic wave and, then, the oscillation frequencies are determined. In order to quantify the changes of the mode frequencies for different H values, the case L/H = 3 (L = 3 inches) was chosen as the standard cavity. Three other cases of L/H = 4, 5, and 6 (L = 3 inches) were compared with the standard. Those comparisons are organized in Table 3.3. In this table the difference is defined as $\left(\frac{f}{f_{L/H=3}} - 1 \right) \times 100\%$.

It can be seen that even as the ratio of L/H increased by 100%, the maximum difference in frequency of any of the modes was about 11% and the minimum was less than 1%. Generally the first and the second mode frequencies are almost unchanged. The effect of H and the ratio of L/H are not significant on the oscillation frequencies. Since for a shallower cavity the trailing-edge vortex is "squeezed", it might be expected that the vortex breathing motion and recompression process could change as the ratio of L/H is doubled. In turn the value of α would change substantially affecting the oscillation frequencies. On the other hand in Heller and Bliss's model, oscillation frequencies will not change since L is the main factor which determines the travel time of the acoustic wave in the cavity. If L remains the same, oscillation frequencies should remain essentially unchanged. This result shows that Heller and Bliss's model appears to be somewhat better based on the measured results.

To find the relation between L/H and the strength of power spectra, two comparisons were made by considering three cavities which were L/H = 3 (H = 1 inch), 4 (H = 1 inch), 4 (H = 0.75 inches), 5 (H = 0.6 inches), and 6 (H = 0.5 inches). Two points were chosen to represent the strongest oscillations on the

cavity floor and the RW, shown in figures 3.8(a) and (b). The chosen point on the cavity floor was the point F10 or the 17th point for different cases. The second point was the point R7 for all cases.

<i>L/H (L=3 inches)</i>	<i>Frequency Modes</i>	<i>Difference %</i>
4	f_1	-2.33
4	f_2	-2.03
4	f_3	3.77
4	f_4	0.57
5	f_1	-6.98
5	f_2	-4.28
5	f_3	10.24
5	f_4	5.54
6	f_1	-6.98
6	f_2	-6.53
6	f_3	11.75
6	f_4	10.52

Table 3.3 Difference (%) from the Standard Cavity ($L/H=3$)

From figure 3.8(a), as L increased from 3 to 4 inches ($H = 1$ inch) the strengths of all modes were enhanced. By comparing their strongest modes, the strength was enhanced by a factor of about 3. The reason for the increase is that the longer cavity can get more high energy inflow from the SL impingement. With L fixed at 3 inches, H varied from 1 to 0.5 inches such that L/H varied from 3 to 6. Except for the case $L/H = 4$ ($H = 0.75$ inches), the levels of strongest modes were close to each other, which were around 1.4 to 1.7×10^{-6} $(\text{psi})^2/\text{Hz}$. As for the case $H = 0.75$ inches ($L/H = 4$), the level of the 3rd mode was enhanced to near 5.0×10^{-6} $(\text{psi})^2/\text{Hz}$.

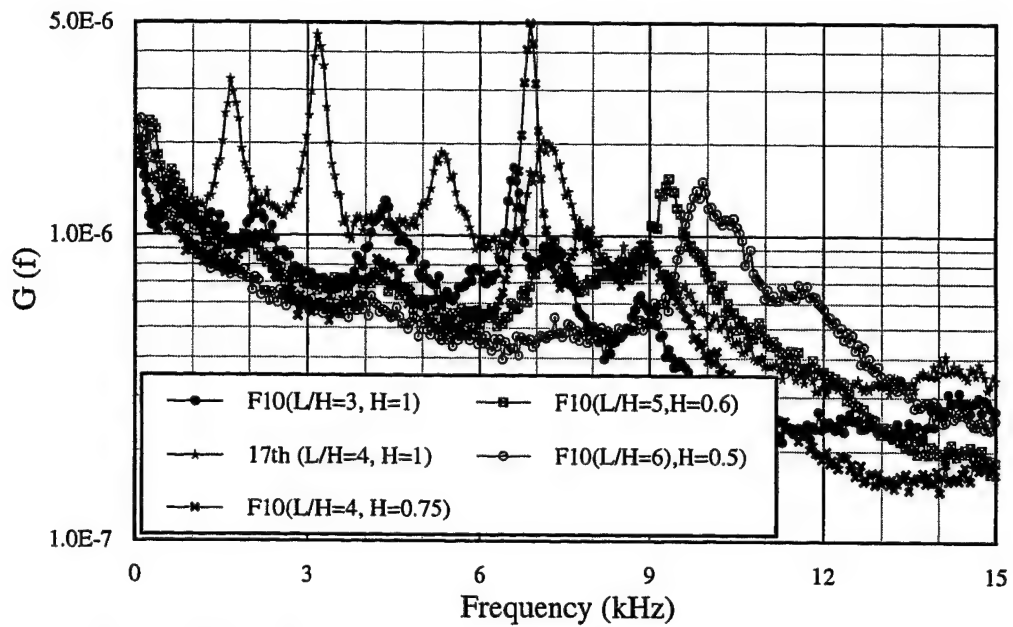


Figure 3.8(a) Power Spectra at Points F10 and 17th for Cavities
($L/H=3, 4$ ($H=1$)), 4 ($H=0.75$)), 5 ($H=0.6$), & 6 ($H=0.5$))

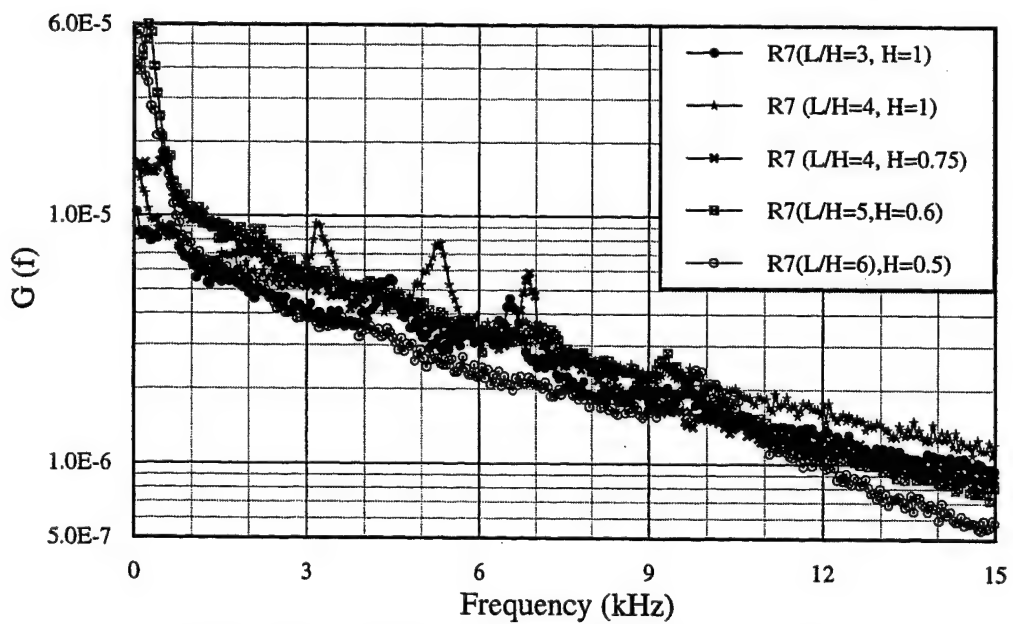


Figure 3.8(b) Power Spectra at Point R7 for Cavities
($L/H=3, 4$ ($H=1$)), 4 ($H=0.75$)), 5 ($H=0.6$), & 6 ($H=0.5$))

From figure 3.8(b), at point R7 the strongest mode of the cavity $L/H = 4$ ($H = 1$ inch) was about 1.7 times of that of the case $L/H = 3$ ($H = 1$ inch). With L fixed at 3 inches, except for the case $L/H = 4$ ($H = 0.75$ inches), the strongest-mode levels were attenuated as H increased. As for the case $H = 0.75$ inches ($L/H = 4$), the level of the 3rd mode was enhanced to near 5.9×10^{-6} $(\text{psi})^2/\text{Hz}$. No consistent tendency for the oscillation strength was obtained with variations of H . Since the impingement flow supplies the energy to sustain the flow oscillation inside the cavity, the waved SL can induce stronger pressure oscillations. Therefore the longer the cavity is, the stronger the pressure oscillations are. This observation will be discussed further in section 3.5.

3.5 COMPRESSIBILITY EFFECT ON THE SHEAR LAYER

Due to compressibility effects, the growth rate of the mixing layer at high convective Mach number is significantly less than that of an incompressible mixing layer at the same velocity and freestream density ratios. Convective Mach number, M_c , is the Mach number convecting with the velocity of the main vortex structures of the SL, and has been shown to be a suitable correlation parameter for the SL growth rate. M_c is defined as $\Delta U/(a_1 + a_2)$.

Quantity	Upper Shear Layer	Lower Shear Layer
γ	1.4	1.4
M	4.95	0
U_∞	765 m/s	0 m/s
Re_∞	$48 \times 10^6 / \text{m}$	$0 / \text{m}$
P_0	$2.275 \times 10^6 \text{ N/m}^2$	4560 N/m^2
T_0	355 K	323 K
P	4560 N/m^2	4560 N/m^2
T	60.2 K	323 K
a	155.5 m/s	360.3 m/s
ρ	0.264 kg/m^3	0.0492 kg/m^3
M_c	1.483	1.483

Table 3.4 Flow Conditions of the Shear Layer

In order to find the compressibility effect on the disturbance excited by the acoustic wave striking the FW, the growth rate for the compressible SL needs to be investigated. The cavity SL was modeled by considering the relatively quiet flow inside the cavity as the lower speed flow part and the SL above the cavity as the higher speed flow. Then, all values of parameters in the formula of $\delta'_{\text{pit},0}$ can be computed to calculate the growth rate of the SL disturbance, δ'_{pit} . (Note: $\delta' = \frac{d\delta}{dx} \equiv \text{SL growth rate}$) Based on the assumption of a mixing layer, the flow conditions of the SL are set as in Table 3.4.

From the previous equation for the growth rate of δ'_{pit} for the incompressible SL $\delta'_{\text{pit},0}$ can be calculated as follows

$$\delta'_{\text{pit},0} = 0.14 \frac{\left(1 - \frac{U_2}{U_1}\right) \left(1 + \left(\frac{\rho_2}{\rho_1}\right)^{1/2}\right)}{1 + \frac{U_2}{U_1} \left(\frac{\rho_2}{\rho_1}\right)^{1/2}} = 0.14 \left(1 + \left(\frac{0.0492}{0.264}\right)^{1/2}\right) = 0.2$$

Then, at $M_c = 1.5$, $\beta = 0.2$ and the growth rate of δ'_{pit} for the compressible SL is

$$\delta'_{\text{pit}} = 0.2(\delta'_{\text{pit},0}) = 0.2(0.2) = 0.04$$

The growth of disturbance for the case $L/H = 3$ ($L = 3$ inches) is estimated below

$$\delta_{\text{pit}} = \delta'_{\text{pit}}(\Delta x) = 0.04(3) = 0.12 \text{ (inches)}$$

For a longer cavity, $L/H = 4$ ($L = 4$ inches), the δ_{pit} is calculated as 0.16 inches similarly. Since points R7 and R6 are 0.125 and 0.25 inches below the top of the RW, then point R6 is too deep to be reached by the disturbed SL, *i.e.*, the shock foot. If this SL were not compressible, the δ_{pit} would be 5 times that of the compressible case, *i.e.*, $\delta_{\text{pit}} = 0.6$ and 0.8 inches for $L/H = 3$ and 4 respectively.

Since the disturbance growth is very small, it is very possible that there is little

room for the shedding vortex to develop. Therefore the constrained disturbance growth in the compressible case is an additional evidence supporting Heller and Bliss's model for this flow. A further investigation of the penetration of the shock foot into the cavity will be discussed in the next section.

3.6 IMPINGEMENT SHOCK DETECTION

As noted earlier, the main difference between the two models used to predict oscillation frequencies is that Heller and Bliss assumed that the acoustic/compression wave reflected from the FW rather than the shedding vortices was the cause of the impingement "event" on the RW. However, both agree that the SL impingement event on the upper RW causes the acoustic wave which induces or enhances the upstream-going acoustic wave. This event can generate a sharp pressure spike in the impingement area. To capture the pressure spike, a conditional sampling code was used (Perng and Dolling, 1996). Then an ensemble-averaging algorithm was applied to examine the self-sustaining oscillation cycle in the cavity.

Since the impingement region is restricted to the upper part of the RW, points R5, R6, and R7 on the RW are of interest. In Perng (section 4.2) figures 4.3 and 4.4 showed the mean shock event duration and the mean interval duration respectively for a range of data window sizes from 101 to 651 points for the case $L/H = 3$ ($L = 3$ inches). For the case $L/H = 4$ ($L = 4$ inches), both quantities at points FW1, F10, R5, R6, and R7 are shown in figures 3.9(a) and (b).

From figures 4.3 and 4.4 for the case $L/H = 3$ both the mean event and interval durations at point R7 became stable as the number of points in the window size exceeded about 200. It should be noted again that the optimum window size should be properly selected. On this basis the appropriate window size was chosen to be 291 points. For this window size, the mean interval durations were 1281, 733, and 292 μ sec at points R5, R6, and R7 respectively. Similarly, the mean

event durations were 9.2, 12.4, and 20.9 μ sec respectively. Defining the persistence of the mean event duration as the ratios of the mean event duration to the mean interval duration, the persistences at R5, R6, and R7 were 0.72%, 1.69%, and 7.16% respectively. From the large variation in the durations and persistences from point R5 to point R7, this suggested very strongly that the shock foot seldom penetrated as deep as point R6 or further downward on the RW. It appears that, on the RW, the top point (R7) was the deepest point which the impingement could reach. At R7, the mean event interval of 292 μ sec corresponded to a 3.43 kHz oscillatory frequency which was in between the 1st (2.15 kHz) and 2nd (4.44 kHz) frequency modes. If the above result is not coincidental, it probably means that the 1st and 2nd mode frequencies are the dominant frequency modes for the shock event also.

For the $L/H = 4$ case, at point R7 the mean interval was about 421 μ sec corresponding to a 2.38 kHz oscillatory frequency which was also in between the 1st (1.66 kHz) and 2nd (3.17 kHz) frequency modes. Similarly, the mean event durations were 12.1, 12.8, and 20.9 μ sec respectively. Persistences at R5, R6, and R7 were 1.96%, 1.54%, and 4.80% respectively. Thus in this case the shock foot also only penetrated as deep as point R7. The persistence at R7 of the case $L/H = 4$ was about 3/4 times of that of the case $L/H = 3$, which corresponded to the inverse of the length ratio of the two cavities. For a longer cavity, the travel time for the acoustic wave is expected to be longer and the impingement frequency is lower than that of a shorter cavity. Accordingly, a lower persistence, 4.80%, at R7 was obtained for the case $L/H = 4$ ($L = 4$ inches).

In addition, the approximate location, R7, of the shock foot was also predicted in section 3.5 based on compressible SL growth rate data (Papamoschou & Roshko, 1988). The convective number, M_c , in this case was 1.48 and the growth of the SL between FW and RW was estimated to be only 0.16 inch for the case $L/H = 4$ ($L = 4$ inches) due to the compressibility effect. Since points R7 and R6 were 0.125 and 0.25 inches below the top of the RW, then point R6 was too deep to be reached by the shock foot.

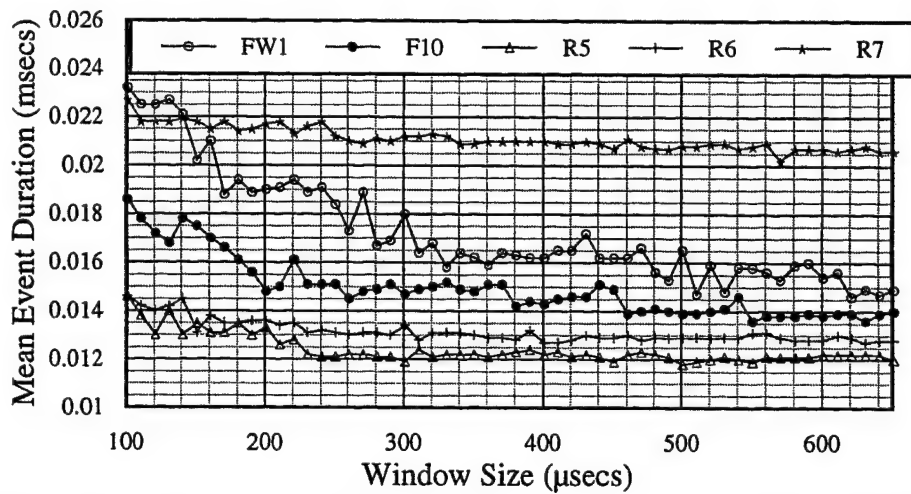


Figure 3.9(a) Mean Event Duration vs Window Size (L/H=4, L=4 inches)

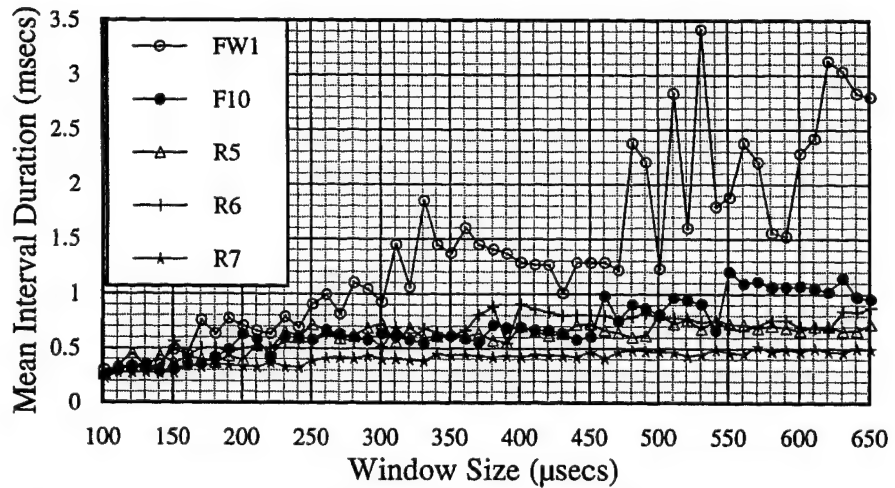


Figure 3.9(b) Mean Interval Duration vs Window Size (L/H=4, L=4 inches)

3.7 ACOUSTIC WAVE AND MODEL OF OSCILLATION PREDICTION

In order to find the relation and time delay between the acoustic wave on the FW and the flow impingement on the RW, an ensemble-averaging algorithm was used. A window size, N, fixed at 1024 points (μ secs) and the maximum pressure point of the trigger channel was set at $\tau = 0$. Two cavities, one being the baseline case and the other one equipped with a plate separator, with the same ratio of L/H=3 (L=3 inches) were examined. The separator-equipped cavity was designed

such that the impingement flow was prevented from going into the cavity by the plate separator.

For the baseline case, initially the signal from point R7 on the RW was selected as the trigger channel. Ensemble averages computed on FW1 and R7 are shown in figures 3.10(a) and (b) respectively. The triggering event on R7 around $\tau = 0$ is very evident. In figure 3.10(a), there are two maxima either side of $\tau = 0$. The one on the left is 223 μ secs earlier than the impingement event on R7 and the one on the right is about 232 μ secs after the impingement event. In the next computation, FW1 was selected as the trigger channel and ensemble averages computed on FW1 and R7. Results are shown in figures 3.11(a) and (b). The triggering event is not as pronounced as on R7 but is still evident. In figure 3.11(b), two peaks are also obvious. The left one is 211 μ secs earlier and the right one is 226 μ secs later than when the acoustic wave impinges on the FW at $\tau = 0$. These two data sets show quite clearly how the shock impingement event generates an acoustic wave which moves upstream to the FW and a downstream-going acoustic wave precedes a shock impingement.

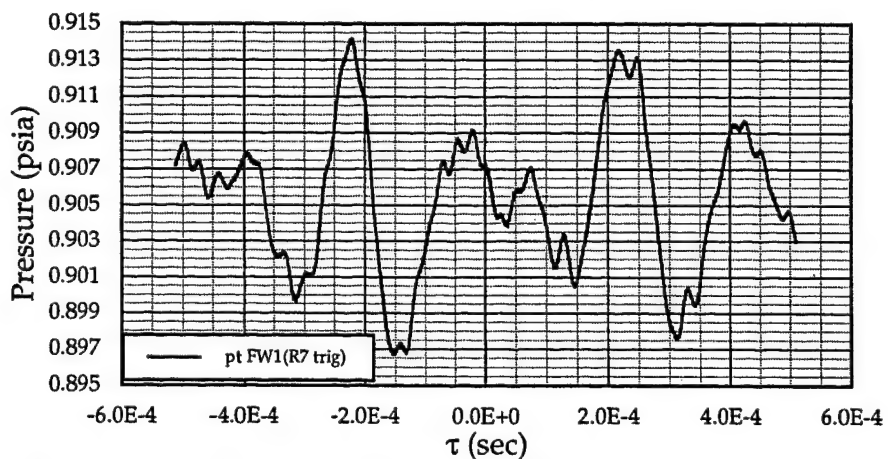


Figure 3.10(a) Ensemble Average at Point FW1 (R7 as Trigger) (L/H=3)

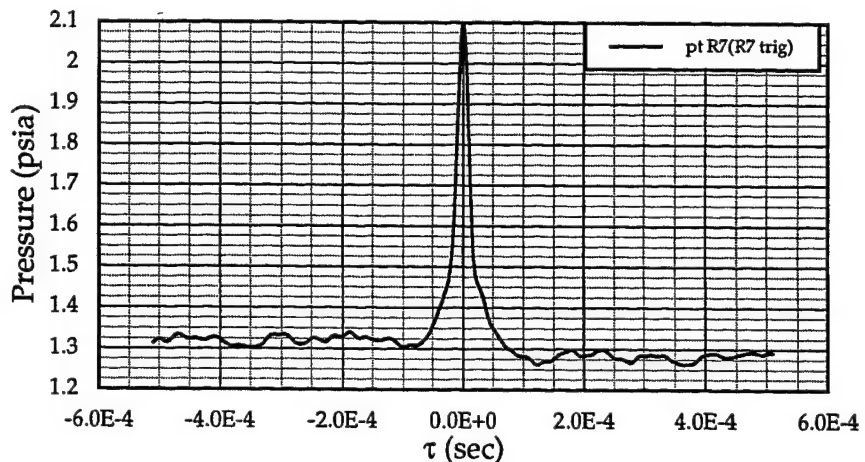


Figure 3.10(b) Ensemble Average at Point R7 (R7 as Trigger) (L/H=3)

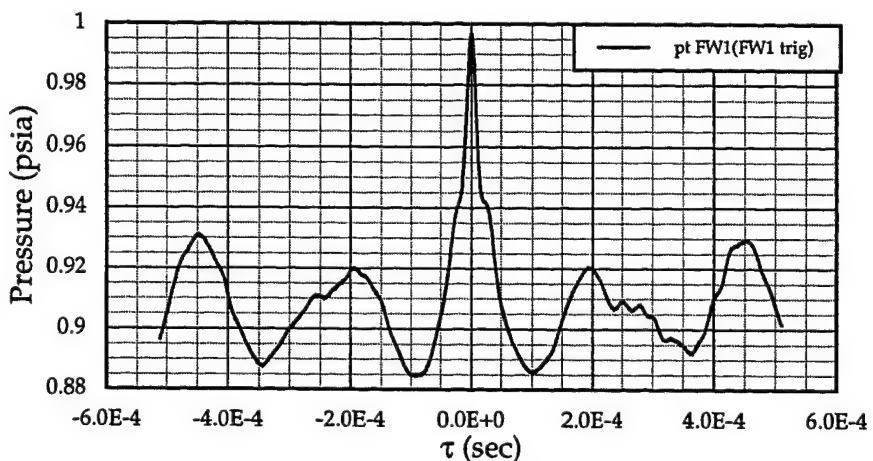


Figure 3.11(a) Ensemble Average at Point FW1 (FW1 as Trigger) (L/H=3)

Additional evidence for such a cycle comes from the cross correlation of FW1 and R7 as shown in figure 3.12. The two peaks A & B on either side of $\tau = 0$ are at $\tau = -216$ and $226 \mu\text{secs}$ respectively. As mentioned earlier the time for the acoustic wave to travel from the RW to the FW is $212.5 \mu\text{secs}$ based on the adiabatic temperature (320 K). The actual temperature inside the cavity is smaller than 320 K due to the flow of the cavity vortices. In this case, the measured travel time of the acoustic wave is a little larger. All ensemble-averaging results and the cross correlation of points FW1 and R7 suggest that the explanation of the self-

sustaining oscillation process offered by Heller and Bliss (1975) in which it is the acoustic/compressive waves reflected off the FW rather than shedding vortices which induce the impingement event is more likely. If this is true, the deflection of the SL is probably induced by the acoustic pressure wave as suggested by Heller and Bliss (1975) and if there is a shedding vortex it is an affiliated phenomenon on the pressure wave.

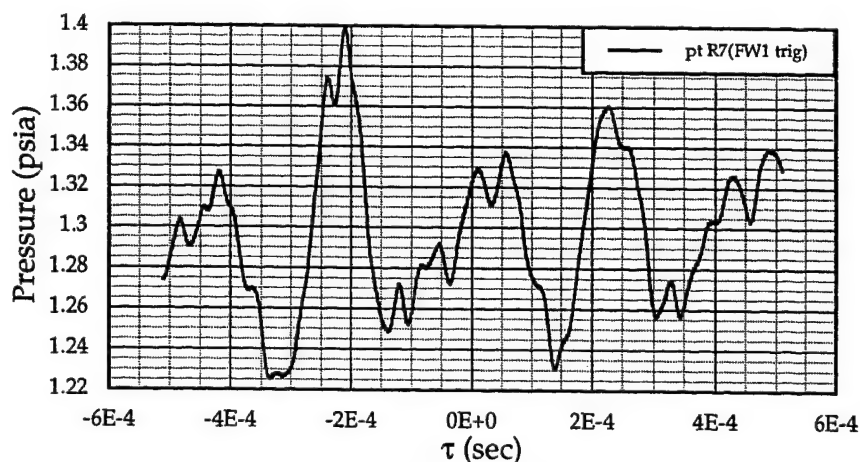


Figure 3.11(b) Ensemble Average at Point R7 (FW1 as Trigger) (L/H=3)

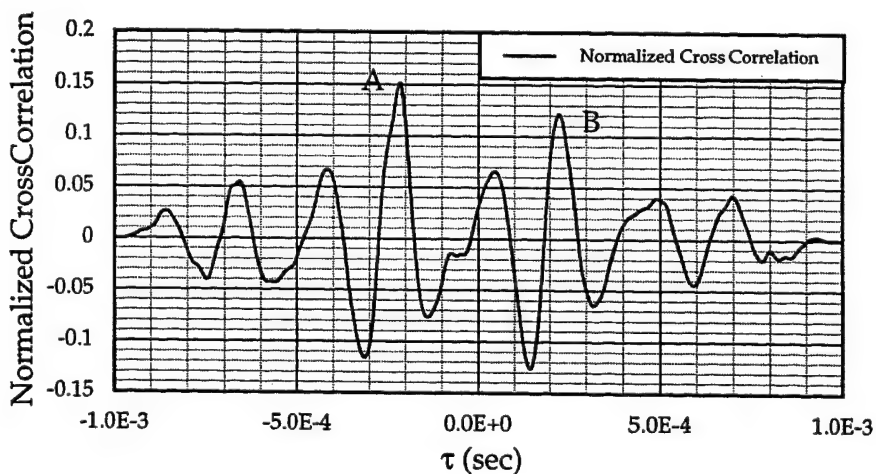


Figure 3.12 The Normalized Cross Correlation of Points FW1 & R7 (L/H=3)

Since the trailing-edge vortex is very strong, moves randomly in all directions, and nonuniformly expands/contracts, the cross correlations of pressure signals on the cavity floor with either point FW1 or R7 are difficult to analyze. In their computational investigation, Tam *et al.*, (1996) found that the upstream moving acoustic wave was reflected from the rear corner forced by a pressure pulse (*i.e.*, recompression effect) caused by a flow impingement on the top of the RW. Instead of the impingement event, the recompression process generated an upstream going acoustic wave (Tam *et al.*, 1996). In order to examine the effect of the recompression on the acoustic wave, a special cavity arrangement was designed as follows. If the impingement event can be isolated from the cavity, there will be no impingement flow entering the cavity such that no recompression effect can occur around the rear corner. Further without the high energy flow, the cavity flow should be more stable than the baseline case. Under such conditions, it was hoped that the cross-correlations and ensemble-averaging calculations would show more clearly the motion of the acoustic waves in the cavity.

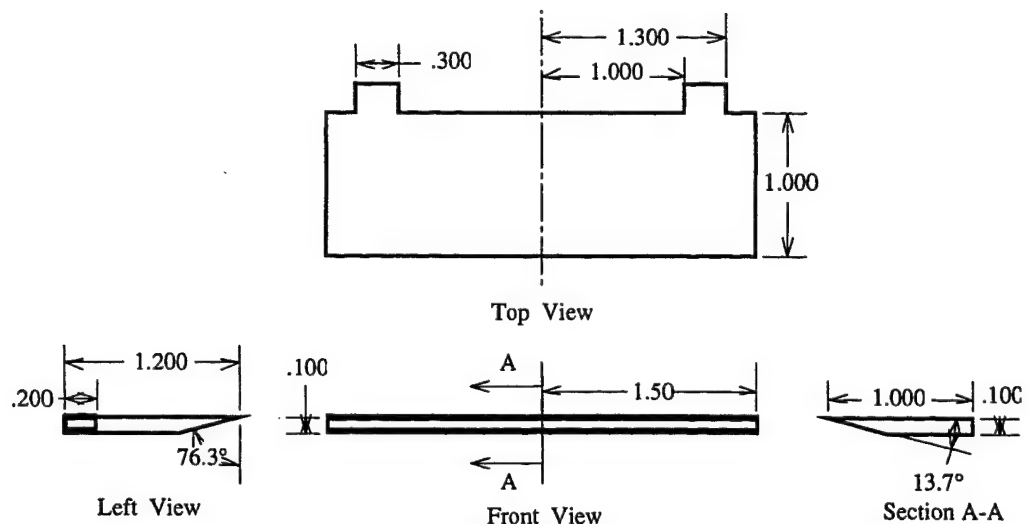


Figure 3.13(a) Plate Separator (L/H=3)

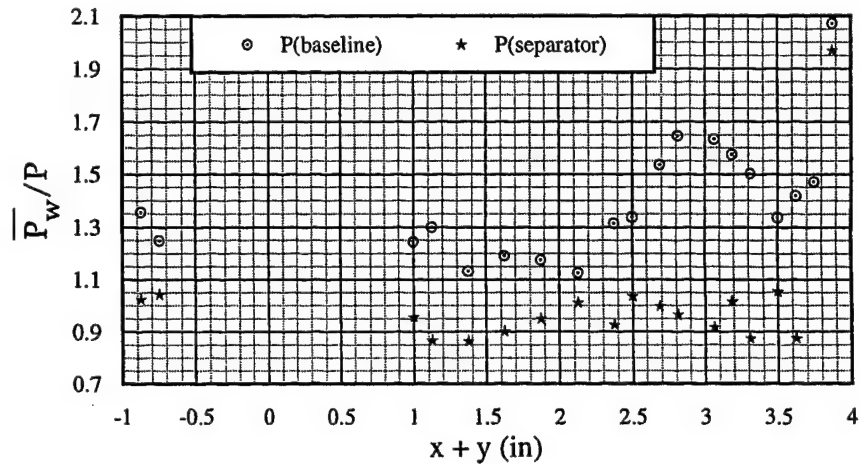


Figure 3.13(b) Mean Pressure Distribution of Cases, L/H=3 (L=3 inches)

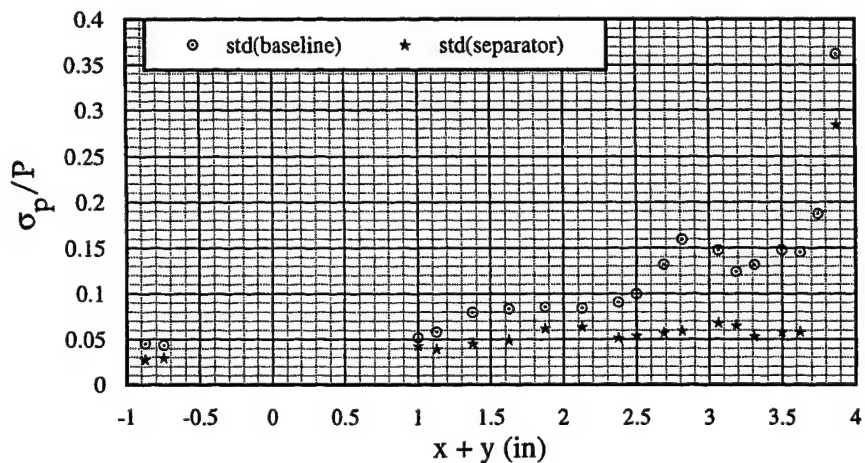


Figure 3.13(c) Standard Deviation Distribution of Cases, L/H=3 (L=3 inches)

A plate separator (1.0 in. x 3.0 in. x 0.125 in.), as shown in figure 3.13(a), was attached to the RW 0.25 inches below the top edge to prevent the shock foot going into the cavity directly. Since the separator was 1 inch long in the streamwise direction, the impingement flow should not be able to pass by the separator leading edge and to flow into the cavity. The measured mean pressures and standard deviations are shown in figures 3.13(b) and (c). In the pressure distribution, except the point R7(3.875), all mean pressure values are within the range of (0.95 ± 0.1) psia. There is no evidence that a strong vortex exists in such a cavity which has no concave pressure distribution on its floor. From figure 3.13(c), the

normalized standard deviation distribution clearly shows that a cavity flow with a plate separator is very quiet compared to the baseline case. However a weaker vortex might be formed inside. Usually, the evidence of the existence of a vortex at a point is that a higher standard deviation and a lower mean pressure occur simultaneously. According to this criterion, a weak vortex was recognized near the rear corner (around points F9(2.6875), F10(2.8125), and R1(3.0625)).

From the conditional sampling calculation, the mean event and interval durations at points FW1(-0.875), R1, R5(3.625), and R7 are shown in figures 14(a) and (b). The mean value of the interval duration at point R7 has a plateau approximately from 311 to 591 μ secs of window size. Since the window size, 591 μ secs, was close to its mean interval duration (601.6 μ secs), T_1 's at point R7 and FW1 were chosen to be 1.962 and 0.739 psia respectively at this window size. Then the mean event durations were 9.6 and 13.1 μ secs at points FW1 and R7 respectively. It should be noted that the chosen duration (601.6 μ secs) is larger than that of the baseline case and this difference was caused by the plate separator which interfered with the instability of the SL and the flow impingement frequencies on the point R7. Since the plate separator largely isolated point R7, point FW1 was then selected to be the *trigger* channel. The results are shown in figures 3.15(a), (b), and (c).

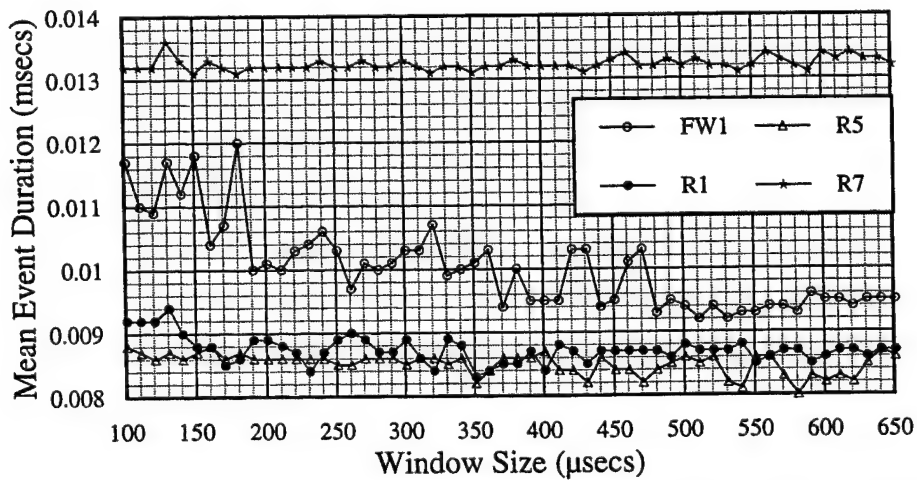


Figure 3.14(a) Mean Event Duration vs Window Size ($L/H=3$ with a Separator)

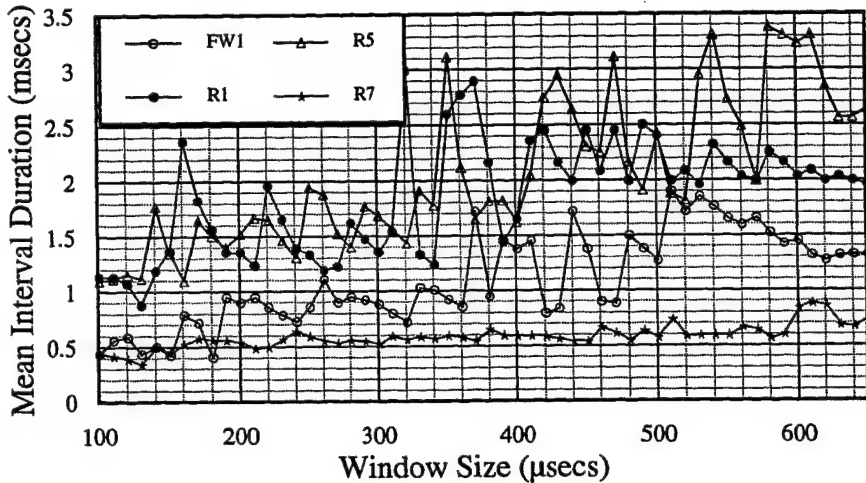


Figure 3.14(b) Mean Interval Duration vs Window Size (L/H=3 with a Separator)

From figure 3.13(c), the standard deviation at point FW1 is obviously smaller than at other points, which means the flow near this point is relatively quiet. Therefore, the acoustic wave could be extracted easily and the ensemble averaging result at point FW1 (shown in figure 3.15(a)) looks periodic and symmetric about the center point, $\tau = 0$. All other points had a maximum at time delays between -80 and -230 μ secs. Exact time delays for those peaks, which correspond to the time for the acoustic wave to travel from the other points to point FW1, are listed in Table 3.5.

In this table, the passage of the traveling acoustic wave is very evident from the data in the time-delay column. The time delays calculated from the ensemble averaging algorithm are very close to the calculated travel time based on the theoretical adiabatic wall temperature. Since the plate separator prevented the impingement flow going into the cavity directly, no recompression happened around the rear corner. This result does not agree with the computational investigation of a supersonic cavity flow from Tam *et al.* (1996). Nevertheless the acoustic wave was caught successfully, which was not evident in the baseline case due to the existence of the strong trailing-edge vortex. The time delay between

points FW1 and R7 demonstrates the relation of the flow impingement and the generation of the acoustic wave on the top of the RW again.

<i>Point</i>	<i>Time Delay of the Left Maximum (μsec)</i>	<i>Horizontal Distance (inch)</i>	<i>Traveling Time of Acoustic Wave (μsec)</i>
<i>F1</i>	-73	1.000	-70.8
<i>F2</i>	-80	1.125	-79.7
<i>F3</i>	-93	1.375	-97.4
<i>F4</i>	-103	1.625	-115.1
<i>F5</i>	-120	1.875	-132.8
<i>F6</i>	-141	2.125	-150.5
<i>F7</i>	-150	2.375	-168.2
<i>R1</i>	-208	3.000	-212.5
<i>R2</i>	-206	3.000	-212.5
<i>R4</i>	-210	3.000	-212.5
<i>R5</i>	-207	3.000	-212.5
<i>R7</i>	-223	3.000	-212.5

Table 3.5 The Calculated Time Delay between Point FW1 and Other Points

In addition, normalized cross correlations between FW1 and other points showed that time delays were similar to the results of the ensemble-averaging algorithm. For brevity, only the cross correlation between FW1 and R7 is shown in figure 3.16. The left and right maxima are located at $\tau = -230$ and 240 μ secs respectively. These time delays correspond to oscillation frequencies of 4.35 and 4.17 kHz which are very close to the 2nd mode frequency, 4.35 kHz. The 2nd mode frequency shows that only two acoustic waves exist in a cavity. The distance between these two waves is about the cavity length. Their moving directions are opposite. In addition, by considering those left and right three consecutive peaks the time delays were -387, -230, -67, 74, 240, and 393 μ secs respectively. The

differences of two consecutive peaks are 157, 163, 141, 166, and 153 μ secs respectively and these time differences correspond to oscillation frequencies of 6.37, 6.14, 7.09, 6.02, and 6.54 kHz respectively. The averaged value of these five oscillation frequencies is 6.432 kHz which is very close to the 3rd mode frequency (6.59 kHz). The 3rd mode frequency shows that only two consecutive and same-direction acoustic waves exist in a cavity. These two waves must move in the same direction (*i.e.*, downstream or upstream). About the 1st mode frequency, there can only be one acoustic wave inside a cavity for both directions. Therefore the travel time required for the 1st mode wave is double of that of the 2nd mode wave. The definition of the travel time for the 1st mode is different from other higher modes. The specific travel time is the time required to move around a cycle between the FW and the RW for the wave, *i.e.* two times of 212.5 μ secs. By considering the time-delay peaks, every four peaks can constitute the time delay of the 1st mode waves. They are (387+74), (230+240), and (67+393) μ secs. The average value is 463.7 μ secs which corresponds to 2.16 kHz, *i.e.*, the 1st mode frequency. These 1st and 3rd modes could not be detected by using the ensemble averaging algorithm. The algorithm only sensed the event which corresponded to the event which happened earlier or later on the other wall. Therefore the time delay detected from the algorithm was always close to 212.5 μ secs. Overall, this distinct and useful cross correlation can be attributed to the quiet cavity flow with a plate separator. For the baseline case the cross correlations were dominated by both the strong trailing-edge vortex and the acoustic wave, and had no such periodic peaks like the separator case.

With the help of the plate separator to eliminate the strong trailing-edge vortex, the passage of the acoustic wave and relations of oscillation frequencies were made seen. From the investigation of both the baseline cavity and the cavity with a plate separator, there is some evidence that the acoustic wave instead of the shedding vortex is the main factor causing the flow impingement and vice versa in this study. The acoustic wave also provoked the higher modes of the pressure oscillation in the cavity.

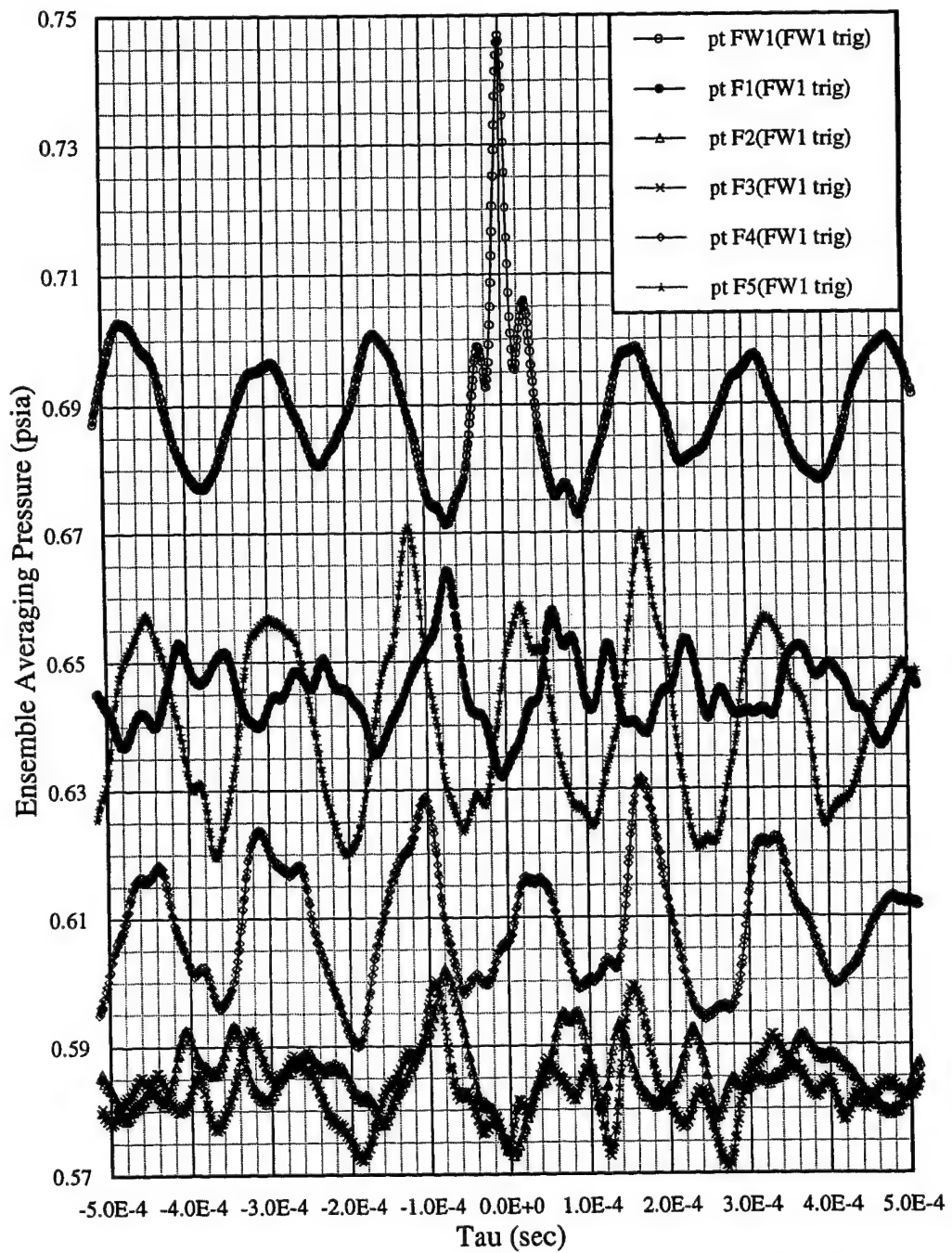


Figure 3.15(a) Ensemble Average of the Case L/H=3 with a Plate Separator
(FW1 as Trigger)

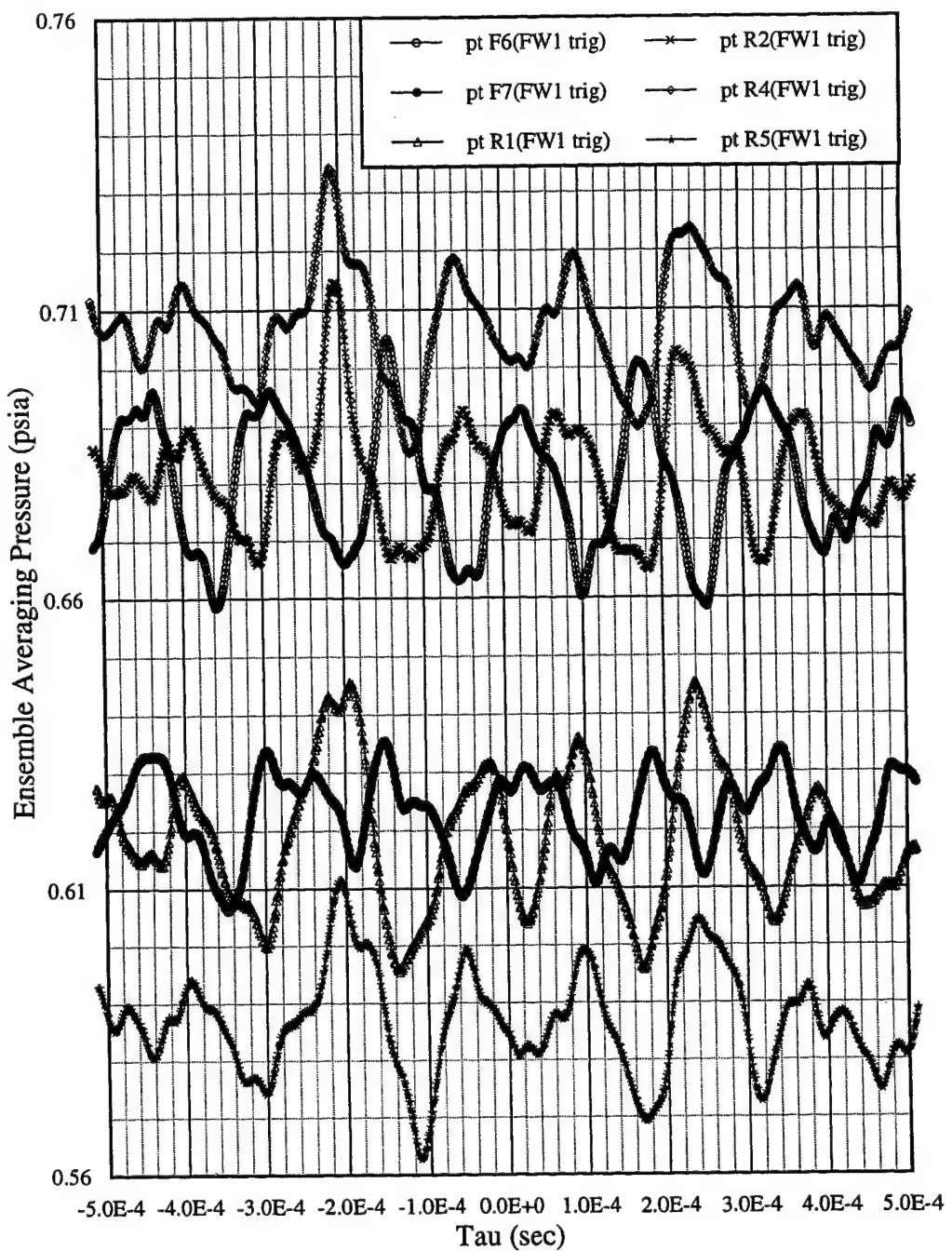


Figure 3.15(b) Ensemble Average of the Case L/H=3 with a Plate Separator
(FW1 as Trigger)

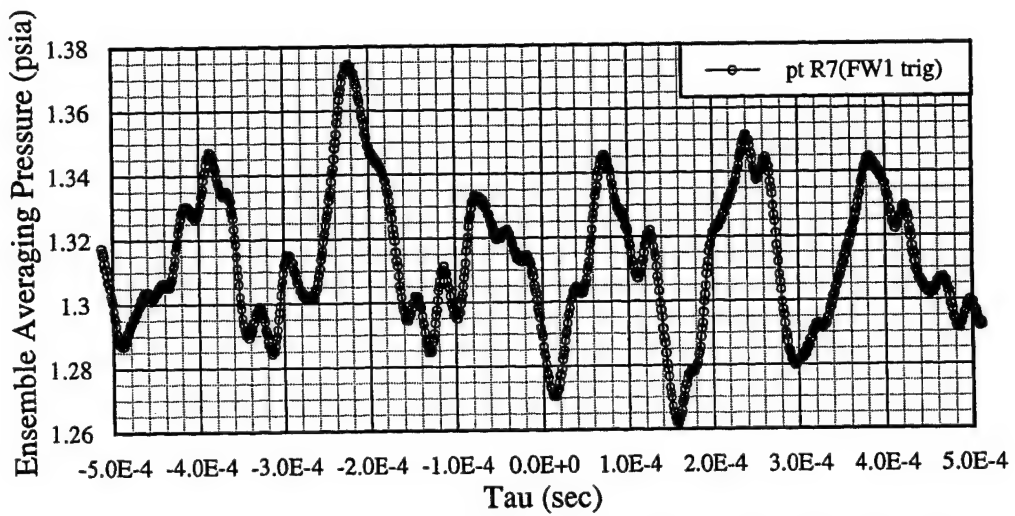


Figure 3.15(c) Ensemble Average of the Case L/H=3 with a Plate Separator
(FW1 as Trigger)

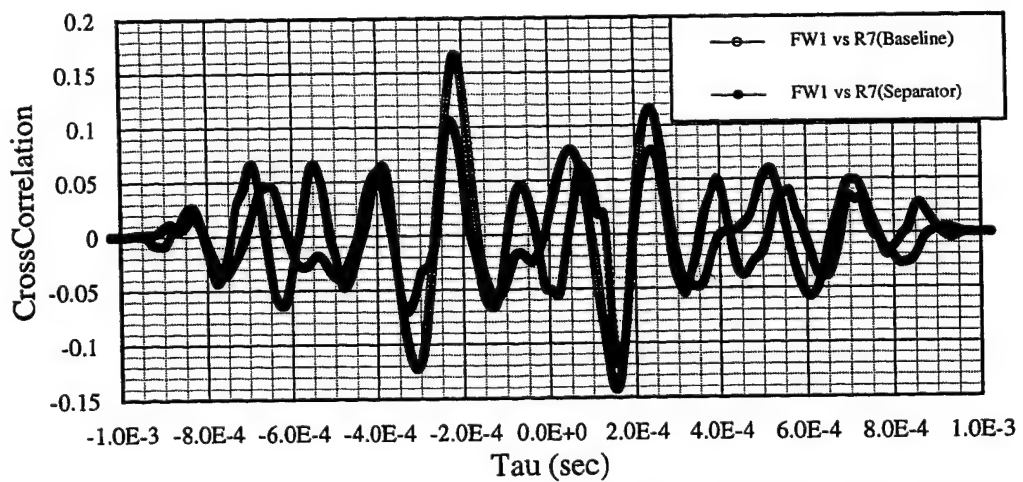


Figure 3.16 Cross Correlation between Points FW1 and R7 of the Case L/H=3

Chapter 4: Passive Control Investigation

All the passive control geometry variations were explored for both $L/H = 3$ & 4 . From the discussion of the previous chapter, the acoustic wave, the SL impingement, and the large trailing-edge vortex are the most important phenomena which can affect the pressure oscillations in the cavity. Changes of the FW and RW geometries were made to investigate their effect on the acoustic wave and the flow impingement. Two BL spoilers were attached to the tunnel floor upstream of the cavity to explore their effect on the generation of the shedding vortex (if there was any) and the SL. Finally, two obstacles were placed on the cavity floor in order to alter the shape of the trailing-edge vortex.

4.1 EFFECTS OF CHANGES IN FRONT WALL GEOMETRY

According to Rossiter, when an acoustic wave strikes the FW, a shedding vortex is excited and convects downstream. Heller and Bliss proposed that the reflected acoustic wave from the FW instead of the shedding vortex is the cause of the flapping SL and the flow impingement. In either case, the FW is important in the oscillation cycle. Therefore changes to the geometry of the FW surface were examined. Power spectra for the vented and slotted FWs at points F6(2.125) and F10(2.8125) are shown in figures 4.1(a) and (b) for $L/H=3$. The baseline spectra are shown for reference. From these two figures, except for the 3rd mode at point F10 of the vented-FW case, the strength of oscillation modes was enhanced. Those irregular surfaces do not attenuate the acoustic wave or the generation of the shedding vortex in this study. And the stable compressible SL was possibly disturbed and excited by the irregular top edge of the slotted FW and the upstream porous surface of the vented FW.

4.2 EFFECTS OF CHANGES IN REAR WALL GEOMETRY

Since SL impingement is the most important source supplying energy to the cavity flow and generating the forward-going acoustic wave, it is anticipated

that reducing or blocking this inflow should be the most effective way to control the amplitude of the pressure fluctuations.

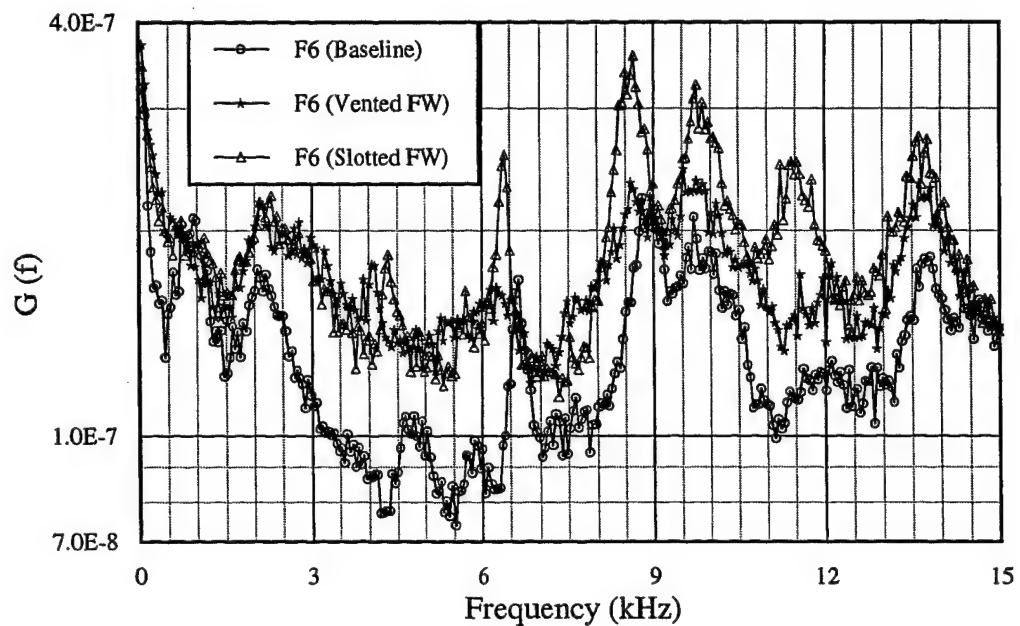


Figure 4.1(a) Power Spectra at Point F6 with Modified FWs (L/H=3)

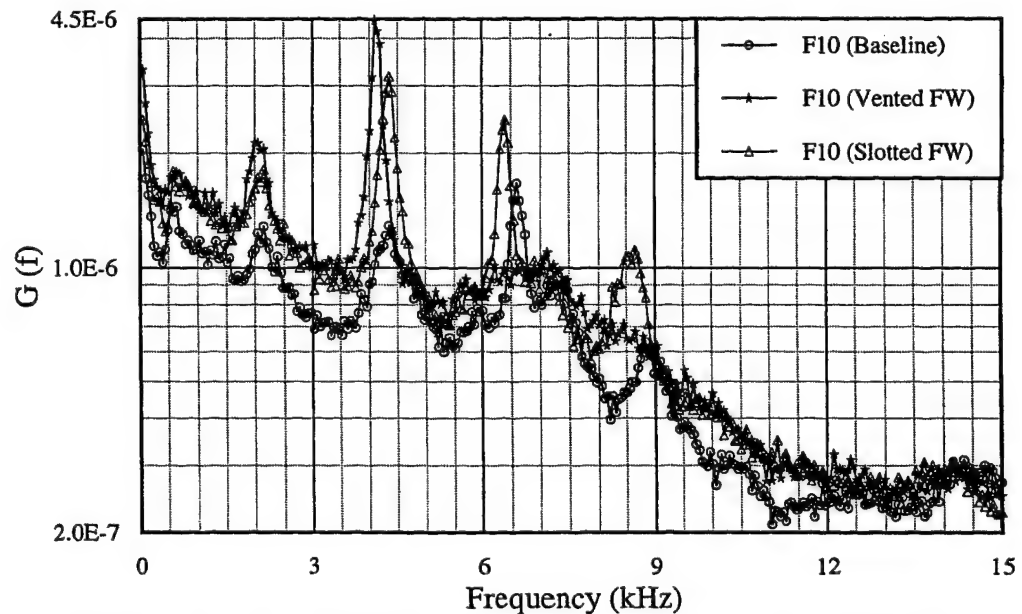


Figure 4.1(b) Power Spectra at Point F10 with Modified FWs (L/H=3)

Power spectra for the baseline and the four modified RWs (slanted #1, vented, slotted, and beak) are shown in figures 4.2 and 4.3 for $L/H=3$ & 4 respectively. For clarity, only data at points F1(1.0) & F10(2.8125) for $L/H = 3$ and the 1st(2.0) & 17th(3.8215) points for $L/H = 4$ are shown. These correspond to stations on the floor at which the weakest & strongest pressure oscillations occurred. For the baseline case the ratio of the strongest power levels at points F1 and F10 for $L/H = 3$ is about 14. Similarly the ratio for $L/H = 4$ is 10.5. At point F1 (figure 4.2(a)) with the slanted RW1, the 2nd and the 3rd modes are attenuated by factors of about 3.6 & 1.5. At point F10 (figure 4.2(b)), the power levels of the 1st & 2nd modes are decreased by factors of about 7.6 & 5.1, but the 3rd mode is almost unaffected. Unfortunately, the 3rd mode is stronger than the 1st & 2nd modes in the baseline flow for $L/H = 3$. For $L/H = 4$, the slanted RW1 is more effective at the 17th point even for the 3rd and 4th modes which are attenuated by factors of about 2 as shown in figure 4.3(b). If comparing the highest strength mode (the 2nd mode) of the baseline cavity and the highest strength mode (the 3rd mode) with a slanted RW1, the attenuation factor is about 5. Since the edge surface of a slanted RW1 was not parallel to the FW surface, the induced acoustic wave was directed towards the outflow from the slanted surface, not directly towards the FW. In addition, the flow impingement angle was reduced and the high speed flow more easily “escaped” downstream. Since the impingement point occurred a little bit further downstream on the slanted surface, slightly smaller oscillatory frequencies were obtained.

Recall that the intent of the vented RW was to conduct air from the high-pressure region around the RW to the lower pressure region downstream of the cavity and, hopefully, attenuate oscillation amplitudes of the resonant cavity flow. The slotted RW was designed as an attempt to interfere with the acoustic wave (which was thought to be responsible for disturbing the SL and exciting the shedding vortex). From the results for $L/H = 3$ shown in the figure 4.2, these two methods are not as effective as the slanted RW1 and even serve to amplify the 2nd and 3rd modes at point F1. Only the 1st mode is attenuated significantly for the slotted RW at point F10. For $L/H = 4$, the strength of the 2nd mode at the 1st

point (figure 4.3(a)) is decreased by about a factor of 2 with other modes largely unchanged. At the 17th point, by comparing the strongest modes, the 2nd mode in the baseline cavity is attenuated by a factor of about 2.2 compared to the 2nd mode of the vented RW case and to the 3rd mode of the slotted RW case. Clearly, these two methods do not work as expected.

The cavity control methods discussed above are 2-D modifications to the RW geometry. Since the cavity flow is a complicated 3-D phenomenon, it seems logical to use an appropriately shaped 3-D RW to suppress the oscillations. Therefore, a 3-D RW, referred to as the "beak" wall was tested in this study. From figure 4.2(a) it can be seen that the strength of the 1st mode is too weak to be recognized and the amplitudes of both 2nd and 3rd modes are decreased by factors of about 6.5 & 3.5 respectively. If comparing the strongest oscillations, the amplitude of the 2nd mode of the baseline cavity has decreased by a factor of about 6 compared to the 3rd mode with the beak RW control. At point F10, the strengths of the 1st and 2nd modes are attenuated by factors of about 7.8 & 8.5 respectively and the amplitude of the strongest oscillation mode (*i.e.*, the 3rd mode) is decreased by a factor of about 3.5. At the 1st point, for the $L/H = 4$ case shown in figure 4.3(a), the strengths of the 1st & 2nd modes are attenuated at least by factors of 9 & 11.7 respectively but the 3rd mode strength increases slightly. By comparing the strongest modes, the amplitude decreased by a factor of about 2. At the 17th point, the factors of attenuation of the 1st & 2nd modes are about 10.5 & 21 respectively. For the 3rd & 4th modes, the factors are about 3.4 & 3 respectively. If the strongest oscillations in the two cases are compared (*i.e.*, 2nd mode in the baseline case and 4th mode in the beak case) then the attenuation factor is about 6.8. Of these four methods, the 3-D beak RW was the most effective.

Of the previous approaches to control, the 3-D beak RW was the most effective and the slanted RW1 also did a good job. Therefore an effort was refocused on those two RWs with a different 3-D shape and different 2-D slant angles. Opposite to the beak shape, the valley RW was created with its streamwise centerline cut deeper than on its two spanwise edges. The slanted

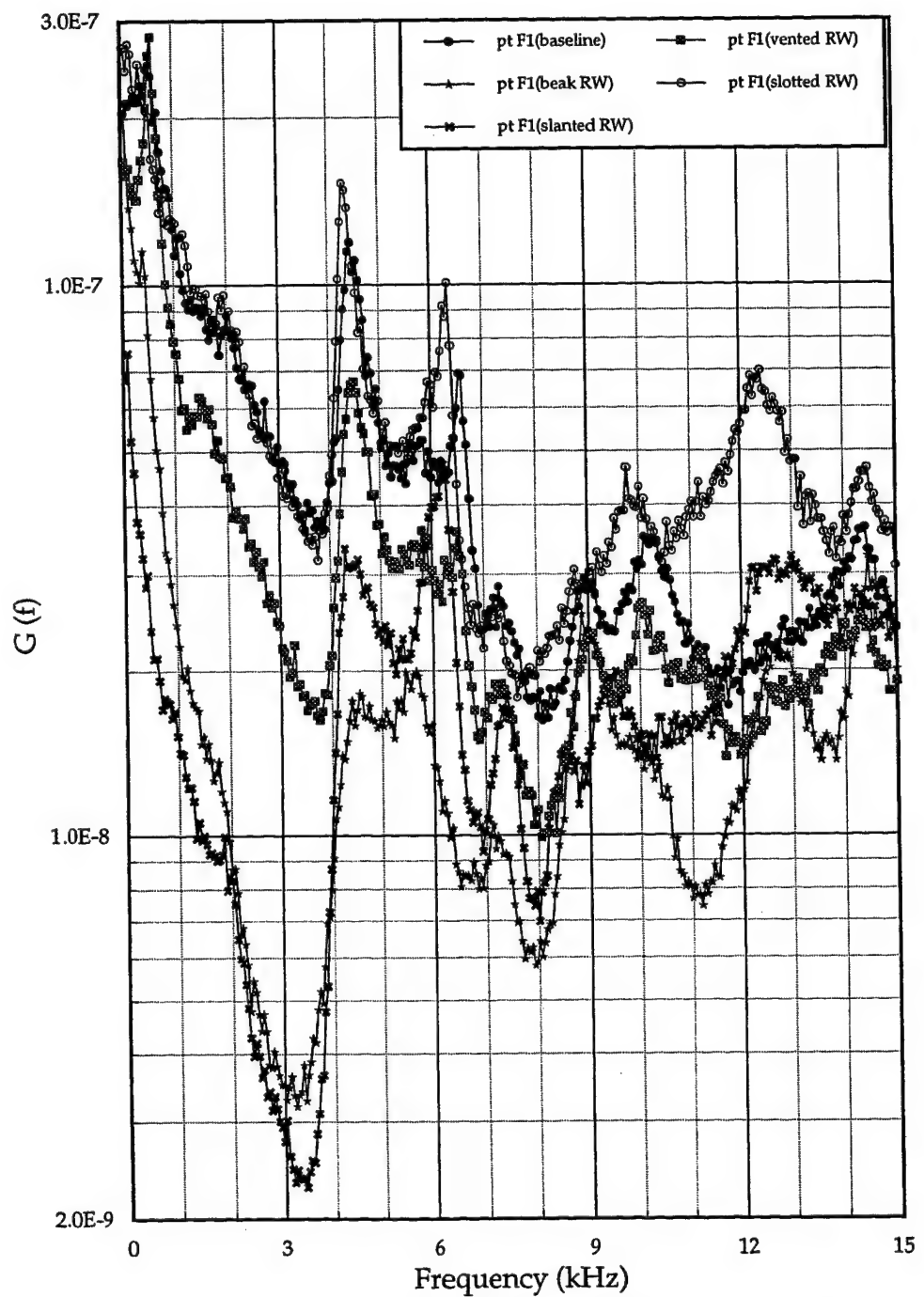


Figure 4.2(a) Power Spectra at Point F1 with Modified RWs (L/H=3)

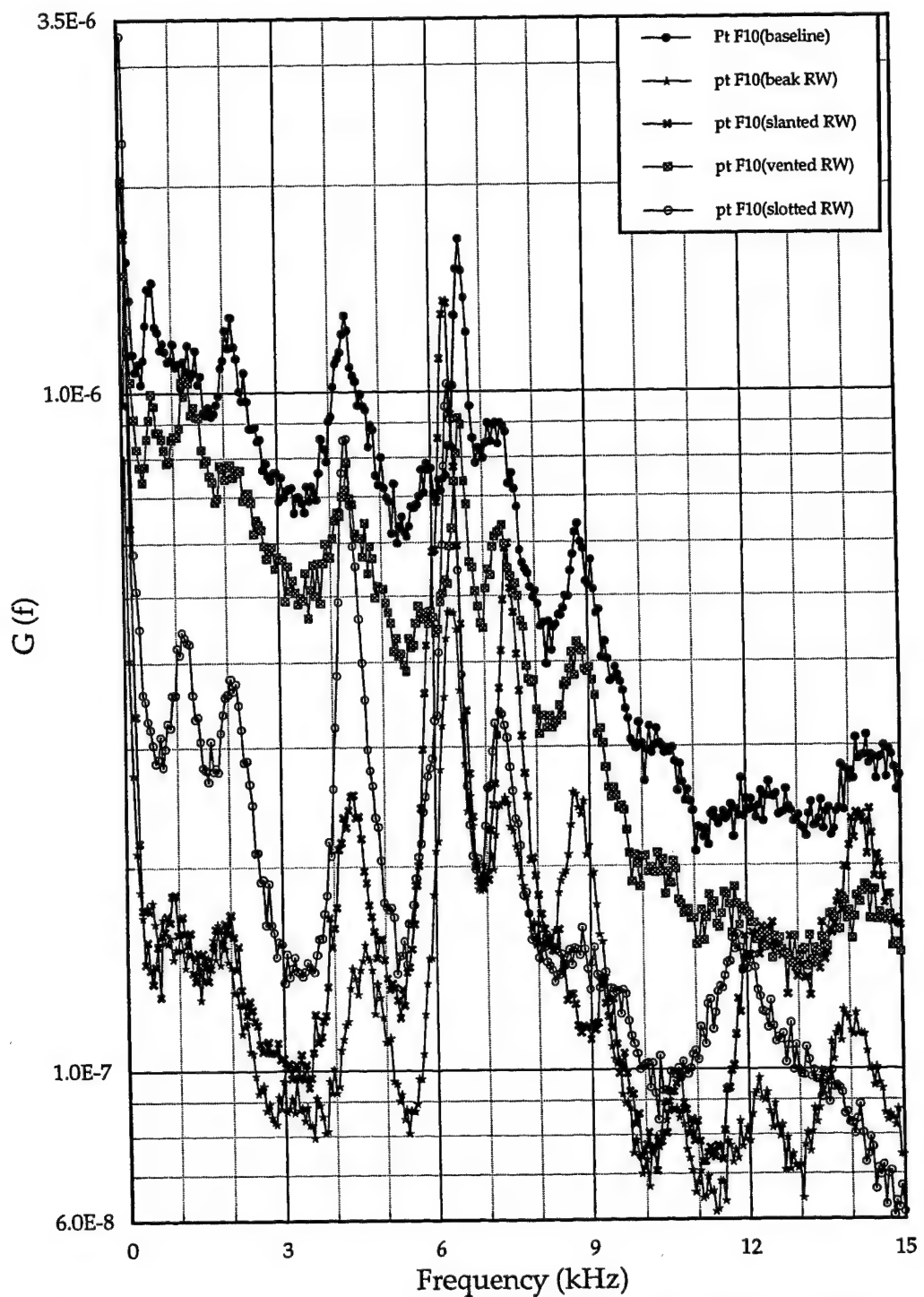


Figure 4.2(b) Power Spectra at Point F10 with Modified RWs ($L/H=3$)

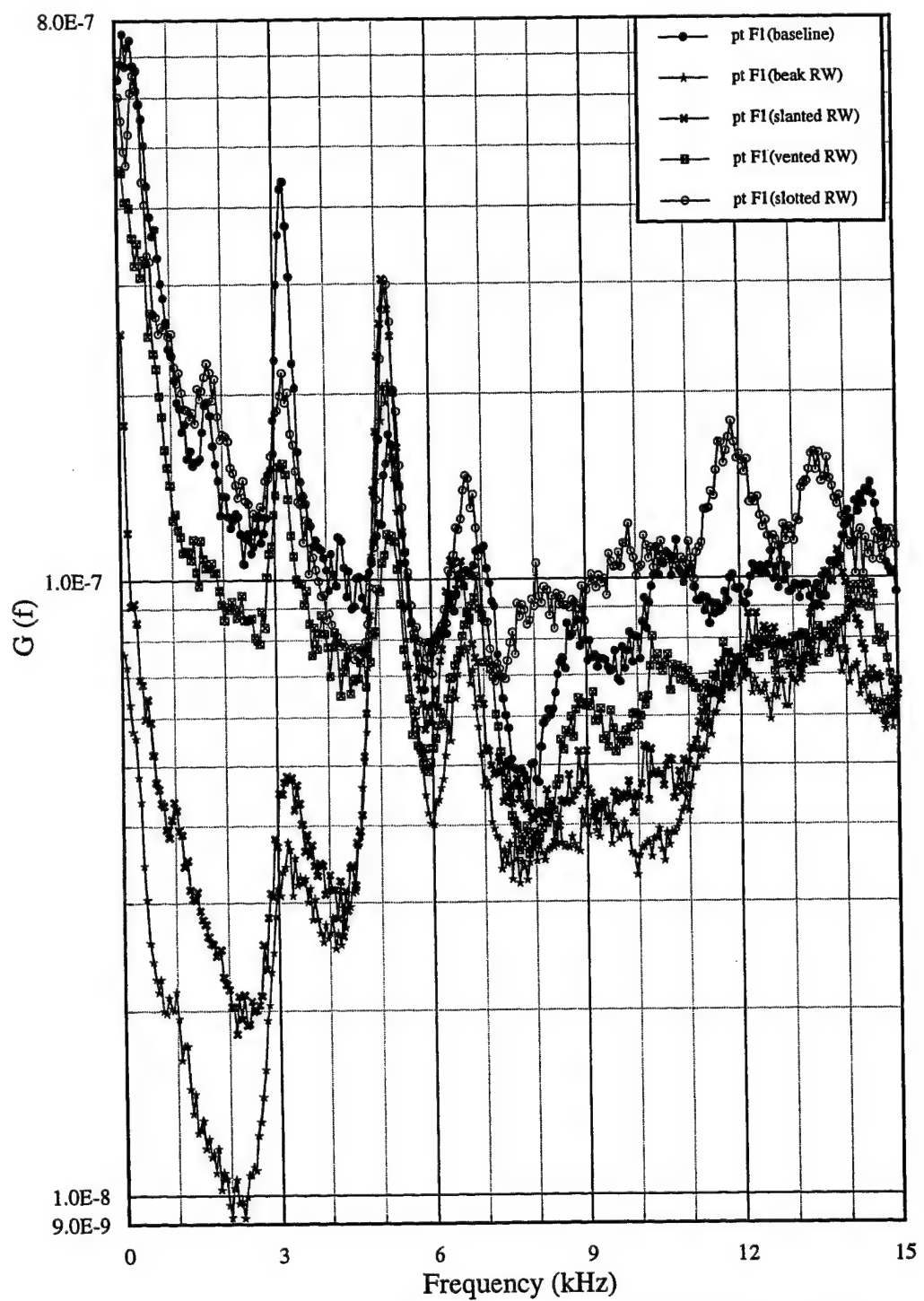


Figure 4.3(a) Power Spectra at Point F1 with Modified RWs (L/H=4)

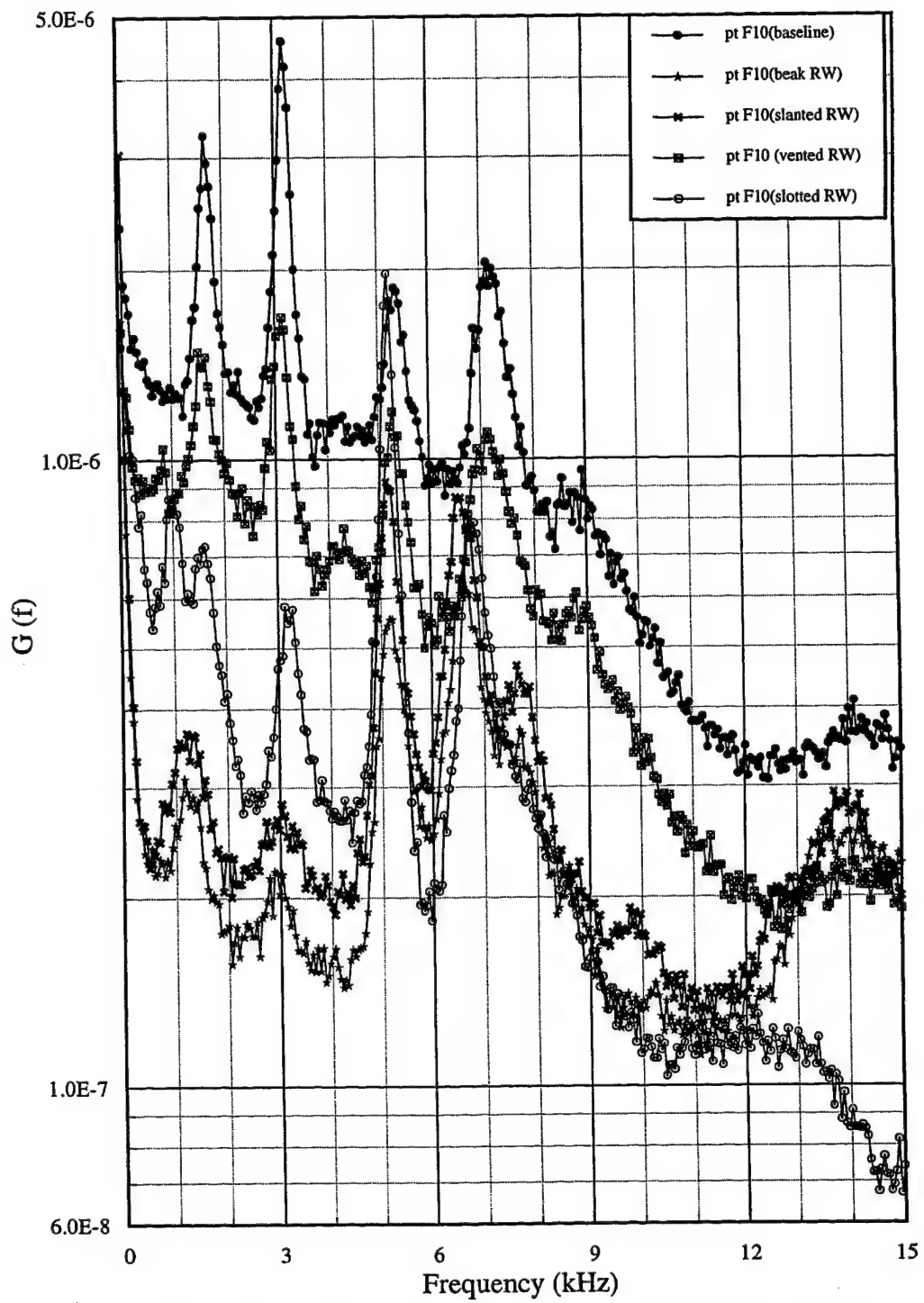


Figure 4.3(b) Power Spectra at Point F10 with Modified RWs ($L/H=4$)

RW2 and RW3 had steeper slant angles of 38.7^0 & 30.2^0 respectively than the angle 45^0 of the slanted RW1 (shown in section 3.2.2). The weakest and strongest power spectra happened at points F1(1.0) & F10(2.8125) respectively for the case $L/H = 3$ and at the 1st(2.0) & 17th(3.8125) points respectively for the case $L/H = 4$. These power spectra distributions are shown in figures 4.4 & 4.5 respectively. It should be noted that the tests of the valley RW, the slanted RW2 & RW3 were done together. Their power spectra around 1 kHz were contaminated by a electronic noise due to a heat-conduction problem in the Dynamics amplifier. After putting a bigger heat sink, the noise was reduced a lot.

By using the beak RW result as a standard, other RWs were evaluated. From figure 4.4(a) for point F1 the attenuation effect of the valley was similar to the beak RW except for small strength increases in the 2nd & 3rd oscillation modes. The slanted RW2 provided better attenuation of the 4th mode with an attenuation factor of about 1.5 compared to the beak RW. For all modes, the slanted RW2 attenuated the oscillation strength such that there was no obvious sharp peak except a spike around 1 kHz. Such a spike was not anticipated and was very likely caused by the electronic noise from the amplifier. For the slanted RW3, a higher peak at the 2nd mode was found. Among these three slanted RWs, the slanted RW2 effectively attenuated the oscillation strength of all modes at point F1.

From figure 4.4(b), the power spectra at point F10 shows that the valley RW enhanced the 2nd, 3rd, & 4th modes by factors of about 2.2, 2.0, & 2.3 respectively. The slanted RW2 enhanced the 2nd, 3rd, & 4th modes by factors of about 1.7, 1.4, & 1.8 respectively. No obvious 1st mode peak was found for both of these RWs. The slanted RW3 enhanced the 1st, 2nd, 3rd, & 4th modes by factors of about 4.9 2.5, 1.1, & 1.8 respectively. No other RWs were more effective than the beak RW in attenuating the oscillations at point F10 which was the location of the strongest oscillation on the cavity floor for the case $L/H = 3$.

For a longer cavity ($L/H = 4$) the power spectrum at the 1st point is shown in figure 4.5(a). The valley RW enhanced the 2nd & 4th modes by factors of about 1.7 & 1.4 respectively. But the 3rd mode strength (the strongest mode) was

weakened by a factor of about 2. The slanted RW2 weakened the 3rd mode by a factor of about 2.9. The 2nd mode was enhanced by a factor of about 1.3. The 4th mode was almost unaffected. For the slanted RW3 the power spectra almost had no obvious peak except a spike at 500 Hz caused by electronic noise. By considering the strongest mode of each method, the slanted RW3 was the best. It attenuated the 3rd mode of the beak RW case by a factor of about 7.6 at the 1st point.

For the strongest oscillation location, *i.e.*, the 17th point, on the cavity floor the power spectra are shown in figure 4.5(b). The valley RW enhanced the 1st, 3rd, & 4th modes by factors of about 2.4, 1.6, & 1.5 respectively. No obvious peak occurred around the 2nd mode. The slanted RW2 enhanced the 1st, 3rd, & 4th modes by factors of about 2.7, 1.4, & 1.2 respectively. The slanted RW3 weakened the 4th mode by a factor of about 1.3 but enhanced the 1st mode by a factor of about 2.4. No obvious peaks were there for the 2nd & 3rd modes. Among the 3 slanted RWs, #3 was the most effective by comparing the strongest oscillations. But no RW could surpass the performance of the beak RW at the 17th point.

In order to attenuate the strongest oscillations, the power spectra at points F10 ($L/H = 3$) & 17th ($L/H = 4$) on the floor are compared with each other to qualify effectiveness of all RW methods. For the case $L/H = 3$, the 3-D beak RW still was the best. It attenuated the 3rd mode (the strongest mode) by a factor of about 3.5. The slanted RW2 & RW3 also worked well and attenuated the 3rd mode by factors of about 2.6 & 2.2 respectively. The 3-D valley RW was not as effective as the slanted RW2 and RW3. It attenuated the 3rd mode by a factor of about 1.8.

For the case $L/H = 4$, the 3-D beak RW was still the best. The strongest mode oscillation (the 2nd mode) in the baseline case was attenuated by a factor of about 6.8 and shifted to the 4th mode. The 2-D slanted RW3 changed the strongest mode of the baseline case to the 1st mode with an attenuation factor of about 6.4. The 2-D slanted RW2 attenuated the strongest mode of the baseline case by a factor of about 5.5 and the 4th mode became the strongest mode.

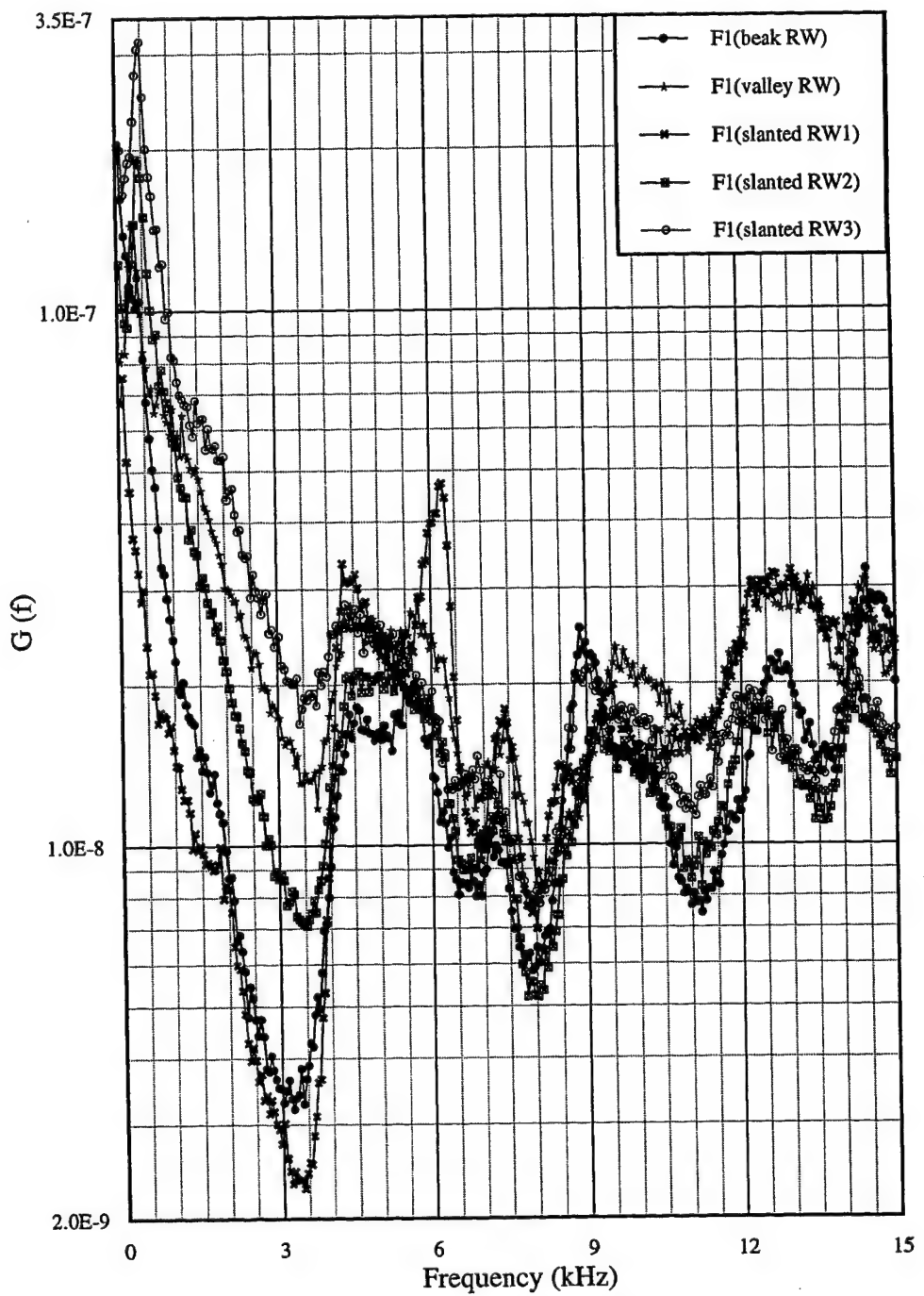


Figure 4.4(a) Power Spectra at Point F1 with Modified RWs ($L/H=3$)

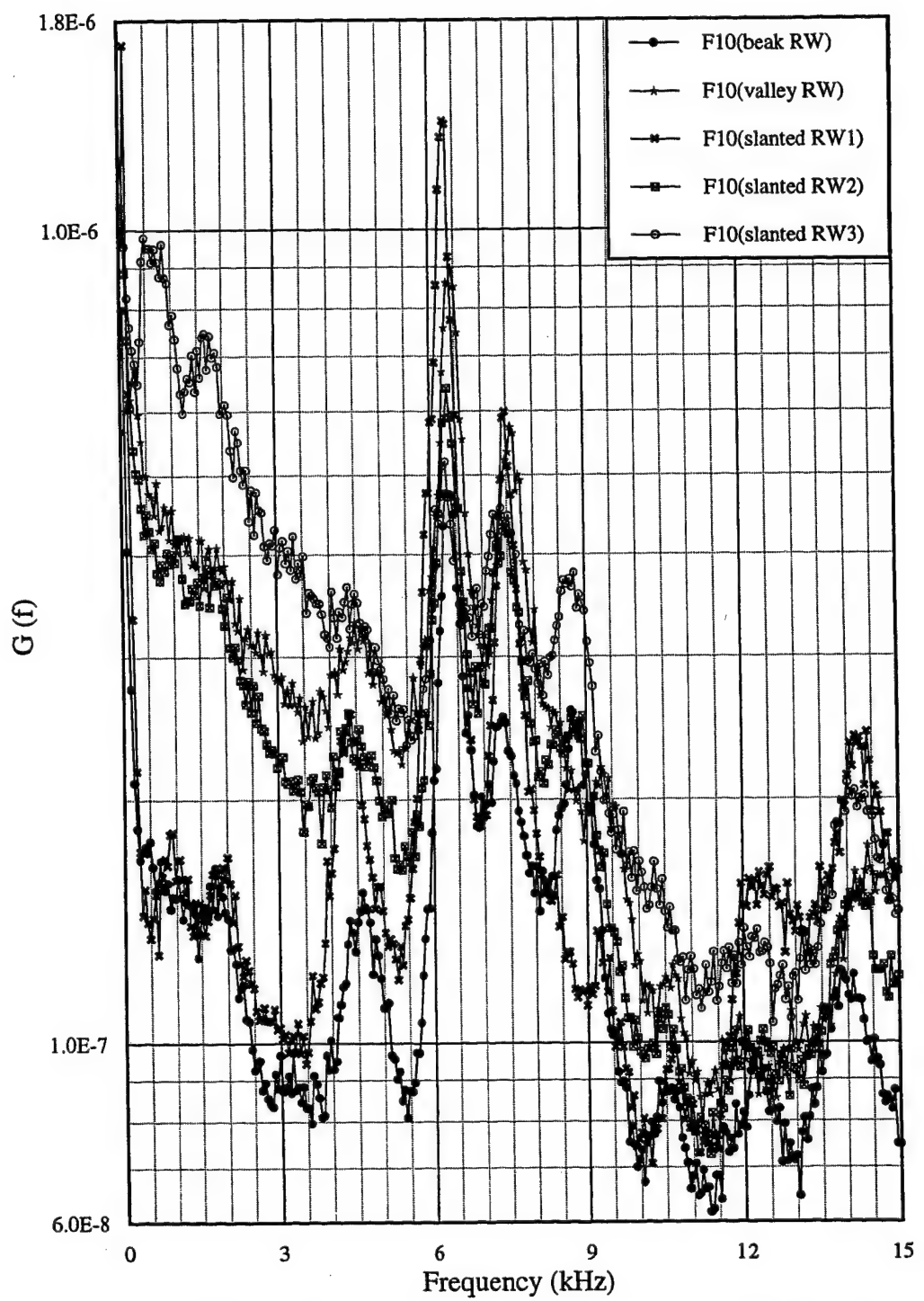


Figure 4.4(b) Power Spectra at Point F10 with Modified RWs ($L/H=3$)

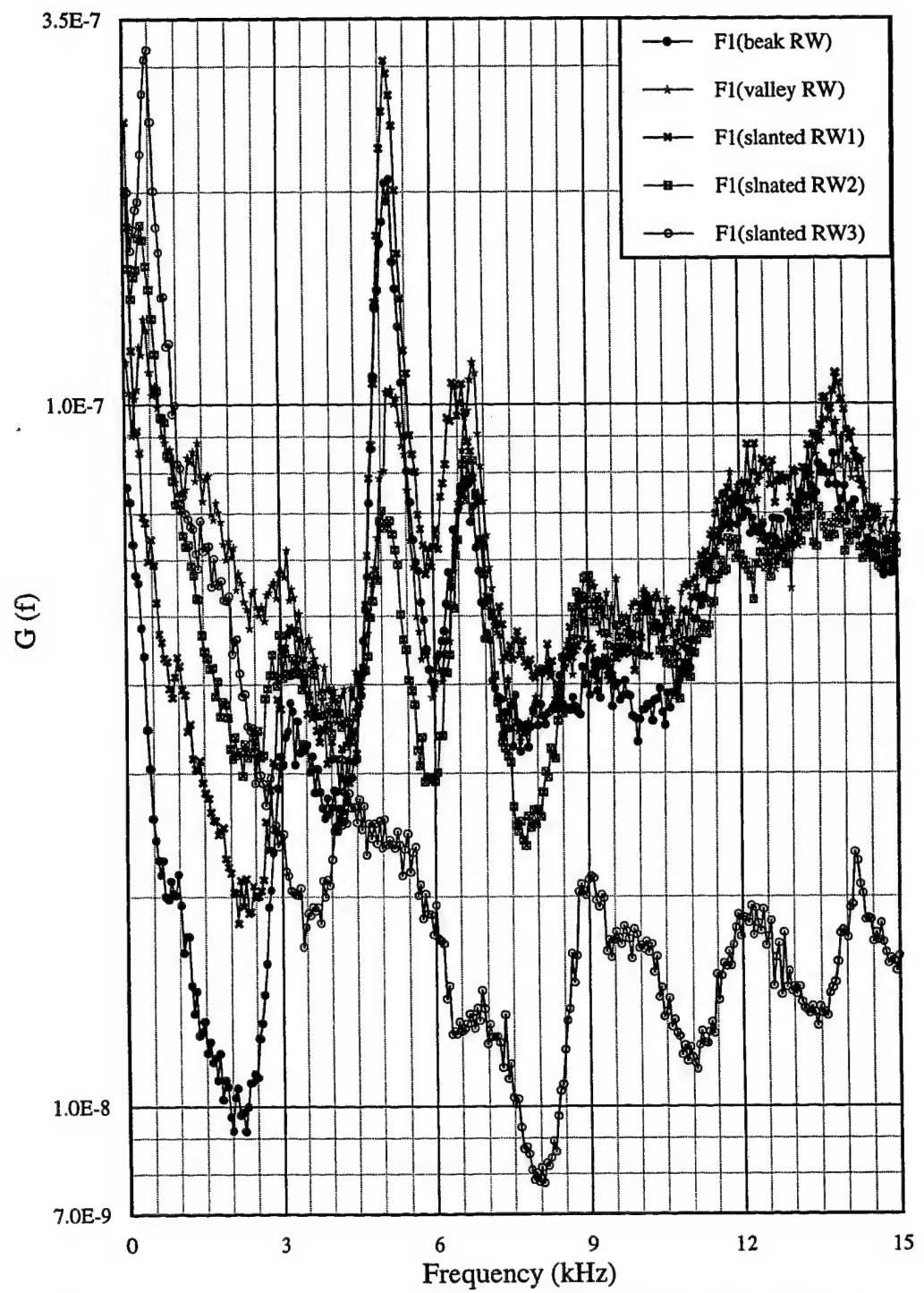


Figure 4.5(a) Power Spectra at Point F1 with Modified RWs ($L/H=4$)

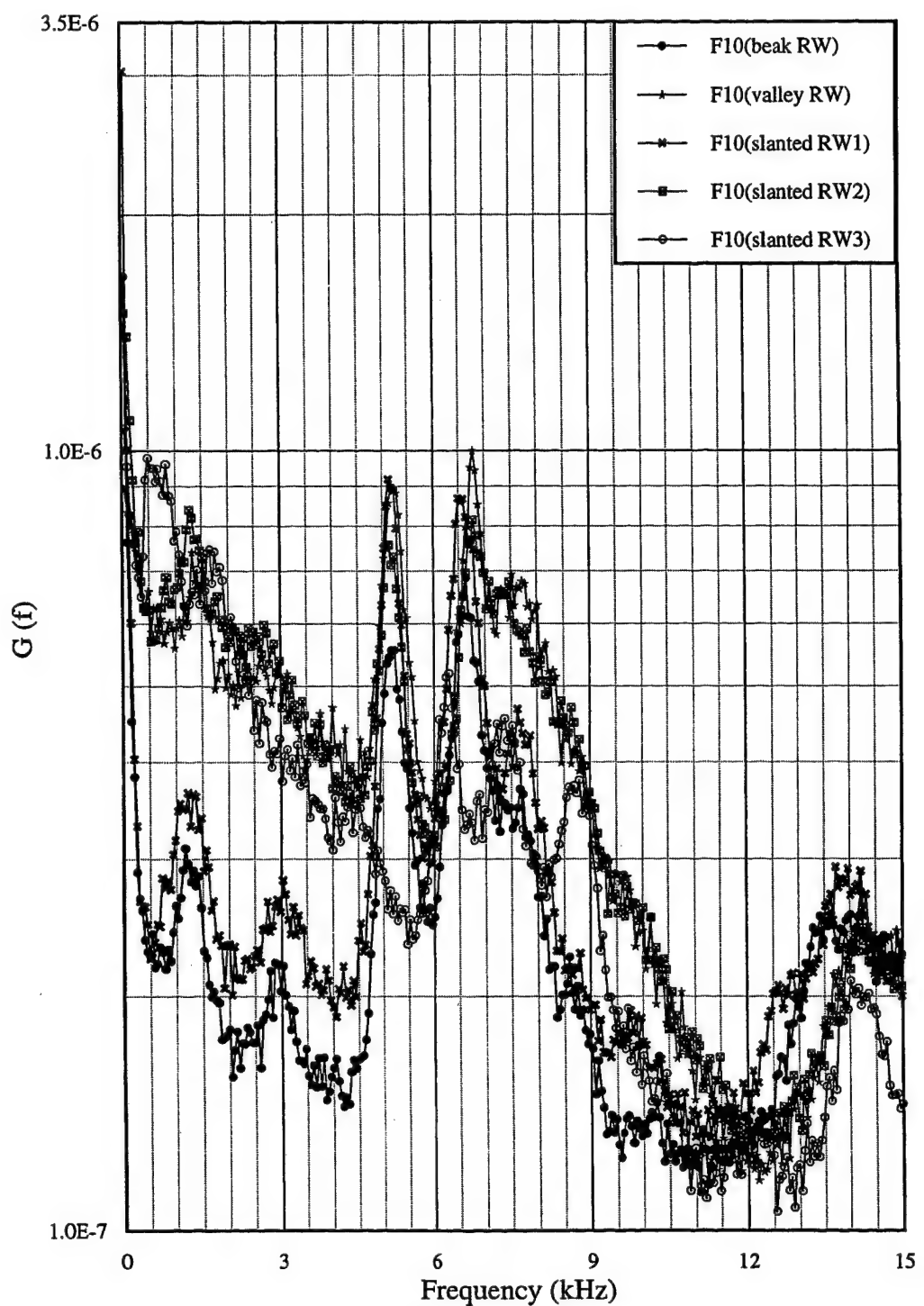


Figure 4.5(b) Power Spectra at Point F10 with Modified RWs (L/H=4)

Among the 3 slanted RWs, #3 was the most effective by comparing the strongest oscillations. The 3-D valley RW attenuated the strongest mode of the baseline case by a factor of about 4.6 and the 3rd mode became the strongest mode.

In all tests, the 3-D beak RW is the most effective, although the attenuation effects of the 2-D slanted RW2 and RW3 are close to that of the beak RW. The slanted RW1 and the 3-D valley RW are not as good as the beak RW. The vented and slotted RWs are not recommended. By reviewing the geometry of all RWs and their effects there are two characteristics of effective RWs. The *first* characteristic is that the RW should have a slant surface with a steeper slant angle ($< 45^0$). Of course, the low edge of the slanted face should be lower than the impingement shock foot. The *second* characteristic is that two edges of the RW should be cut deeper than on the centerline. The combination of these two characteristics is to cut two edges as deep as the cavity floor such that the slant angle on the centerline is less than 45^0 . This is a steeper 3-D beak RW. However for simplicity and for economical reasons, the slanted RW3 is recommended.

4.3 EFFECTS OF INCOMING BOUNDARY LAYER SPOILERS

In this phase of the work, two different BL spoilers were tested. As described in section 3.2.3, they were three Wheeler doublet type vortex generators (VG's) and a BL wedge separator. These spoilers were placed such that their trailing edges were 1 inch ahead of the leading edge of the cavity $L/H = 3$ ($L = 3$ inches). The power spectra at points FW1(-0.875), F10(2.8125), & R7(3.875) are shown in figures 4.6(a), (b), & (c). Since the beak RW was very effective, its results are included for comparison. Near point FW1 the flow was relatively quiet and was dominated by the acoustic wave. From figure 4.6(a) the beak RW significantly attenuated the 1st, 2nd, & 3rd modes by factors of about 3.6, 9, & 4.2 respectively. The 2nd (the strongest) mode of the baseline case was attenuated by a factor of about 6.3 and shifted to the 3rd (the strongest) mode of the beak RW case. In the spoiler methods, the VG's enhanced the 1st mode a lot and weakened the 3rd mode by a factor of about 1.4. The 2nd mode was almost unchanged. The wedge enhanced all modes. Its 1st mode was even stronger than the 2nd mode of the

baseline case. From the above discussion of the point FW1 where the acoustic wave dominated, the beak RW clearly attenuated the strength of the acoustic waves inside the cavity. Both spoilers were ineffective.

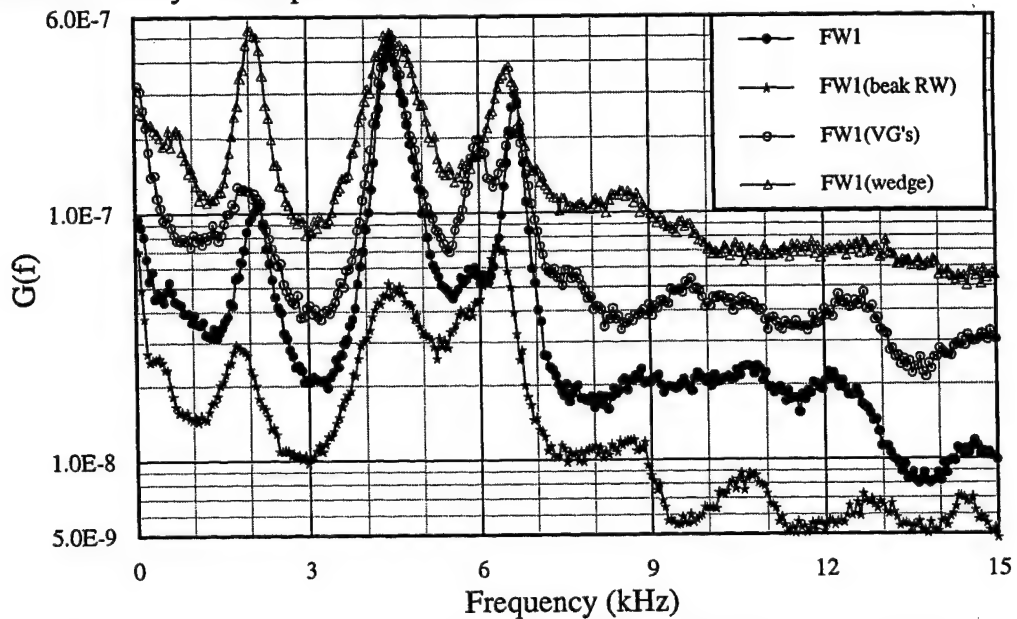


Figure 4.6(a) Power Spectra at Point FW1 with BL Spoilers (L/H=3)

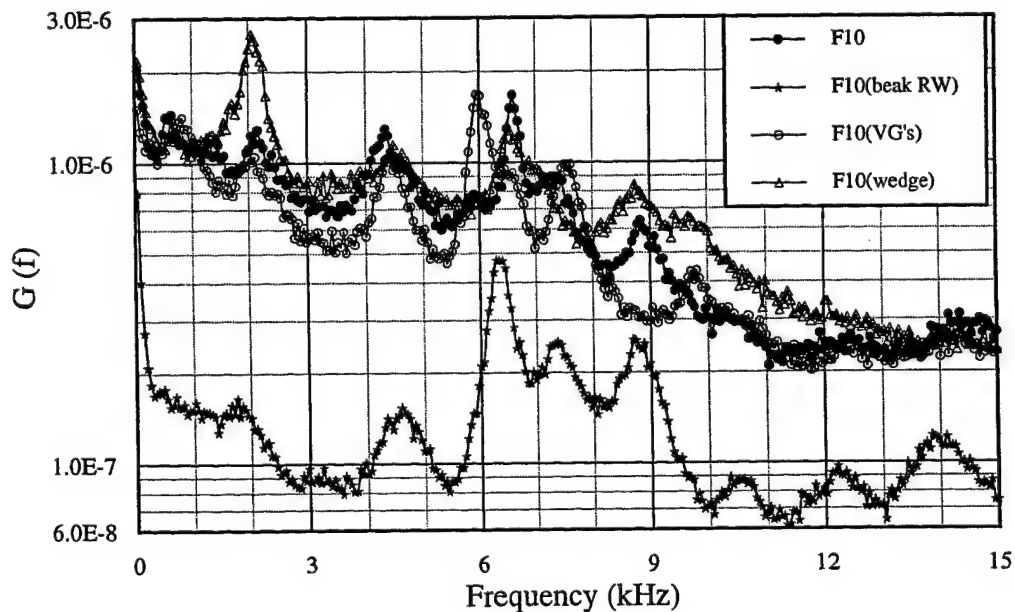


Figure 4.6(b) Power Spectra at Point F10 with BL Spoilers (L/H=3)

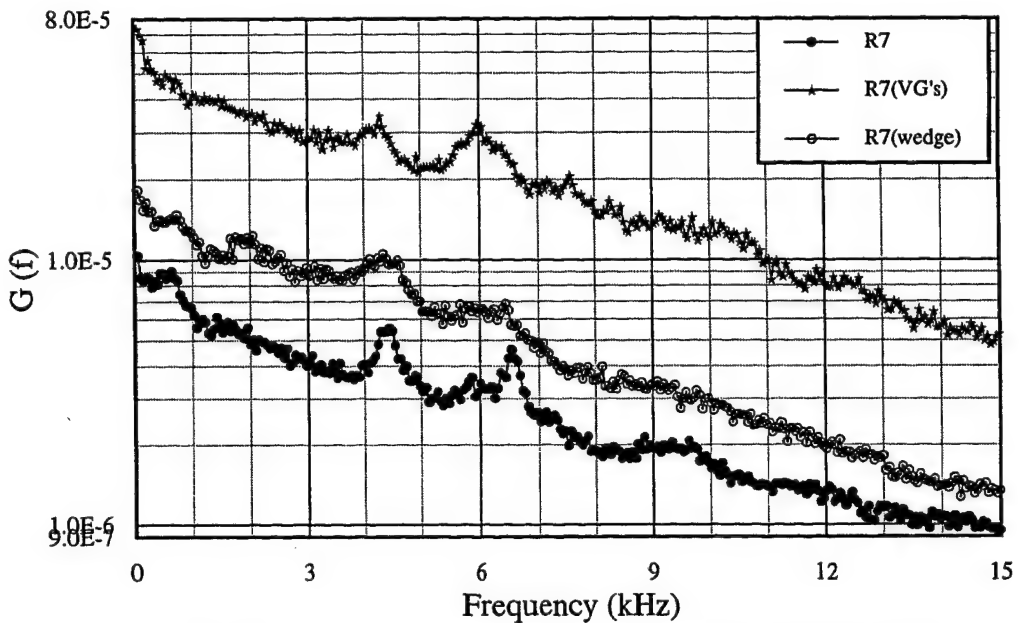


Figure 4.6(c) Power Spectra at Point R7 with BL Spoilers (L/H=3)

For the point F10, the 3rd mode was the strongest for the baseline case. The VG's attenuated the 1st mode by a factor of about 1.1 but left the 2nd & 3rd modes almost unchanged as shown in figure 4.6(b). The wedge weakened the 3rd mode by a factor of about 1.3 but enhanced the 1st mode by a factor of about 2.3. The 2nd mode was almost unchanged. By comparing the strongest modes, the VG's failed with no improvement. The wedge enhanced the 3rd mode of the baseline case by a factor of about 1.7 and the 1st mode became the strongest oscillation mode.

For the point R7, the 2nd mode was the strongest for the baseline case as shown in figure 4.6(c). Both spoilers enhanced all modes. The 2nd mode was enhanced by factors of about 6.3 & 1.9 with the VG's & the wedge respectively. Similarly the 3rd mode was enhanced by factors of about 7.2 & 1.5 respectively.

Therefore the BL spoilers used here were not only ineffective but also enhanced the oscillations. From the earlier discussion, the SL above the cavity was

relative stable due to the compressibility effect. Both spoilers disturbed the incoming BL and made the SL fluttered severely. By checking the power spectra at point R6 (not shown), the impingement shock foot could penetrate as deep as point R6 rather than point R7 in the baseline case. Then more impingement flow poured into the cavity such that stronger oscillations were generated. Since in a very high speed flow the compressible SL is stabilized by the compressibility, it is better not to use any spoiler for preventing more high energy flow from entering the cavity. With both spoilers upstream of the cavity, the changes in incoming BL or SL structure did not largely alter the mode frequencies. This implies that the acoustic wave not the shedding vortex is the main cause of the flow impingement on the RW.

4.4 EFFECTS OF AN INTERNAL OBSTACLE

Inside a cavity, the breathing of the large trailing-edge vortex interacts with the SL impingement. Two obstacles were put on the cavity floor in order to alter the shape of the trailing-edge vortex. One obstacle was the wall base and the other one was the slanted wall #3. In addition, a combination of the wall base and the VG's was tested also. The locations of these obstacles on the cavity floor were described earlier. The test results at points FW1(-0.875), R1(3.0625), & R7(3.875) are shown in figures 4.7(a), (b), & (c). For simplicity, the cavities investigated here are renamed. The case with the wedge put in the middle of the cavity is named cavity A. Cavities B & C correspond to the cases with the wall base put in the middle of the cavity & put 1.5" behind the FW respectively. Cavity D is similar to cavity C but the VG's was attached 1" ahead of the cavity leading edge.

For cases A & C, at point FW1 the strength of the acoustic wave was weakly attenuated at the 2nd (the strongest) mode as shown in figure 4.7(a). For cavity B, all oscillation modes were attenuated significantly. The 1st, 2nd, & 3rd modes were attenuated by factors of about 6.1, 8.1, & 8 respectively. For cavity D with the VG's spoiler, as the SL was disturbed by the spoiler, the 2nd mode was

enhanced by a factor of about 2.6 compared with cavity C. The inefficiency of the spoiler is proven here again.

From figure 4.7(b) at point R1 (the measurement point which was very close to the point F10), the 3rd (the strongest) mode of the baseline case was attenuated to the 2nd (the strongest) mode of cases B & C by factors of about 2.5 & 1.2 respectively. No improvement of case A was obtained by comparing the strongest modes. For case D, the addition of the VG's spoiler still enhanced the oscillations. The oscillations at point R7 which was usually in the region of the flow impingement were shown in figure 4.7(c). By comparing the strongest modes, all cases A, B, & C didn't effectively attenuate the 2nd mode of the baseline case. It is reasonable because the flow near point R7 is dominantly influenced by the SL impingement not by the trailing-edge vortex. This argument was proven by the result of the case D also. Its power spectra level was enhanced a lot such that the 1st mode of the baseline was enhanced by a factor of about 4.6 and shifted to the 2nd mode.

From the above results, the shape and the size of the trailing-edge vortex is important and can affect the oscillation strength. The wall base obstacle is more effective than the wedge obstacle since the volume of the wall base is larger and the size of trailing-edge vortex is smaller. This suggests that not only the acoustic wave but also the trailing-edge vortex can affect the pressure oscillations. The location of the obstacle is also important such that case B is better than case C. It was difficult to measure the pressure distribution on all surfaces in the cavity. The approximate shapes of the vortices inside the cavity could not be obtained for all cases in this study either.

However an interior obstacle would be an effective way to attenuate the oscillations. By checking figures 4.6(a) and 4.7(a), at point FW1 the case B was even better than the beak RW. The defect of this interior obstacle was that less space was available for weapons. In addition, for all methods in this section, all oscillation frequencies shifted to low values. The reason for this is not available since the obstacle made the geometry of the cavity really complicate.

The experimental examinations provide the good data for computational analysis. Especially, the 2-D slanted and 3-D RWs are appropriate models to be simulated since they result in effective and ineffective attenuation.

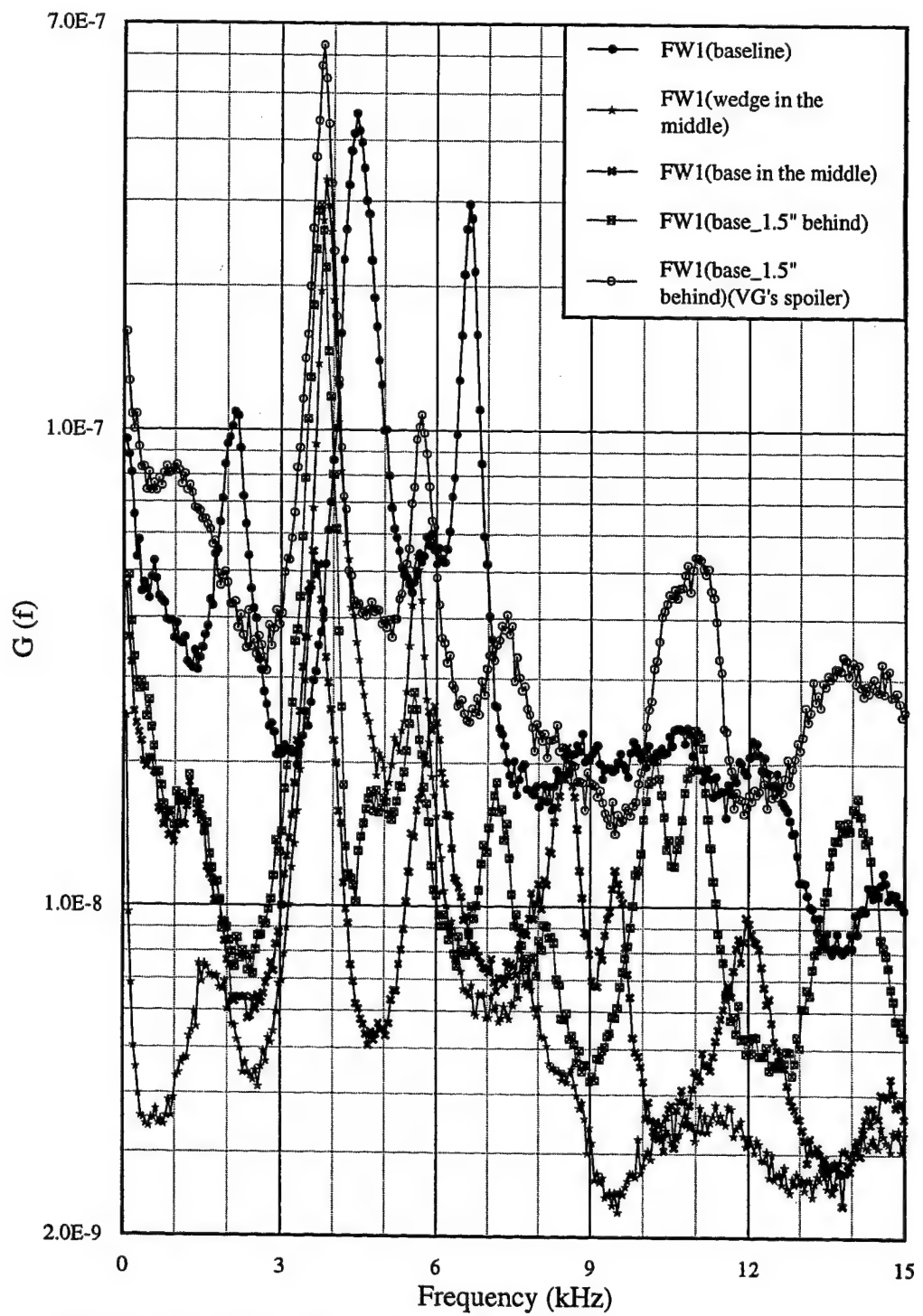


Figure 4.7(a) Power Spectra at Point FW1 with an Obstacle Inside ($L/H=3$)

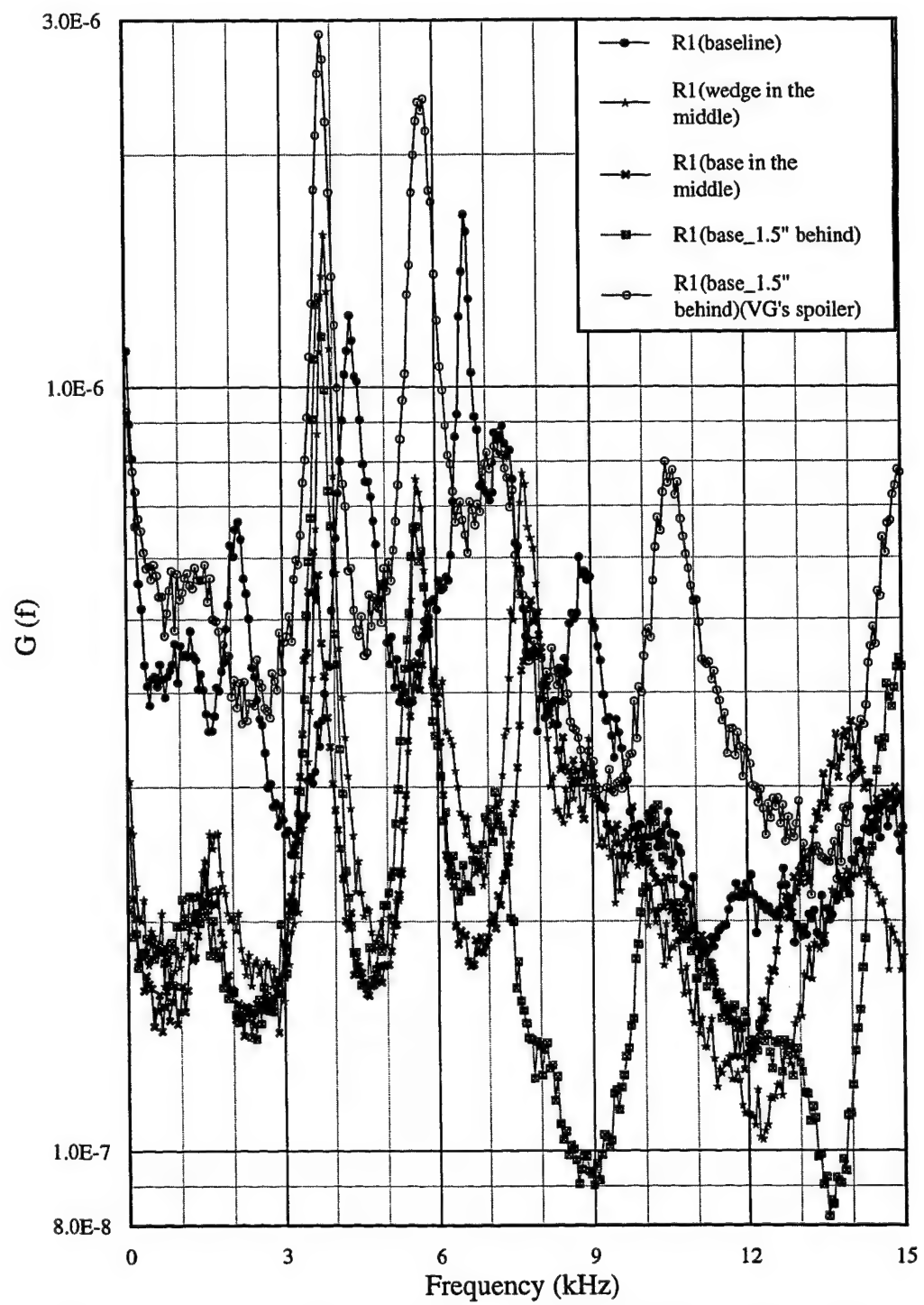


Figure 4.7(b) Power Spectra at Point R1 with an Obstacle Inside ($L/H=3$)

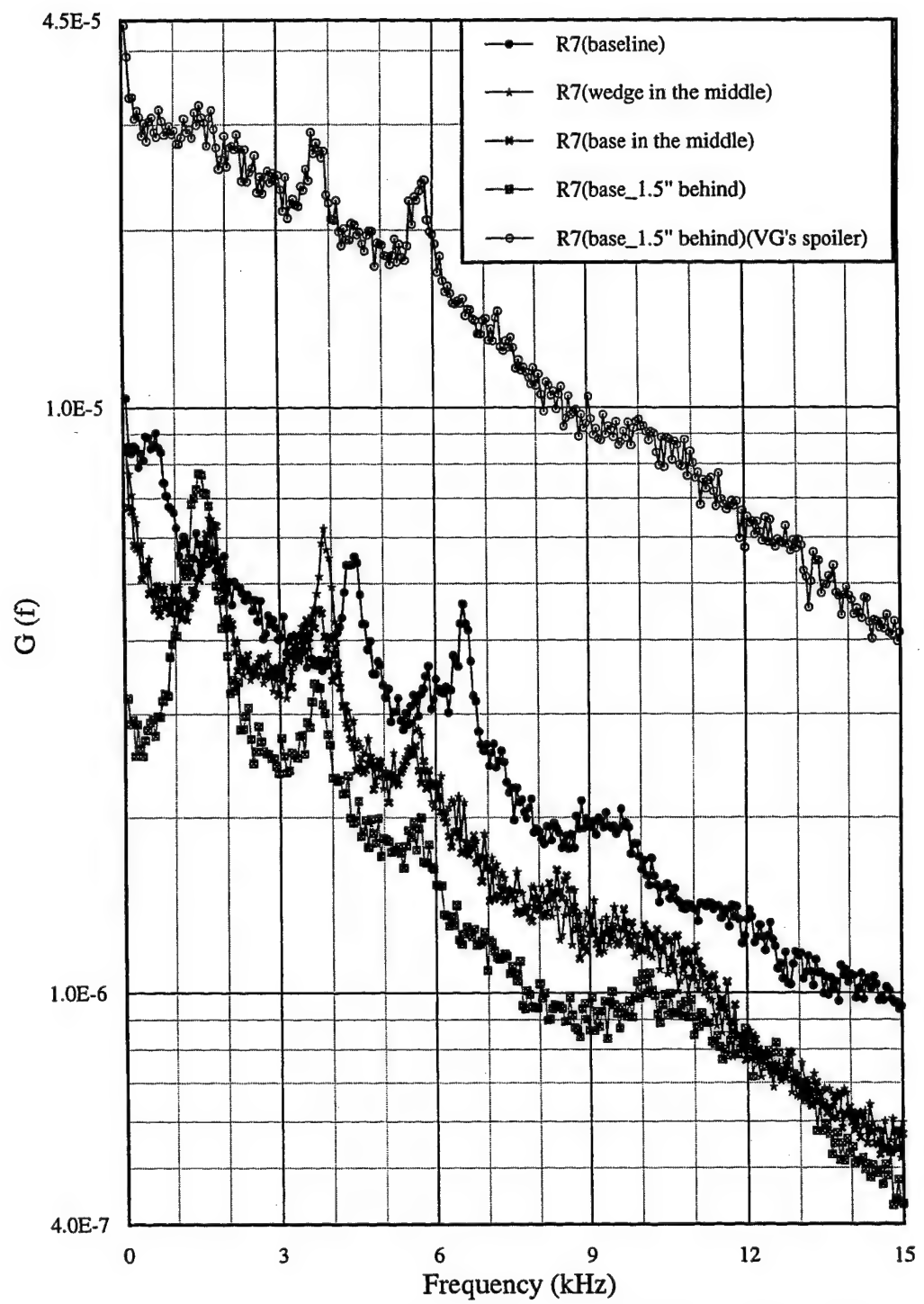


Figure 4.7(c) Power Spectra at Point R7 with an Obstacle Inside ($L/H=3$)

4.5 SCALE-UP DISCUSSION

A critical question is whether experimental results from wind tunnel are applicable to full-scale flight vehicles. For the real flight condition, even at the same Mach number, L , H , and δ/H might be in a different range. Nevertheless pressure oscillations in the cavity will still occur and as seen from the result of chapter 5, L is the dominant parameter which determines the oscillation strength and frequencies. In the real bomb bay, the oscillation frequencies will decrease proportional to the ratio of $L_{\text{bay}}/L_{\text{model}}$ at the same free stream speed and temperature. It has been shown that modified Rossiter's formula predicts oscillation frequencies well for a larger cavity (a 0.2 scale model of the B-1 bomber) examined by Maurer (1973). In general the ratio of δ/H at the flight condition will be different from that of the test model. From the literature review, increasing δ/H results in smoothing out the pressure gradients and decreasing the pressure magnitudes. Therefore, the strength of pressure oscillations decreases. However the frequency modes do not change much as seen in Chapter 5 for the cases $L/H = 3, 4, 5, \& 6$ ($L = 3$ inches). Since the ratio of δ/H in this study is fairly large (≥ 0.7) compared to a typical flight condition (≈ 0.1), the oscillation strength in a bomb bay will probably be much stronger. At different Mach numbers, the stability of SL will change due to the compressibility effect. However, the basic vortex structure does not change and the flow impingement always happens on the RW. All effective control methods are designed to sweep the impingement flow downstream. Therefore, it might be expected that they would also be effective and applicable to the full-scale vehicle.

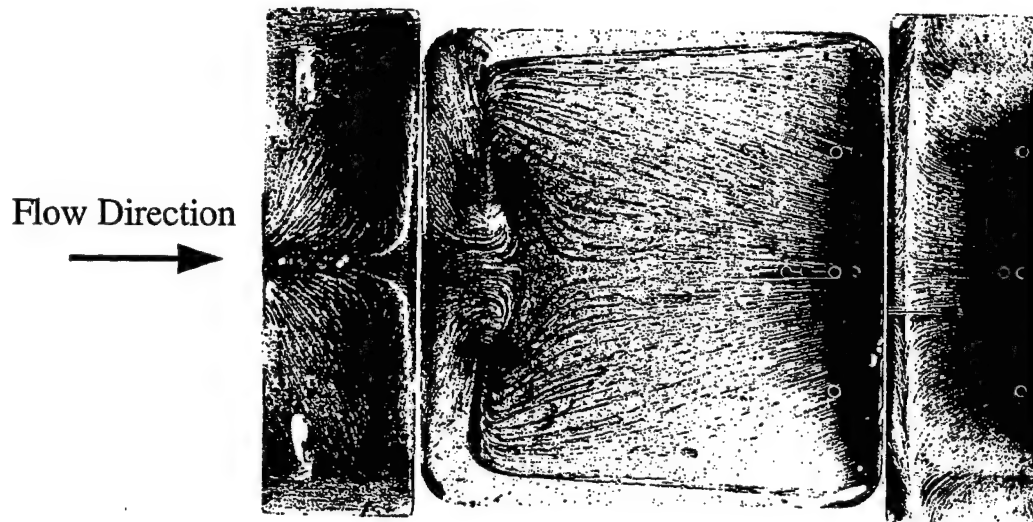
CHAPTER 5 SHOCK/CAVITY INTERACTION

The discussion of the shock/cavity interaction experiment begins with an overview of the flow structure provided by the lampblack surface flow visualization. It is followed by and linked to the detailed surface mean pressure and pressure standard deviation measurements. Then the power spectra are examined in order to draw conclusions about the flow dynamics.

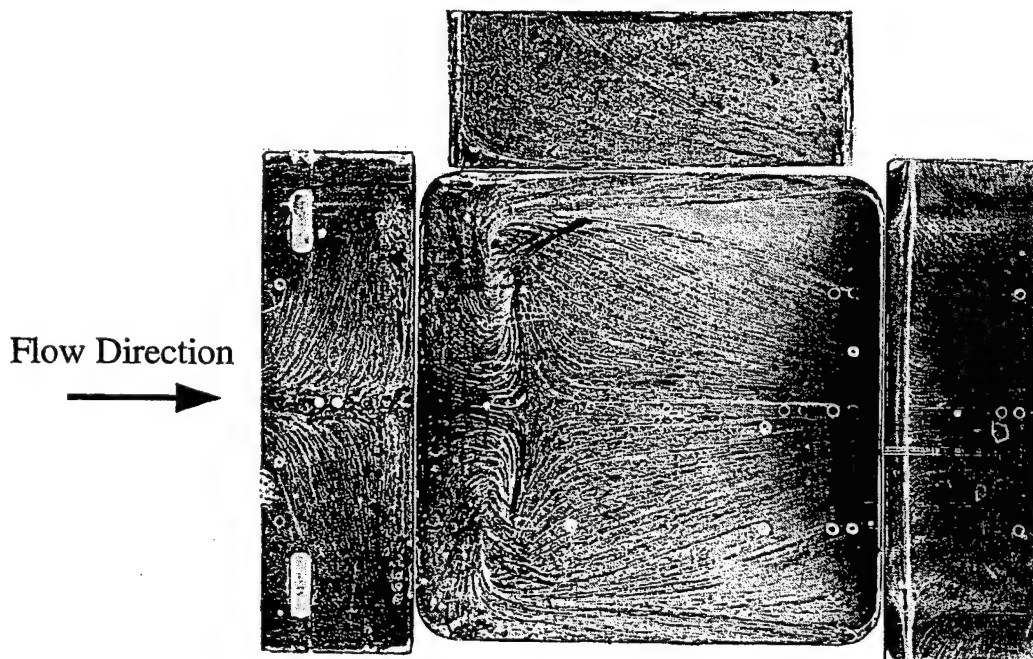
5.1 SURFACE FLOW VISUALIZATION

Surface flow patterns on the cavity front wall, floor and rear wall for the “upstream strong shock impingement” and “downstream strong shock impingement” cases are shown in Figures 5.1(a) and (b) respectively. For the latter case, the flow pattern on one of the cavity side walls is included. An exploded view of the surface flow pattern of the “empty cavity” case (from Perng and Dolling, 1996) with the same L/H ratio as this experiment is shown in Figure 5.2 for comparison.

The flow patterns of these two shock impingement cases show that the flowfield is quite symmetric about the longitudinal centerline of the cavity and that the flow structure with shock impingement is the same as that of the “empty cavity” case. These flowfields all include a large trailing-edge vortex, a small rear corner vortex induced by the trailing-edge vortex and two tornado vortices which form two foci on the front floor (Refer to Figure 5.2 for the locations of these structures). Figure 5.3 is a 3-dimensional sketch of the basic cavity flow structure based on these surface flow visualization results. The shear layer impinges near the upper edge of the rear wall (the impingement line cannot be identified from these flow patterns) and then enters the cavity. Referring to Figure 5.3, part of the impingement flow joins the



(a) The "Upstream Strong Shock Impingement" Case



(b) The "Downstream Strong Shock Impingement" Case

Figure 5.1 Two Surface Flow Patterns of the Strong Shock Impingement Cases

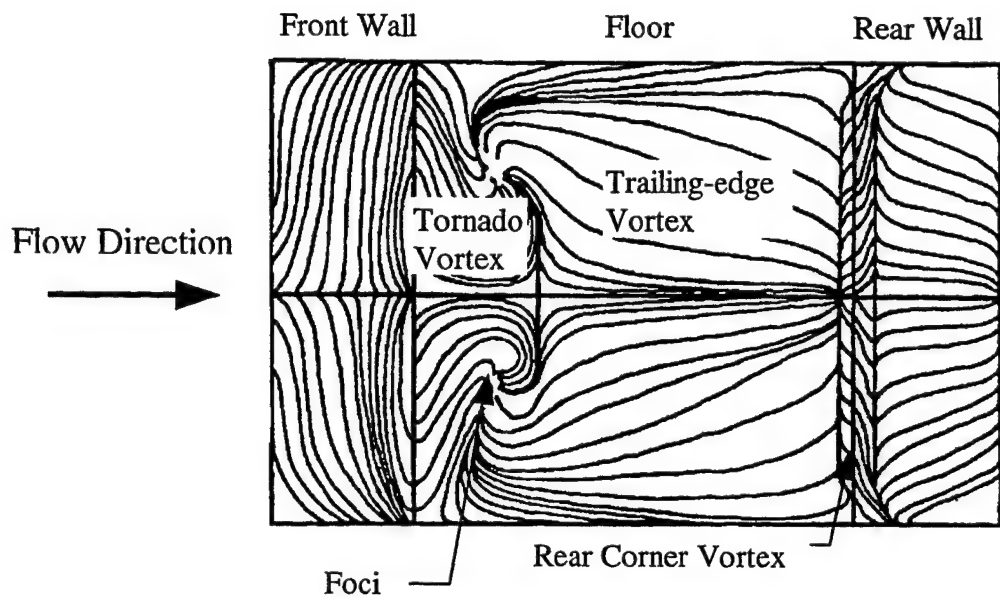


Figure 5.2 Exploded View of the Surface Flow Pattern of the "Empty Cavity" Case
 (Perng and Dolling, 1996)

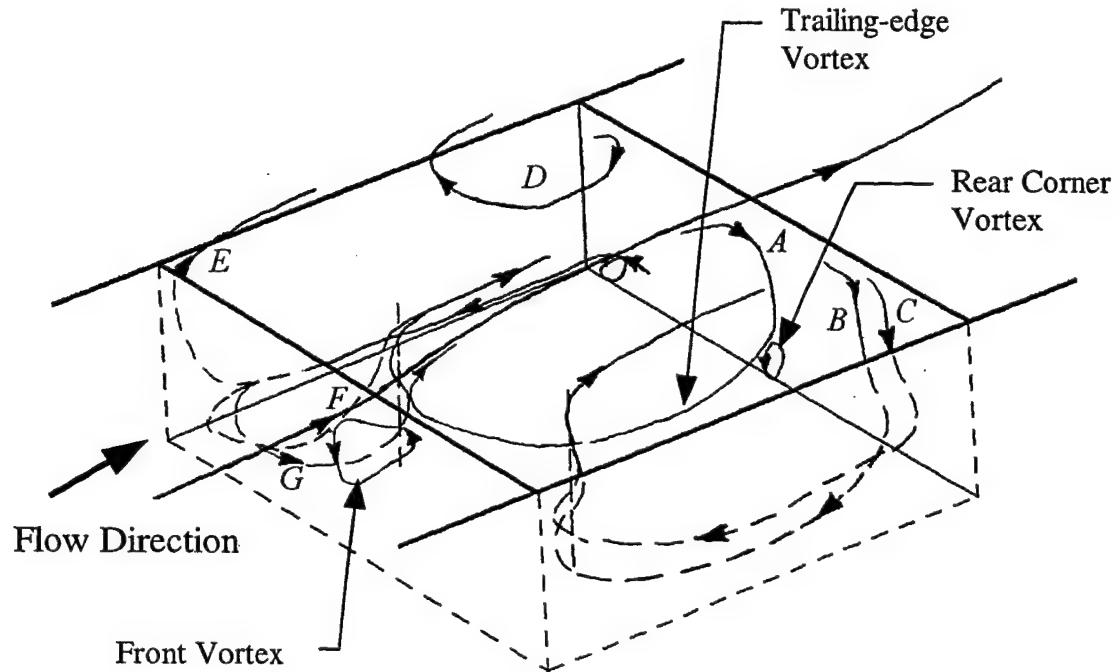
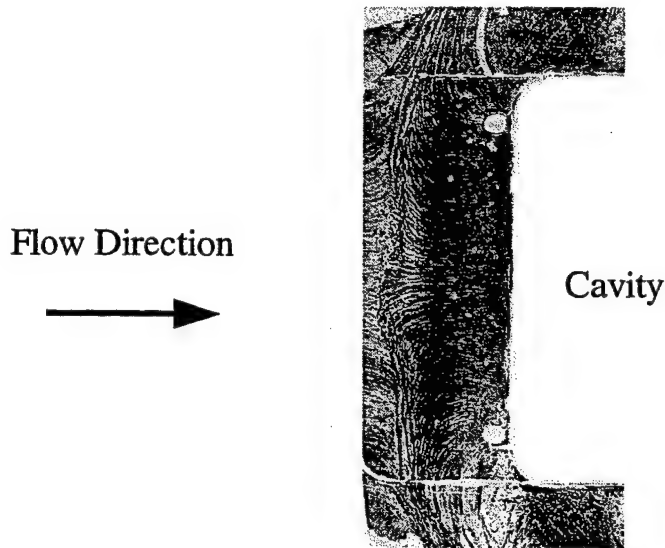


Figure 5.3 3-Dimensional Sketch of the Basic Cavity Flow Structure

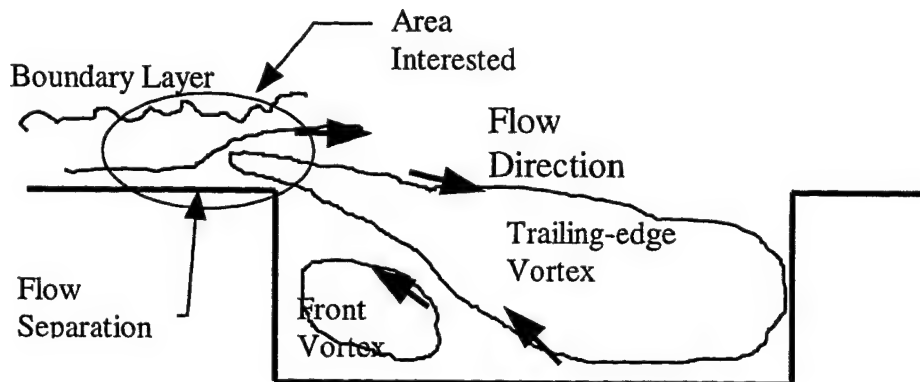
trailing-edge vortex (streamline A) and the two tornado vortices (streamlines B, C), and part of the impingement flow exits the cavity from both side walls soon after entering the cavity (streamline D) as the flow pattern on the side wall shows (Figure 5.1(b)). The rear corner vortex inhales mass from the trailing-edge vortex and expels mass to the front cavity where mean pressures are lower. The expelled mass could exit to the freestream from the front cavity (streamlines E, F) or join the tornado vortices (streamline G).

Compared to the “downstream impingement” case, the two foci of the “upstream impingement” case move upstream a little. This is easily understood since the shock-induced pressure rise facilitates the re-circulation flow from the high pressure region behind the shock wave to the front low pressure region and hence the “upstream shock impingement” case has a larger trailing-edge vortex than the “downstream impingement” case. Note that the separation line on the front wall is cleaner and clearer for the “upstream impingement” case, but is cleaner and clearer on the rear wall for the “downstream impingement” case. This suggests that shock impingement tends to stabilize the local flowfield.

Figure 5.4(a) shows the lampblack taken from the tunnel floor just upstream of the cavity model for the “downstream shock impingement” case. Because the shock impingement facilitates the re-circulation flow inside the cavity, part of the high pressure air inside the cavity is forced to exit the cavity from the front wall and the freestream is pushed away from the cavity at the leading edge. Since it is impossible for the counter-clockwise front vortex to push the freestream back at the leading edge of the cavity and to leave a flow pattern like this one on the tunnel floor, the trailing-edge vortex must reach the front wall frequently in the mean cavity flow structure. A 2-dimensional sketch of the flow structure for the flow separation just upstream of the cavity is shown in Figure 5.4(b).



(a) Surface Flow Pattern on the Tunnel Floor Just Upstream of the Cavity



(b) The Cavity Flow Structure Causes the Flow Separation

Figure 5.4 Surface Flow Pattern on the Tunnel Floor and the Cavity Flow Structure Just Upstream of the Cavity Model of the "Downstream Shock Impingement" Case

5.2 MEAN PRESSURE AND PRESSURE STANDARD DEVIATION

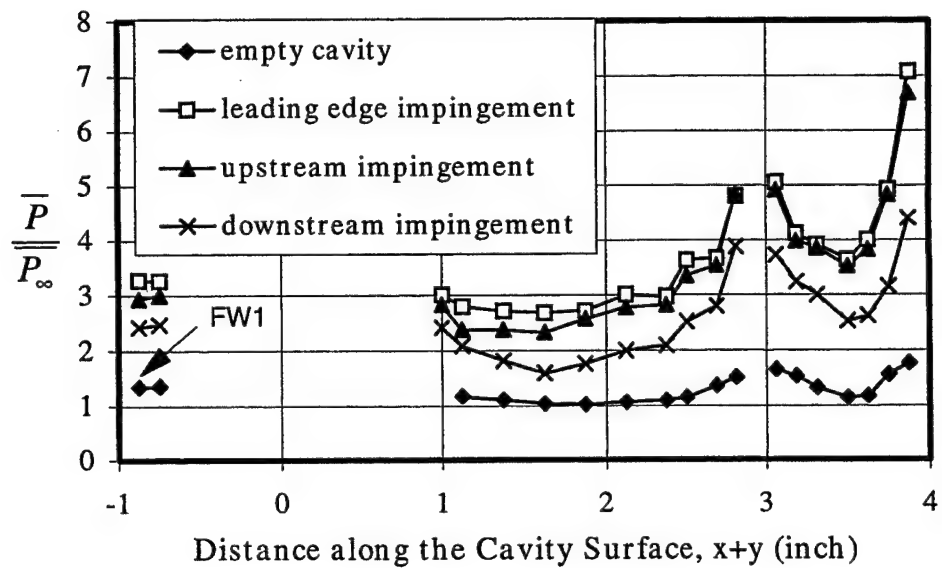
First of all, the symmetry of the flowfield is checked. For the "empty cavity" case, the ratios of the mean pressures of an off-centerline port to its corresponding centerline port at $x/L=0.94$ on the cavity floor are 0.94 and 0.90 for the off-centerline

port at $z/W=-0.25$ and $+0.25$ respectively. Similarly, the dimensionless σ_p (which is an indicator of the amplitude of the mean pressure fluctuations) ratios are 0.97 and 0.93 respectively for the above two off-centerline ports. The mean pressure and σ_p ratios combined with the surface flow pattern show that the mean flowfield is approximately symmetric about the longitudinal centerline.

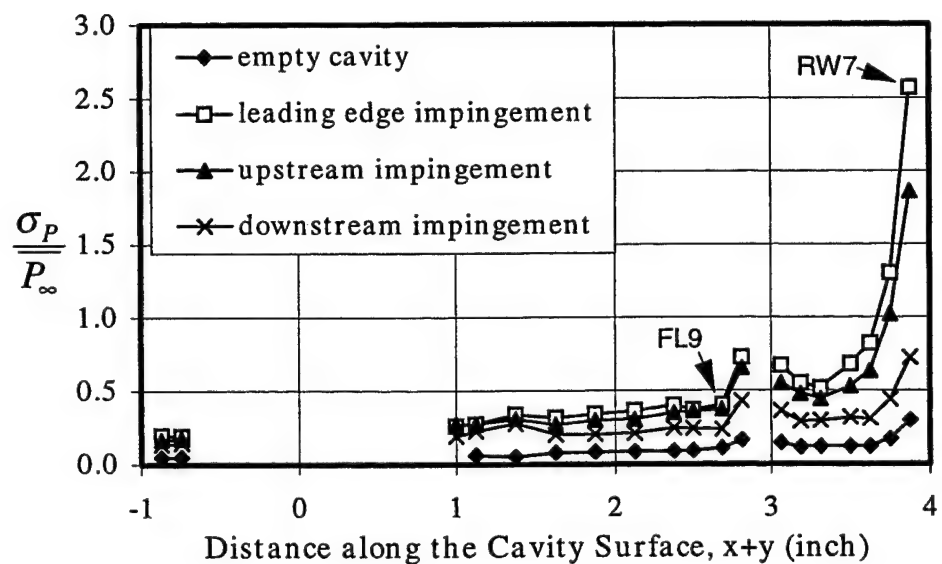
The mean pressure and σ_p distributions on the cavity surface for the strong shock impingement cases are discussed in this section with emphasis on measurements along the longitudinal centerline of the cavity. The "empty cavity" data are also included for comparison. In all of the following mean pressure and σ_p distribution figures, the abscissa ("Distance along the Cavity Surface") is the distance of the transducer port to the bottom of the front wall when the cavity surfaces are unfolded. The 'y' coordinates are negative for the ports on the front wall and are positive for those on the rear wall. Thus, the upper edges of the front wall and the rear wall are at -1 and +4, respectively, on the abscissa.

Figures 5.5(a) and (b) show the mean pressure and σ_p distributions respectively on the cavity surface for the shock impingement cases. The mean pressure and σ_p distributions for the shock impingement cases are quite similar to those of the "empty cavity" case in shape. This observation suggests that shock impingement does not change the mean cavity flow structure. Note that these distributions show no information about the impingement position, i.e., there is no sudden jump in the mean pressure and σ_p distributions. Since the shock wave cannot penetrate into the cavity, the only way to affect the mean pressure and σ_p distributions is through the shear layer impingement flow entering the cavity from the rear wall.

An interesting feature in Figure 5.5 is that the mean pressure and σ_p curves shift upwards as the shock impingement position moves upstream. The reason might be that the shear layer is deflected by the shock wave and hence the mean impingement position is deepened on the rear wall as the shock impingement position



(a) Mean Pressure Distribution



(b) Pressure Standard Deviation

Figure 5.5 Mean Pressure and Pressure Standard Deviation Distributions on the Cavity Surface of the Shock Impingement Cases

moves upstream. The consequence is that the entrainment mass flow rate is increased as the shock impingement position moves upstream. However, the influence of the shear layer deflection is alleviated by the blockage of the trailing-edge vortex in its path as the shock impingement position moves upstream. This might be why the difference between the "upstream impingement" and the "leading edge impingement" cases in Figure 5.5 is smaller than that between the "upstream impingement" and the "downstream impingement" cases. The trends of the σ_p curves mentioned above conflict with the experimental results of Sakamoto et. al. (1995) which showed that the pressure fluctuations of the "downstream impingement" case were smaller than those of the "empty cavity" case. The reason for the difference is not known.

For the "upstream impingement" case, the maximum mean pressure and the maximum σ_p values are $6.7 \bar{P}_\infty$ and $1.9 \bar{P}_\infty$ respectively. They all occur at the top edge of the rear wall as for the other cases. Such high mean pressure and σ_p values show that shock impingement is very detrimental to cavity flow. From Figure 5.5(a), the lowest mean pressures on the rear wall occur at the same point for all cases. Thus shock impingement does not change the mean vertical position of the trailing-edge vortex compared to the "empty cavity" case. The scale of the trailing-edge vortex, however, is not identifiable from this figure because no transducer port is available on the front cavity floor. Unlike the "empty cavity" case, the lowest mean pressure values on the cavity surface for all "shock impingement" cases are much higher than \bar{P}_∞ (Figure 5.5(a)). The high \bar{P}/\bar{P}_∞ ratio near the leading edge of the cavity explains partly why back flow occurs on the tunnel floor upstream of the cavity as seen in the lampblack flow pattern (Figure 5.4(a)).

If the mean pressure of the shear layer is assumed to be uniform in the 'y' direction and to be approximately equal to that at port FW1 (0.125 inch below the leading edge on the front wall) at the leading edge, then the angle which the shear layer forms with the tunnel floor at the leading edge can be estimated using charts for

inviscid oblique shocks. Define the angle as the “shear layer angle”. For the “upstream impingement”, “downstream impingement” and “empty cavity” cases, the shear layer angles are 9.8° , 7.8° and 2.5° respectively. Figure 5.6 shows the pressure signals of the “upstream shock impingement” case taken at FW1 in an interval of 2 ms.

The mean pressure value at this port of this case is around $2.9 \bar{P}_\infty$. Since the shear layer deflects up and down with the pressure signals at the leading edge, the shear layer angle indicates the average shear layer position relative to the cavity. A larger shear layer angle results from a higher pressure field which is caused by more serious shear layer impingement events. The deflection of the shear layer can be regarded as the mechanism via which the cavity flow regulates the pressure environment inside it. Note that for the shock impingement cases, the shear layer is deflected downwards downstream of the leading edge by expansion waves.

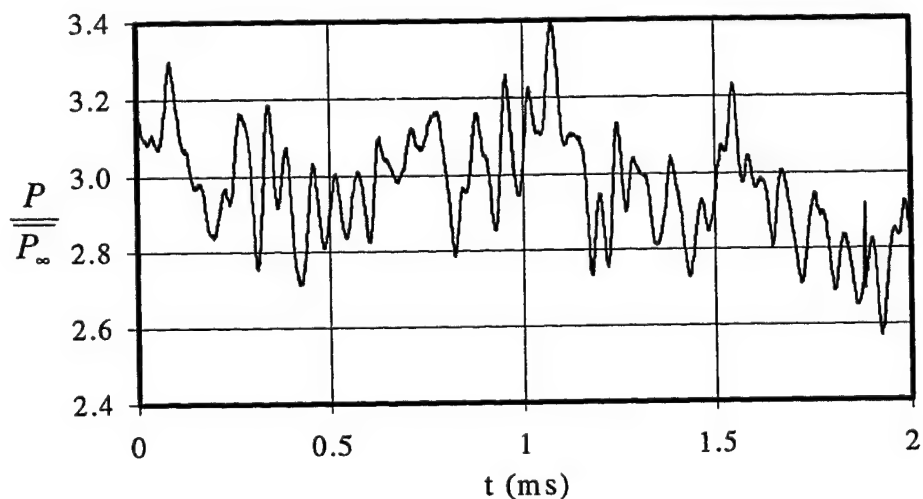


Figure 5.6 Pressure Signals Taken at FW1 of the
“Upstream Shock Impingement” Case

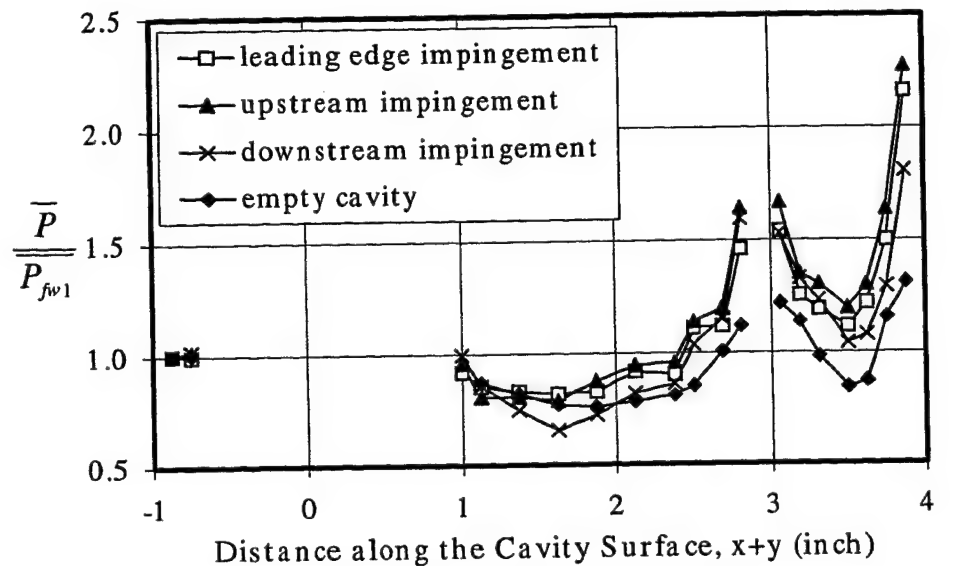
From Figure 5.5(b), the value of σ_P drops rapidly from RW7 to FL9 for all cases. This indicates that the intense pressure fluctuations connected to the shear layer

impingement event dissipate quickly after the impingement flow enters the cavity. On the front wall the σ_p values of the shock impingement cases remain as high as 3 times that of the “empty cavity” case (the σ_p value at FW1 of the “empty cavity” case is about $0.05 \bar{P}_\infty$), although these values are much lower than those at the top of the rear wall.

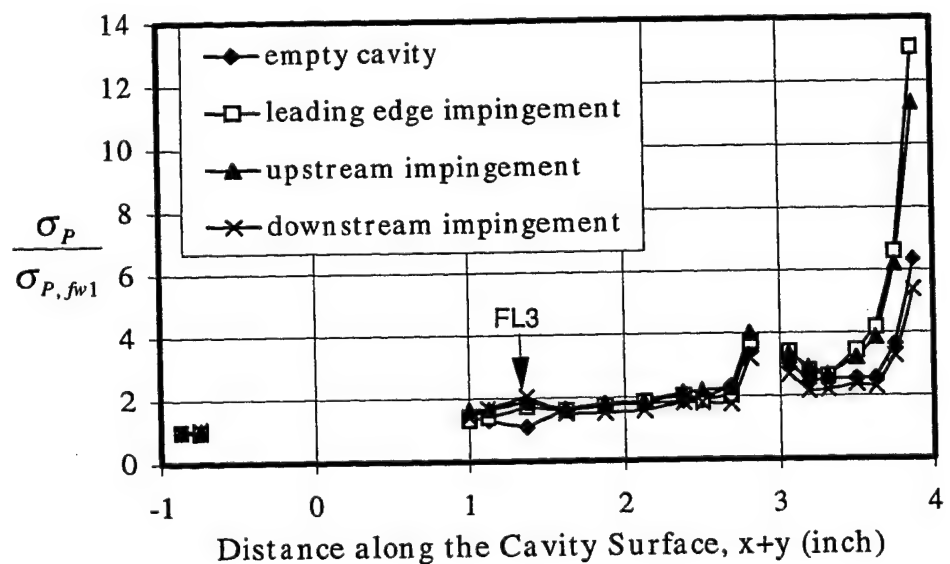
Figures 5.7(a) and (b) show the normalized mean pressure and σ_p distributions of the curves in Figure 5.5. The normalization was performed using the mean pressure or σ_p value at FW1 for each case. For the normalized mean pressure curves, the main difference between the shock impingement cases and the “empty cavity” case is that the normalized mean pressure values on the rear wall and the rear floor are higher for all shock impingement cases. For the normalized σ_p distributions, all curves, including the “empty cavity” case, collapse well on the floor with the maximum difference being 8~24% (except the point FL3). The difference is defined as (larger value - smaller value)/larger value. This is not surprising since the pressure rise induced by the shock wave cannot affect the σ_p values on the floor through the large depth of the cavity, and the intense flow fluctuations incorporated with the shear layer impingement dissipate quickly after the entrainment of the shear layer.

5.3 MODE FREQUENCIES

According to Perng’s analysis (1996) using conditional sampling, the oscillatory frequency of the bow shock at the top of the rear wall is in between the 1st and 2nd modes of the pressure oscillations inside the cavity. Thus the motion of the bow shock does not “lock on” to the mode frequencies of the cavity flow. Generally, the power spectral density plots for ports at the upper edge of the rear wall have the



(a) Normalized Mean Pressure Distribution



(b) Normalized Pressure Standard Deviation

Figure 5.7 Normalized Mean Pressure and Pressure Standard Deviation
Distributions of the Shock Impingement Cases

least obvious peak frequencies compared to those anywhere else since the background noise levels generated by the unsteady bow shock system are high compared to the peak levels of the mode frequencies. Power spectra obtained at FW1 for the strong shock impingement cases are shown in Figure 5.8. The vertical axis, $G(f)$, in Figure 5.8 is the power spectral density function with a dimension of $(\text{psia})^2/\text{Hz}$. Comparison with the power spectra from the undisturbed incoming boundary layer shows that the high level energy in the low frequency range ($< 1 \text{ kHz}$) in Figure 5.8 is due to the thick incoming turbulent boundary layer. From this figure it is clear that shifting the shock impingement position upstream results in higher power spectral density for a very wide frequency interval especially for the high frequency band. The result is consistent with Figure 5.5(b) which indicates that moving the shock impingement position upstream results in higher σ_p values.

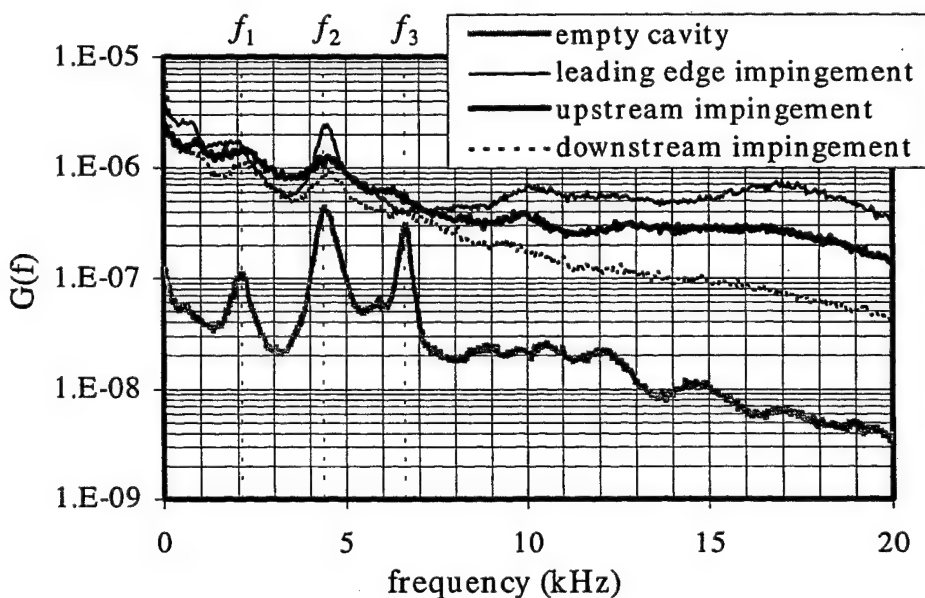


Figure 5.8 Power Spectra Obtained at FW1 of the Shock Impingement Cases

Because the amplitude of the background noise is increased, the mode frequencies are less obvious for the shock impingement cases compared to the "empty

cavity" case. Table 5.1 lists the mode frequencies for the shock impingement cases and for the "empty cavity" case. Mode frequencies calculated from the modified Rossiter's formula (Equation 2.1) are also included for comparison. In calculating the mode frequencies, the cavity flow model proposed by Heller and Bliss was adopted. In this model the cause of the impingement event on the rear wall is the reflected acoustic wave from the front wall rather than the shedding vortices. This renders α in Equation 2.1 equal to zero. The value of k_c which is now the ratio of "the adiabatic temperature sound speed in the cavity" to "the freestream speed"

$(=\sqrt{1+\frac{1}{2}\beta(\gamma-1)M^2/M})$ is equal to 0.468 for this experiment. Note that in the low

frequency range there are no peak frequencies induced by the shock impingement as described in the experiment of Sakamoto et al. (1995).

Table 5.1 Mode Frequencies (kHz) at FW1 of the Strong Shock Impingement Cases

Case	f_1	f_2	f_3
Empty cavity	2.15	4.39	6.64
Leading edge impingement	2.05	4.49	-
Upstream impingement	2.15	4.49	6.30
Downstream impingement	2.29	4.49	-
Modified Rossiter's formula (Calculated)	2.35	4.70	7.05

Note: '-' means that the mode frequency is not obvious.

The most important observation from Figure 5.8 and Table 5.1 is that shock impingement has little effect on the mode frequencies. The shock wave only enhances the power spectral level. Thus, the feedback mechanism of the self-sustaining oscillations inside the cavity and the mode frequencies of the flowfield are not changed by the shock impingement.

5.4 CHANGING SHOCK STRENGTH

As mentioned earlier in the experimental program, some of the shock/cavity interaction experiments were repeated using a weaker shock wave. The reason for using a different shock strength in this experiment is to find out whether the mean pressure and σ_p values at each port scale simply on the strength of the impingement shock. For this part of the experiment the results show that the mean pressure and σ_p distributions and the power spectra of the weak shock impingement cases resemble those of the strong shock impingement cases. The weak shock impingement cases have smaller mean pressures, pressure standard deviations and power spectral levels at each port but the same mode frequencies compared to the strong shock impingement cases as expected. Table 5.2(a) lists the mean pressure ratios of the "strong shock" case to the "weak shock" case at all ports. The σ_p ratios of these two cases are listed in Table 5.2(b). If the mean pressure distributions can be scaled by the shock strength, the ratios in Table 5.2(a) should be about the same. The same concept applies to the σ_p distributions and Table 5.2(b). As shown in these Tables, the ratios are not the same. Thus, \bar{P} and σ_p cannot be scaled by the relative shock strength.

Figure 5.9 shows the σ_p / \bar{P} (the pressure standard deviation to the local mean pressure value) curves for the shock impingement cases. This ratio is similar to the definition of the local turbulent intensity. The ratios σ_p / \bar{P} fall into a narrow zone (0.03-0.13) for all ports except those on the upper rear wall where the impingement flow raises the flow fluctuations significantly.

5.5 SUMMARIZING REMARKS

Shock impingement has detrimental effects on cavity flow. The mean pressure and σ_p values and the power spectral levels on the cavity surface are increased significantly by the shock impingement. The shock impingement position affects these

values too. An upstream impingement position results in more serious pressure environment in the cavity. The resemblance of the lampblack flow patterns, the mean pressure and σ_p distributions between the shock impingement cases and the "empty cavity" case suggests that they have nearly the same mean cavity flow structure. Also the oscillation mode frequencies between these cases are nearly invariant. Therefore, it might be anticipated that the control methods developed to attenuate pressure fluctuations in empty cavities will be effective for cavities with shock impingement.

Table 5.2 Ratios of $\bar{P}_{\text{strong shock}} / \bar{P}_{\text{weak shock}}$ and $\sigma_{p, \text{strong shock}} / \sigma_{p, \text{weak shock}}$ at each port

(a) Ratios of $\bar{P}_{\text{strong shock}} / \bar{P}_{\text{weak shock}}$

Port	Upstream impingement	Downstream impingement
FW1	1.32	1.33
FW2	1.33	1.33
FL1	1.34	1.20
FL2	1.21	1.36
FL3	1.27	1.14
FL4	1.34	1.07
FL5	1.41	1.13
FL6	1.35	1.20
FL7	1.35	1.29
FL8	1.36	1.27
FL9	1.41	1.43
FL10	1.47	1.45
RW1	1.50	1.42
RW2	1.43	1.48
RW3	1.40	1.36
RW4	1.47	1.37
RW5	1.51	1.32
RW6	1.61	1.39
RW7	1.75	1.39

(b) Ratios of $\sigma_{p, \text{strong shock}} / \sigma_{p, \text{weak shock}}$

Port	Upstream impingement	Downstream impingement
FW1	1.49	1.58
FW2	1.61	1.77
FL1	1.79	1.81
FL2	1.55	1.83
FL3	1.46	1.62
FL4	1.46	1.49
FL5	1.54	1.42
FL6	1.46	1.44
FL7	1.48	1.47
FL8	1.62	1.49
FL9	1.66	1.51
FL10	1.72	1.55
RW1	1.65	1.56
RW2	1.74	1.53
RW3	1.66	1.56
RW4	1.59	1.38
RW5	1.83	1.27
RW6	2.31	1.50
RW7	2.39	1.35

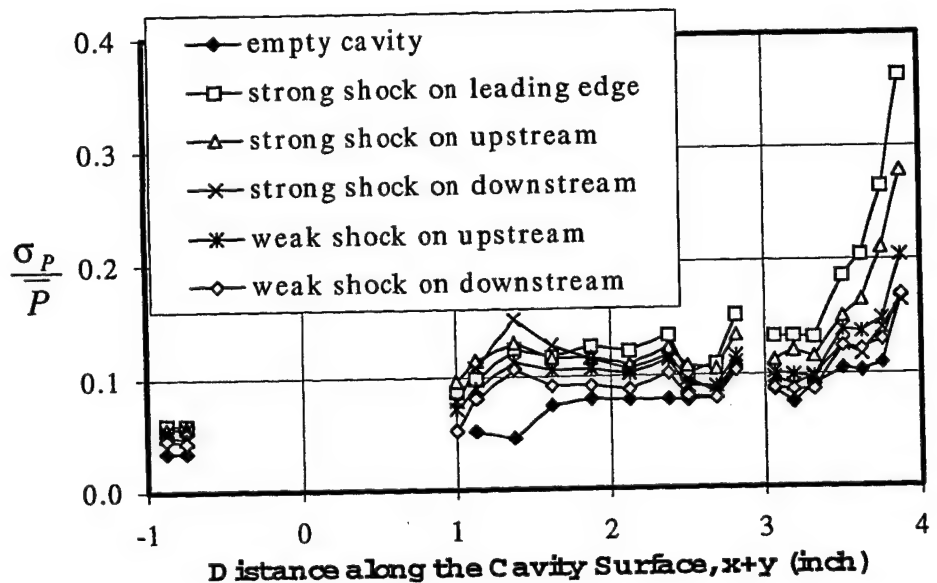


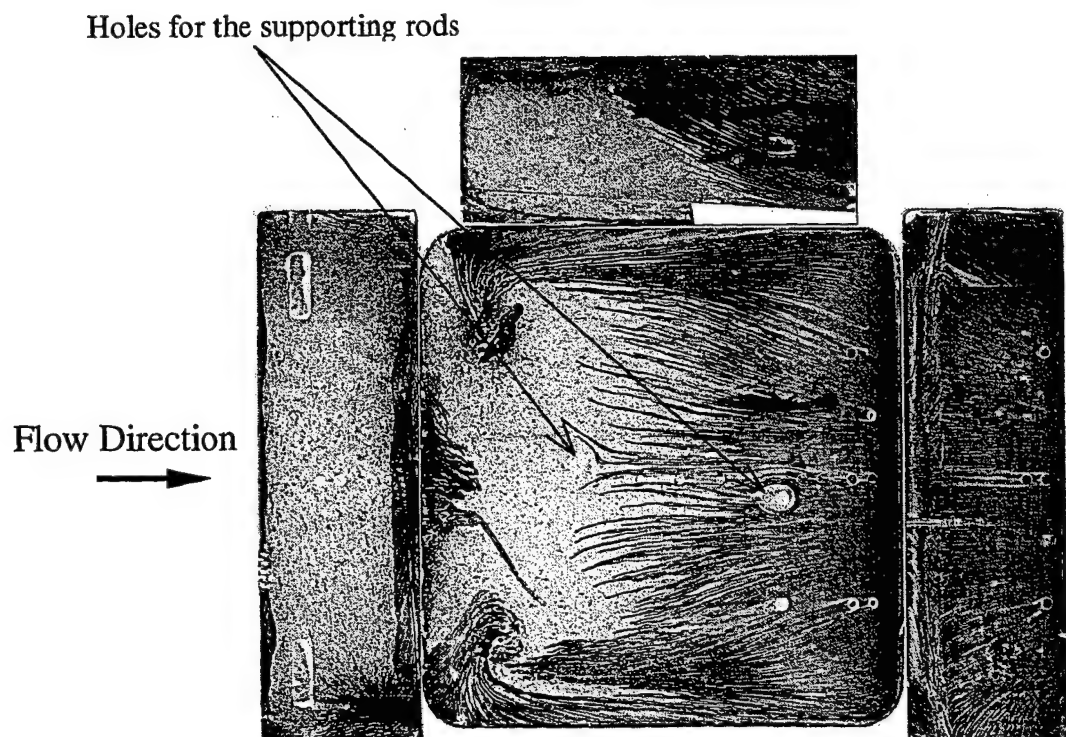
Figure 5.9 σ_P/\bar{P} Distributions on the Cavity Surface of the Shock Impingement Cases

CHAPTER 6 SINGLE STORE/CAVITY INTERACTION

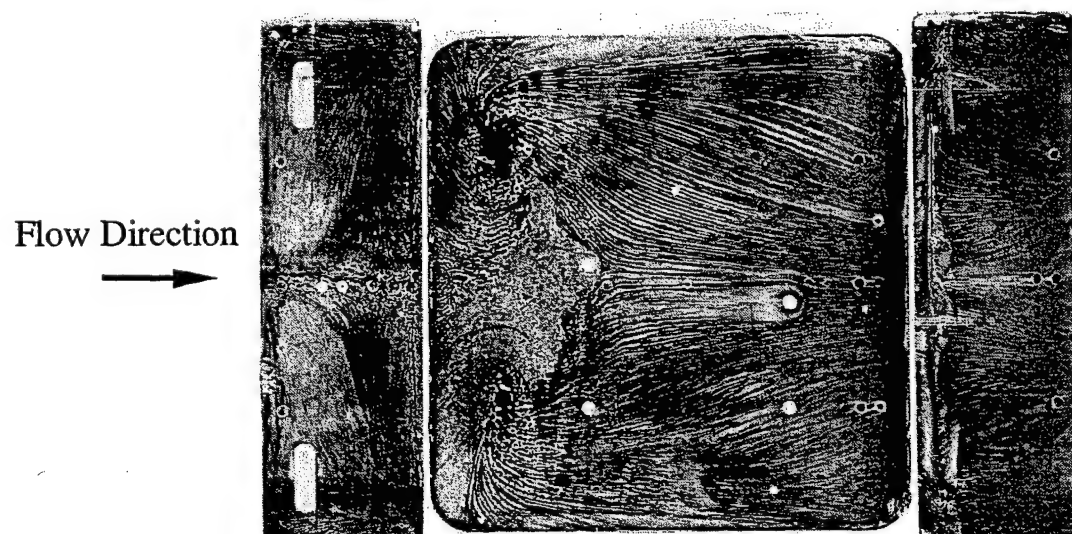
6.1 SURFACE FLOW VISUALIZATION

As mentioned in Chapter 2, the store was positioned on the cavity centerline in the single store/cavity interaction experiment. Thus when referring to the cases in this experiment, the words "single" and "on the cavity centerline" will be eliminated for conciseness. For example, "the store at $H/3$ case" stands for "the single store on the cavity centerline at $y=H/3$ case". For the "store in the shear layer" case, the large drag brought the store downstream a little (estimated to be 0.12 inch from the drag and the property of the material of the supports), but no vibration was observed during the runs. Since we are interested in the general effects of the store position (especially the y position) on cavity flow, the position shift of the store in the x direction during the runs is neglected. Surface flow patterns on the front wall, the floor and the rear wall of the "store at $H/3$ ", "store at $2H/3$ " and "store in the shear layer" cases are shown in Figures 6.1(a), (b) and (c) respectively. Due to difficulty in lifting the lampblack pattern off the side walls, only part of the flow pattern on the side wall is shown for the "store at $H/3$ " and "store in the shear layer" cases.

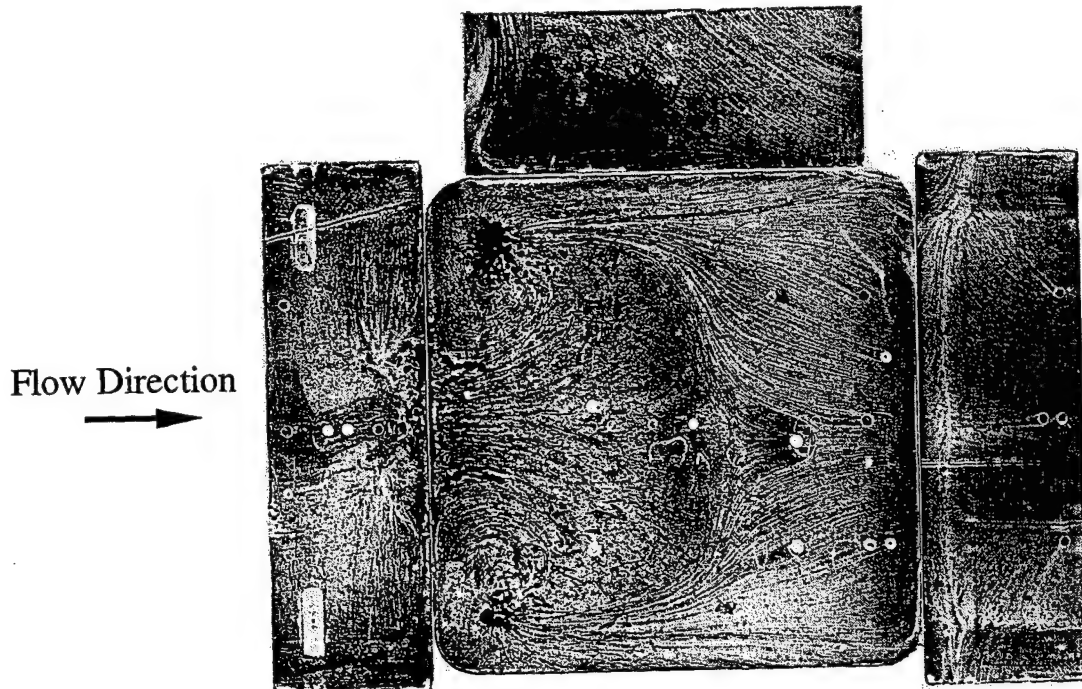
These flow patterns show good symmetry about the longitudinal centerline of the cavity. The two small rods used to support the store (see the two small white solid



(a) The "Store at H/3" Case



(b) The "Store at 2H/3" Case



(c) The "Store in the Shear Layer" Case

Figure 6.1 Surface Flow Patterns of the Single Store
on the Cavity Centerline Cases

circles in the surface flow patterns at coordinates $[1, 0, -0.114]$ inch and $[2.25, 0, 0.114]$ inch) near the centerline have certain influence on the flowfield. However, their influence is localized and small compared to the overall flowfield as shown in Figure 6.1. Surprisingly, even with the blockage of a store, the surface flow patterns of these three cases are still very similar to that of the "empty cavity" case. The changes are mainly in the positions of the two foci on the floor and the size (and probably the strength) of the trailing-edge vortex. This suggests that the basic mean flow structure is not changed by the store. There are several other noteworthy observations about these flow patterns which are discussed below.

The foci of the "store in the shear layer" case are located further upstream and further off-centerline than the other cases. Since the central and most of the rear part

of the cavity are directly affected by the store-induced bow shock for this case, the pressure difference forces flow to go upstream and outwards and thus moves the two foci upstream and outwards to lower pressure regions. The pressure difference also causes the two tornado vortices to grow bigger. As shown in Figure 6.1(c), the flow pattern of these two tornado vortices on the floor grows very large and occupies almost 50% of the cavity floor. Thus, the trailing-edge vortex is pushed downstream and is the smallest of all cases studied.

The separation line on the rear wall is more obscure for the cases with a store “inside” the cavity than for the cases with shock impingement (referring back to Figure 6.2), suggesting that the cavity flowfield is less stable with a store inside it. Also with a store inside the cavity, the surface flow pattern has a blank area on the front cavity floor. Repeated runs using different lampblack composition produced the same result. This suggests that the local shear stress is not high enough to drive the lampblack forward and hence the trailing-edge vortex inside the cavity is weakened by the store. Based on the size of the blank area on the floor, the relative strength of the trailing-edge vortex for the two cases with a store inside the cavity is: the “store at $H/3$ ” case < the “store at $2H/3$ ” case. However, even with the blockage of the store, the size of the trailing-edge vortex is still very large and it occupies most of the cavity.

The streak lines on the side wall and on the right and left quarter portions of the rear wall indicate that part of the impingement flow moves laterally and escapes from the cavity along both side walls. The escape is driven by the pressure difference between the inside of the cavity and the freestream. This phenomenon is more obvious for the “store in the shear layer” case since the streak lines on the rear wall have larger curvature for this case. The expulsion of mass occurs for the rear corner vortex too as those streak lines of the rear corner vortex on both sides of the rear wall which connect to some of the streak lines on the side walls show. It is inferred that the rear corner vortex extracts mass from the trailing-edge vortex and expels part of its mass

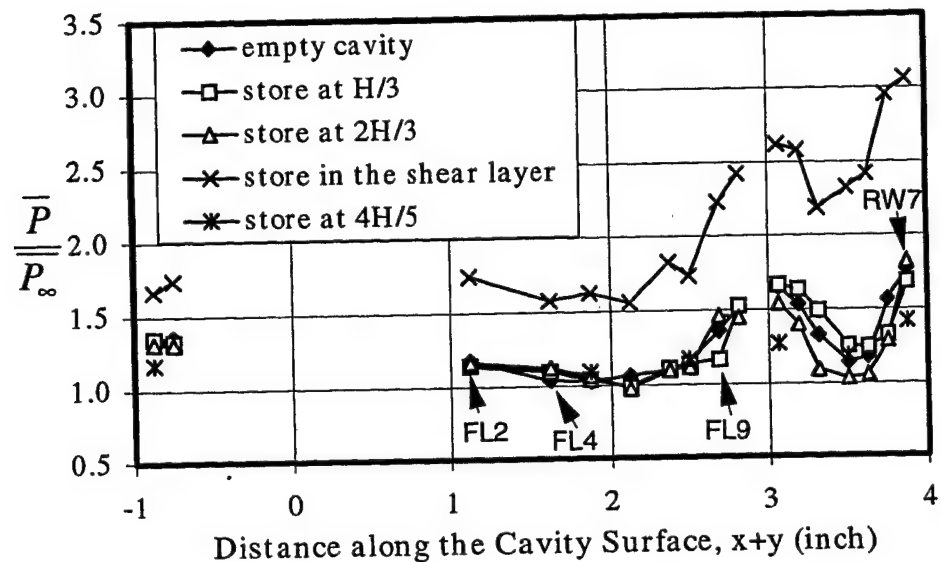
into the freestream. The same inference applies to the shock impingement cases (referring back to Figure 6.2).

For the “store at $2H/3$ ” case, the streak lines near the centerline on the rear wall curve towards the centerline. This is because the low-pressure region behind the store base causes the high pressure impingement flow to expand towards it. Thus, the shielding of the store comes into play to affect the cavity flowfield. The flow pattern on the side wall of the “store at $H/3$ ” case has traces of spanwise vortices generated by the side wall whereas the flow pattern of the “store in the shear layer” case does not. It appears that for the latter case, the pressure inside the cavity is much higher than that of the freestream, so the pressure environment does not allow the spanwise vortices to roll into the cavity. On the contrary, the spanwise vortices roll into the cavity for the former case because of a nearly equal pressure environment between the inside of the cavity and the freestream.

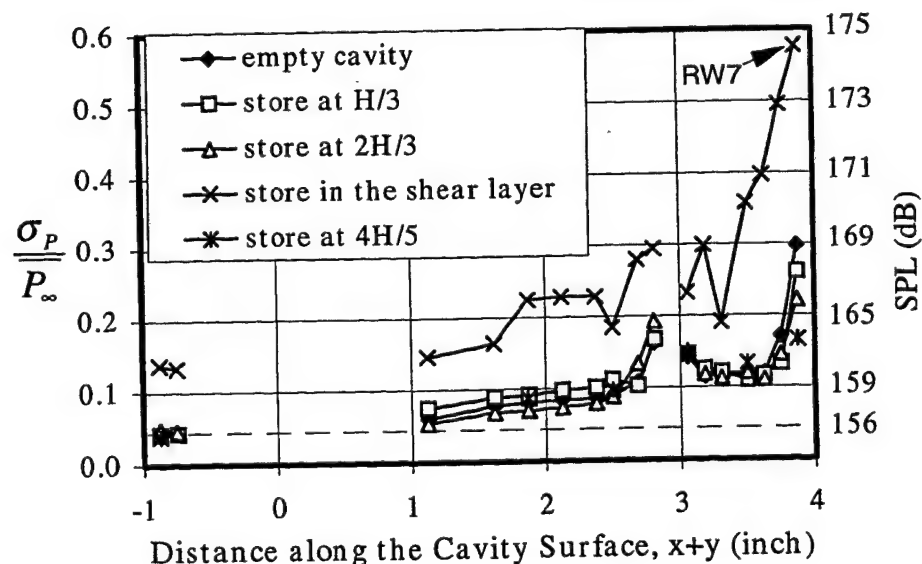
6.2 MEAN PRESSURE AND PRESSURE STANDARD DEVIATION

Like the shock impingement cases, the mean pressure and pressure standard deviation distributions with store-release are discussed with an emphasis on the measurements made along the cavity centerline only. The symmetry of the flowfield is checked quantitatively. For the “store at $H/3$ ” case, the ratios of the pressures of an off-centerline port to its corresponding centerline port at $x/L=0.542$ on the cavity floor are 0.95 and 0.93 for the off-centerline port at $z/W=-0.25$ and $+0.25$ respectively. Similarly, the σ_p ratios are 0.94 and 0.84 for the above two ports respectively. These ratios combined with the surface flow patterns show that the flowfield is approximately symmetric about the longitudinal centerline.

The effects of the store position on the mean pressure and σ_p distributions are shown in Figures 6.2(a) and (b) respectively. The equivalent sound pressure level



(a) Mean Pressure Distribution



(b) Pressure Standard Deviation

Figure 6.2 Mean Pressure and Pressure Standard Deviation Distributions of the Single Store/Cavity Interaction Cases

scale for the pressure standard deviations at an altitude of 40,000 ft is shown on the right vertical axis of Figure 6.2(b) for reference. The equivalent sound pressure levels

are calculated from the formula: $SPL = 20 \log_{10} \left(\frac{\sigma_p}{0.00002 \text{ N/m}^2} \right)$. They are obtained

by neglecting any scaling issues (such as the relative scales of the boundary layer

thickness) and by assuming that $\left(\frac{\sigma_p}{P_\infty} \right)_{\text{at } 40,000'} = \left(\frac{\sigma_p}{P_\infty} \right)_{\text{current experiment}}$. For clarity, the

store position for each case is shown in Figures 6.3(a), (b) and (d). An additional case, the “store at 4H/5” case (Figure 6.3(c)), was tested besides those three planned positions. This case is discussed separately at the end of this chapter.

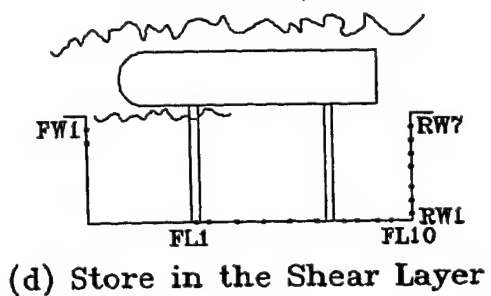
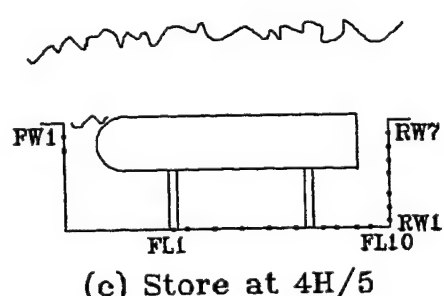
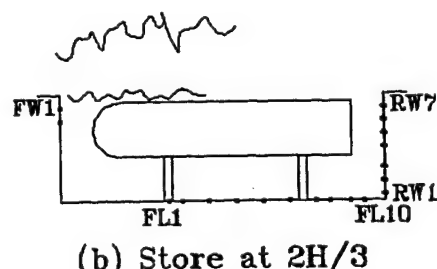
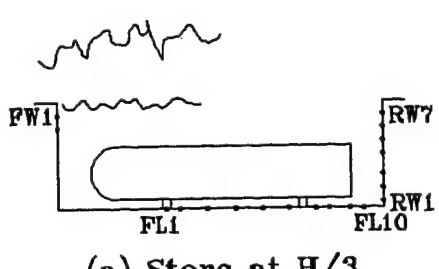


Figure 6.3 Store Positions Tested in the Single Store/Cavity Interaction Experiment

The curves in Figure 6.2 suggest that the hardest pressure environment during store-release occurs when the store is in or above the shear layer and induces a bow shock impinging on the cavity. The maximum mean pressure and σ_p values are as high as $3.07 \bar{P}_\infty$ and $0.58 \bar{P}_\infty$ respectively for this experiment. For all cases studied, the maximum mean pressure and σ_p values all occur at the upper edge of the rear wall. The most notable point is that the curves in Figure 6.2 are all similar to those of the "empty cavity" case. It appears that even with the blockage of a store, the basic mean cavity flowfield remains unchanged compared to the empty cavity flowfield.

The mean pressure and σ_p values on the cavity surface for the cases with a store "inside" the cavity are quite close to those for the "empty cavity" case except for the values on the rear wall. The discrepancy may result from different entrainment mass flow rates for different cases. Thus the presence of a store "inside" the cavity does relatively little to the mean flowfield of the empty cavity. However, there are several quantitative changes to the vortex scale. The changes of the mean flowfield for all cases are discussed below.

Position of the Trailing-edge Vortex. The minimum mean pressures on the floor and rear wall suggest the mean position of the trailing-edge vortex. Figure 6.2(a) shows that the mean vertical position of the trailing-edge vortex moves upwards (to RW5) and downwards (to RW3) with a store deep in the cavity (the "store at $H/3$ " case) and a store in the shear layer respectively compared to the "empty cavity" case (For the "empty cavity" case, it occurs at port RW4.). Thus the trailing-edge vortex is forced upwards with the deep blockage of a store and is forced downwards with a store in the shear layer since the store deflects part of the incoming shear layer deep down into the cavity. For the "store at $2H/3$ " case, the store does not affect the mean vertical position of the trailing-edge vortex. On the floor, the bottom of the trailing-edge vortex moves downstream for all cases with a store in the cavity (from FL5 for the "empty cavity" case to FL6) as indicated by the position of the lowest mean

pressure on the floor. The flat low-pressure region on the middle of the floor for the “store in the shear layer” case is a result of the tornado vortices as inferred from cross-examining the mean pressure curve and the corresponding surface flow pattern (Figure 6.1(c)). Its σ_p curve on the floor has a flat plateau near the boundary of the tornado vortices and the trailing-edge vortex.

Size of the Trailing-edge Vortex. There is no definitive way to determine the length of the trailing-edge vortex from the mean pressure distribution curve. The height of the trailing-edge vortex, however, can be roughly estimated from the “openness” of the mean pressure distribution curve on the rear wall. The more open it is, the higher the trailing-edge vortex is. From Figure 6.2(a), the height of the trailing-edge vortex is: the “store at $2H/3$ ” case > the “empty cavity” case > the “store at $H/3$ ” case > the “store in the shear layer” case. For the “store at $2H/3$ ” case, the upper surface of the store is nearly flush with the tunnel floor, so the low pressure region right behind the store base facilitates the turning of the shear layer at the upper edge of the rear wall that enlarges the height of the trailing-edge vortex. For the “store at $H/3$ ” and the “store in the shear layer” cases, the height of the trailing-edge vortex decreases compared to the “empty cavity” case. For the former, it is due to the deep blockage of the store as inferred from the flattened mean pressure curve at the rear corner; for the latter, it is due to the deep impingement of the shear layer that results from the deflection of the shear layer by the store, and the growth of the rear corner vortex (as inferred from the nearly flattened mean pressure curve at the upper and lower edge of the rear wall respectively for both reasonings. See *Others* below for additional evidence of the growth of the rear corner vortex).

Shielding of the Store. The store can alter the mean pressure and σ_p distributions via its “shielding” effect. For example, for the “store at $H/3$ ” case the lower store surface is just about 0.08 inch above the floor. Thus, the mean pressure and σ_p distributions under it (from FL2 to FL9) are nearly uniform as shown in Figure

6.2. Another example is that, the σ_p value at RW7 of the “store at 2H/3” case is the lowest of all cases since RW7 is shielded by the store base in this case.

Shear Layer Angle. The shear layer angle is 2.5° for the “store at H/3” and the “store at 2H/3” cases and this angle is the same value as that of the “empty cavity” case. For the “store in the shear layer” case, the shear layer angle is 4.2° .

Others. In Figure 6.2(b), the σ_p values on the rear wall drop at the rear corner (from RW2 to RW1) for the “store in the shear layer” case. Since vortex motion causes large variations in the pressure signal, a large decrease of the standard deviation here is indicative of a very strong rear corner vortex. Because the small rear corner vortex is affiliated with the large trailing-edge vortex, the trailing-edge vortex for this case is the strongest of all (inferred from its strongest rear corner vortex of all cases). Combining this inference with the results from the surface flow visualization about the vortex strength, the strength of the trailing-edge vortex is in the following order: the “store in the shear layer” case > the “store at 2H/3” case > the “store at H/3” case.

6.3 MODE FREQUENCIES

The power spectra obtained at FW1 on the front wall of the single store/cavity interaction cases are shown in Figure 6.4. From this figure with a store in the shear layer, the power spectral levels of the mode frequencies as well as the background noises are increased due to the impingement of the store-induced bow shock as anticipated. The power spectra for the “empty cavity” case are nearly the same as those for the cases with a store “inside” the cavity except that for the “store at 2H/3” case, the 4th and 5th mode frequencies become obvious and the power spectral level of the 3rd mode is amplified a lot. The reason for this higher concentration of energy in the 3rd mode and the more noticeable 4th and 5th mode frequencies is not known. One guess for this high concentration of energy is that the store-cavity configuration of this

case enhances the 3rd mode frequency due to the intensification of the vertical oscillations (For the current experiment, L/H equals to 3. Thus, the 1st vertical oscillation mode frequency should be approximately equal to the 3rd longitudinal mode frequency if acoustic waves are the major cause of the pressure fluctuations inside the cavity.). Figure 6.4 suggests that when the store is about to touch the shear layer during store-release, the pressure fluctuation level could be as severe as that when the store induces a bow shock impinging on the cavity. This information cannot be deduced from the σ_p plot alone since the σ_p plot does not provide energy distribution information. However, the maximum power spectral level of the pressure fluctuations inside the cavity during store-release still occurs in the "store in the shear layer" case at port RW7. It is about 3.2 times the maximum power spectral level of the modes of the empty cavity flow. For the "store at 2H/3" case, the maximum power spectral level inside the cavity occurs at FL10 instead of RW7. Thus the re-compression of the impingement flow at the rear corner and hence the vertical oscillations become important in this case.

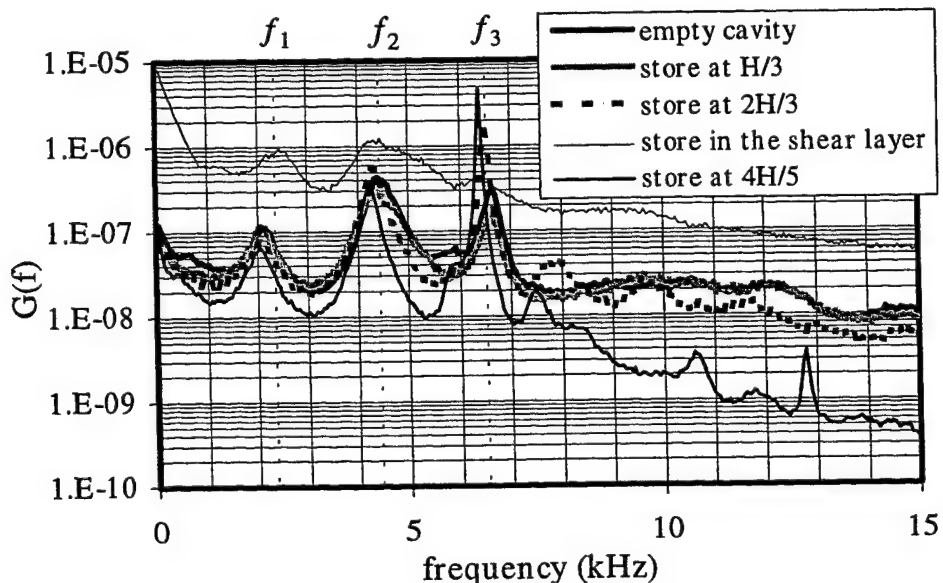


Figure 6.4 Power Spectra at FW1 of the Single Stcre/Cavity Interaction Cases

Table 6.1 lists the values of the mode frequencies for all store positions examined. The calculated frequencies from the modified Rossiter's formula using $\alpha=0$ and $k_c=0.468$ are also included. It is seen that the modified Rossiter's formula does not provide a satisfactory prediction for the 4th mode. Due to the blockage of the store, the mode frequencies of the cases with a store "inside" the cavity are a little lower than those of the "empty cavity" case. The 1st and 2nd mode frequencies of the "store in the shear layer" case are a little higher compared to those of the "empty cavity" case. The reason for this is not known. The most important point to be drawn from Figure 6.4 and Table 6.1 is that the presence of the store changes the mode frequencies very little. Different store position mainly results in enhanced or depressed power spectral levels of some modes. Thus, the feedback mechanism and the mode frequencies of the cavity flowfield are not changed by the store.

Table 6.1 Mode Frequencies (kHz) at FW1 of the Single Store/Cavity Interaction Cases

Case	f_1	f_2	f_3	f_4
Modified Rossiter's formula (Caculated)	2.35	4.70	7.05	9.40
Empty cavity	2.15	4.39	6.64	-
Store at H/3	2.05	4.39	6.59	-
Store at 2H/3	2.05	4.30	6.49	7.76
Store in the shear layer	2.44	4.44	6.40	-

Note: '-' means that the mode frequency is not obvious.

6.4 MORE DISCUSSION ON STORE POSITION

The current experiment shows that the pressure environment inside the cavity does not necessarily benefit from the presence of a store inside the cavity. Referring to

Figure 6.4, the power spectral level of the dominant mode of the “store at $H/3$ ” case is lower, though not by much, than that of the “empty cavity” case, but that is not the case for the “store at $2H/3$ ” case. Due to this discrepancy, a supplemental experiment with a different store position at $y=4H/5$ was tested to explore further the effect of the shear layer/store interaction on cavity flow. Pressure signals were taken at a few ports only. The store position was chosen such that only a small volume of the store was immersed in the shear layer while the store axis was still inside the cavity. It was anticipated that the store would deflect part of the shear layer upward, thus reducing the mass flow rate into the cavity without inducing a bow shock impinging on the cavity. The pressure environment would benefit from the reduction of the impingement mass flow rate.

Referring to Figure 6.2, all measured mean pressure and σ_p values for the “store at $4H/5$ ” case indicate that the store does not induce a bow shock impinging on the cavity since they are the same order as those of the “empty cavity” case. The mean pressure distribution on the rear wall tends to flatten out for this case suggesting that the trailing-edge vortex is weakened (no large vortex motion). Also the mean pressure values at FW1, RW1 and RW7 and the σ_p value at RW7 are all lower than those of the other cases. The power spectra (Figure 6.4) show that the energy of the background noise of this case is the smallest of all. The above observations are evidence of a lower mass flow rate into the cavity, although the shielding of the store is partly responsible for lower mean pressure and σ_p values at RW7 (Refer to Figure 6.3(c) for the relative position of the store base to port RW7. The store base shields RW7 from direct impingement of the shear layer in this case.). It seems that the “store at $4H/5$ ” case has the most favorable pressure environment among all cases. However, the power spectral level of the 3rd mode frequency for this case is still enhanced significantly. Thus, a possible energy source for the enhanced 3rd mode is from the vertical fluctuations. Also note from Figure 6.4 that there emerges the 2nd vertical oscillation

mode at 12.8 kHz for this case. These results suggest that vertical oscillation mode becomes more and more important when the store is at the opening of the cavity.

6.5 SUMMARIZING REMARKS

The mean pressure, σ_p and power spectra on the cavity surface show that these quantities are not changed much by the presence of a store "inside" the cavity. However, when the store is at the opening of the cavity, the power spectral level of the 3rd mode frequency is increased significantly which has detrimental effects on cavity flow. Such a result cannot be seen from the σ_p plot alone. With a store outside the cavity and inducing a bow shock impinging on the cavity, the pressure environment, which deteriorates in the same manner as the shock impingement cases mentioned in chapter 4, is the worst during store-release.

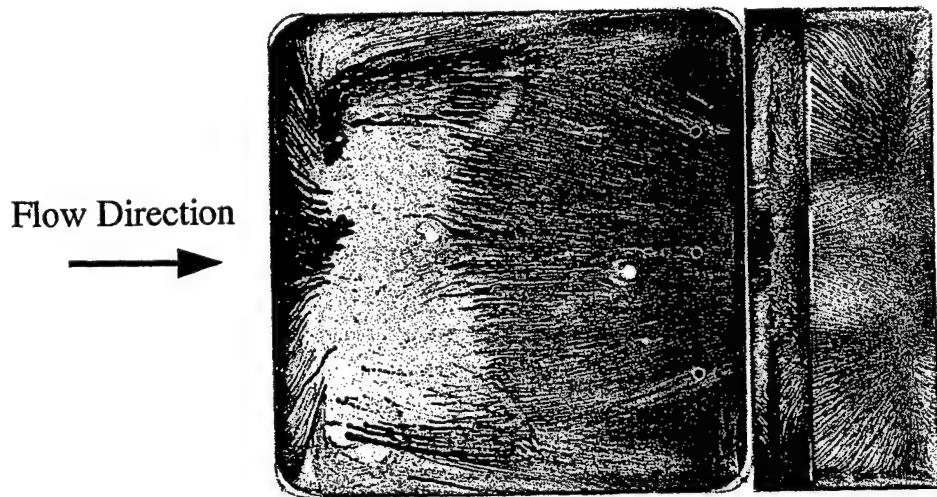
The most important conclusion from the single store/cavity interaction experiment is that the mean empty cavity flowfield and its oscillation mode frequencies are not changed by the presence of a store as inferred from the similarity of the lampblack flow patterns, the mean pressure and σ_p distributions and the mode frequencies on the cavity surface. Thus, the control methods developed to attenuate pressure fluctuations in empty cavities should be applicable for cavities with store-release.

CHAPTER 7 PASSIVE CONTROL TECHNIQUES FOR PERTURBED FLOW CASES

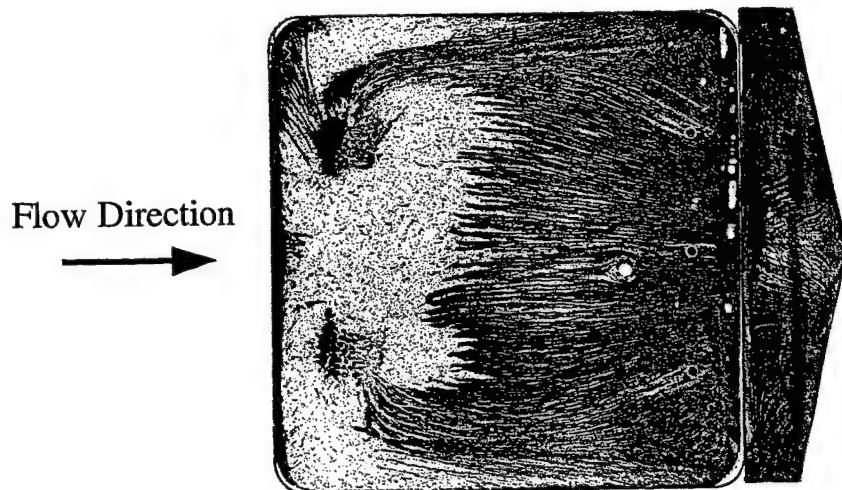
7.1 SURFACE FLOW VISUALIZATION

The surface flow patterns on the floor and rear wall of the cavity of the cases with a store at $2H/3$ and the slanted or "beak" rear wall are shown in Figures 6.1(a) and (b) respectively. For the latter case because of the complicated geometry of the "beak" rear wall, only the lower part (near the rear corner) of the flow pattern on the rear wall is shown.

The similarity of these flow patterns to that of the vertical rear wall case suggests that the essential mean cavity flow structure is not changed by these two rear walls. Since these flow patterns have a larger blank area on the front cavity floor compared to the vertical rear wall case, it can be inferred that the strength of the trailing-edge vortex is weakened by the slanted and "beak" rear walls. The weaker vortex structure results from less mass entering the cavity because the shear layer impingement angle on the rear wall is changed by the slanted



(a) The "Store at 2H/3 with the Slanted Rear Wall" Case



(b) The "Store at 2H/3 with the Beak Rear Wall" Case

Figure 7.1 Surface Flow Patterns of the Cases with a Store at 2H/3 and Passive Control Rear Walls

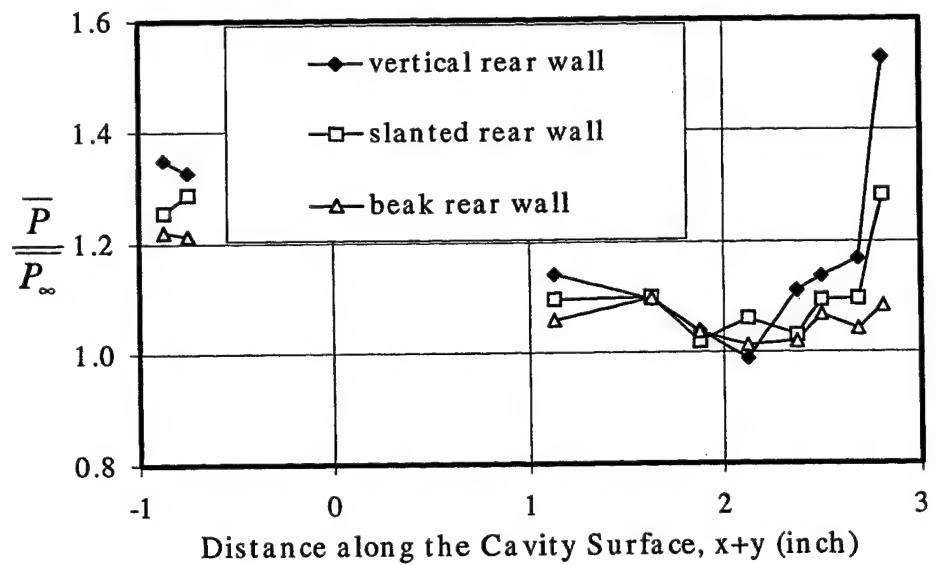
and "beak" rear walls. The two foci on the front cavity floor for the "beak" rear wall case move obviously closer to each other compared to the slanted and vertical rear wall cases. This means that the "beak", as designed, directs more impingement mass to both sides of the cavity that results in the movement of those two foci towards the

longitudinal centerline. Those two separation lines on both sides of the cavity floor are pushed closer to each other too.

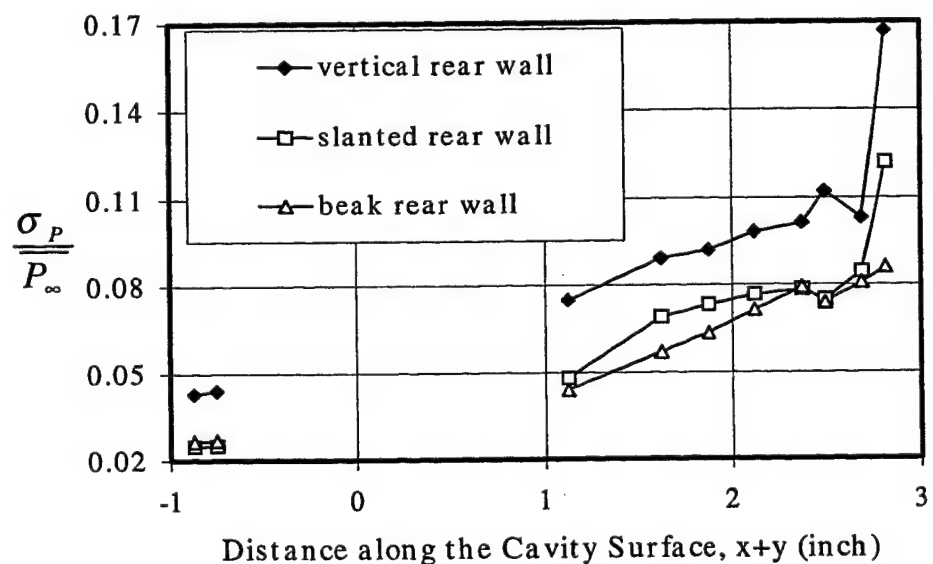
7.2 MEAN PRESSURE AND PRESSURE STANDARD DEVIATION

Because of the difficulty of instrumenting the slanted and “beak” rear walls, no transducer ports are available on these rear walls. The effectiveness of the slanted and “beak” rear walls at reducing the severity of the pressure environment inside the cavity is judged based on the measurements made on the cavity floor.

Figures 7.2(a) and (b) show the effects of the passive control rear walls on the mean pressure and σ_p distributions respectively for the store at $H/3$. Those for the store at $2H/3$ with the passive control rear walls are shown in Figures 7.3(a) and (b). Since the slanted and “beak” rear walls change the impingement angle of the shear layer on the rear wall, they result in a lower mass flow rate into the cavity compared to the vertical rear wall case. Figures 7.2 and 7.3 show that both rear walls are effective at reducing the mean pressure and σ_p values over most of the cavity surface as expected. This confirms that the energy of the pressure fluctuations inside the cavity is mainly provided by the incoming impingement flow. The “beak” rear wall improves on the performance of the slanted rear wall a little since it directs the impingement flow to both sides of the cavity where lower mean pressures occur in the spanwise direction of the cavity. These figures also show that the main pressure and σ_p reductions for both the slanted and “beak” rear wall cases are found near the rear corner. The reason might be that the slanted surfaces of these passive control rear walls move the re-compression positions of the impingement flow on the floor upstream as compared to the vertical rear wall case.

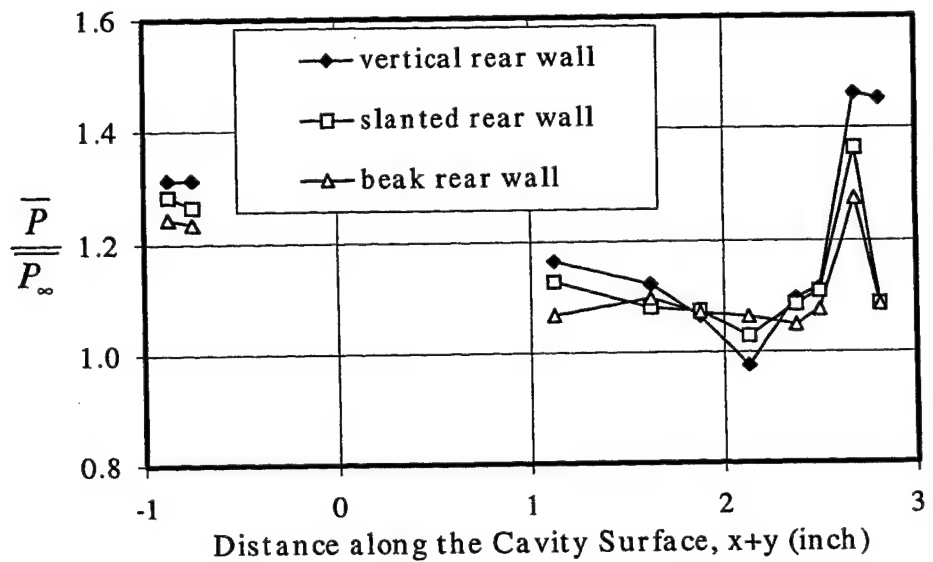


(a) Mean Pressure Distribution

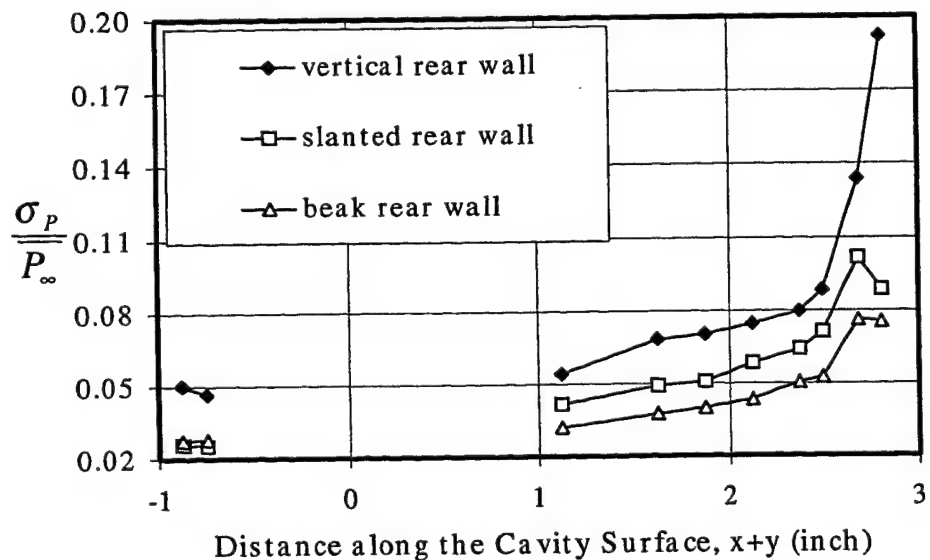


(b) Pressure Standard Deviation Distribution

Figure 7.2 Mean Pressure and Pressure Standard Deviation Distributions of the Cases with a Store at $H/3$ and Different Rear Walls



(a) Mean Pressure Distribution



(b) Pressure Standard Deviation Distribution

Figure 7.3 Mean Pressure and Pressure Standard Deviation Distributions of the Cases with a Store at $2H/3$ and Different Rear Walls

For the shock/cavity interaction cases, the same observations regarding the effectiveness of the slanted rear wall as those from the single store/cavity interaction experiment are obtained. The "beak" rear wall was not applied to these cases. Figure 7.4 shows the mean pressure distribution of the two cases with shock impingement and the slanted rear wall. In this figure, the mean pressure values on the front floor of the cases with the slanted rear wall rise sharply from FL4 to FL2 and then drop from FL2 to FL1 compared to their vertical rear wall cases. This is an indication of a weaker (and maybe smaller) trailing-edge vortex which results from a lower mass flow rate into the cavity.

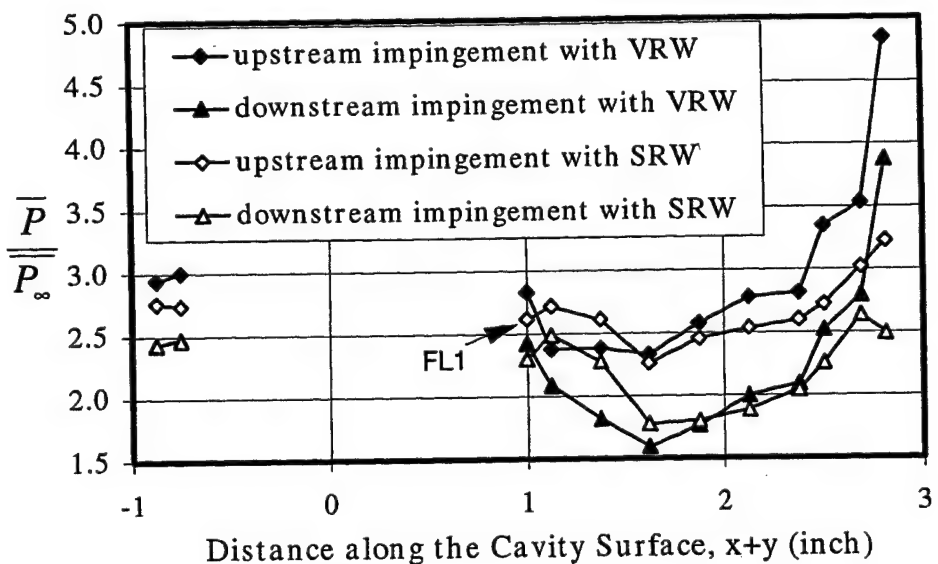


Figure 7.4 Mean Pressure Distribution of the Cases with Shock Impingement and the Slanted Rear Wall

Table 7.1(a) lists the percentage reduction in the maximum mean pressure value on the cavity floor by using the slanted and "beak" rear walls for all the cases studied. The positions where the maximum mean pressures occur are also listed. The percentage reductions in the maximum σ_p value are listed in Table 7.1(b). From these

Table 7.1 Reduction in the Maximum Mean Pressure and σ_p Values
on the Cavity Floor Using Passive Control Rear Walls

(a) Reduction in the Maximum Mean Pressure Value

Case	Store at H/3	Store at 2H/3	Store in the shear layer	Shock Impingement		
				Leading edge	Upstream	Down- stream
Port experienced \bar{P}_{\max} , vertical rear wall	FL10	FL9	FL10	FL10	FL10	FL10
Reduction by the slanted rear wall and where \bar{P}_{\max} occurs	16% FL10	7% FL9	28% FL10	29% FL10	33% FL10	36% FL10
Reduction by the “beak” rear wall and where \bar{P}_{\max} occurs	29% FL4	13% FL9	25% FL10	-	-	-

(b) Reduction in the Maximum σ_p Value

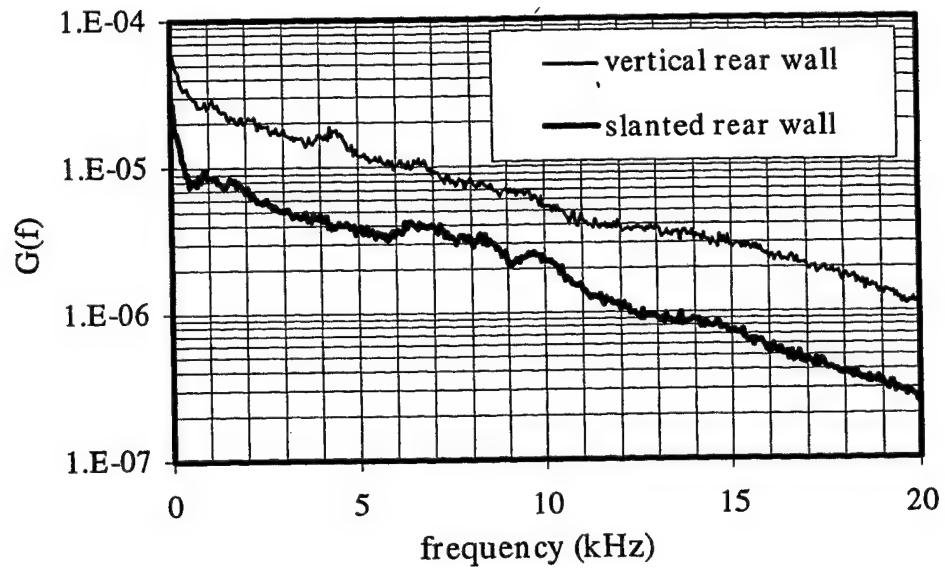
Case	Store at H/3	Store at 2H/3	Store in the shear layer	Shock Impingement		
				Leading edge	Upstream	Down- stream
Port experienced $\sigma_{p,\max}$, vertical rear wall	FL10	FL10	FL10	FL10	FL10	FL10
Reduction by the slanted rear wall and where $\sigma_{p,\max}$ occurs	27% FL10	47% FL9	43% FL7	39% FL10	37% FL10	18% FL10
Reduction by the “beak” rear wall and where $\sigma_{p,\max}$ occurs	49% FL10	60% FL9	39% FL9	-	-	-

tables, the maximum mean pressure and σ_p values tend to occur at the same port for different rear walls. The maximum percentage reductions by the slanted and "beak" rear walls are 7% and 13% respectively in the maximum mean pressure value and are 18% and 39% respectively in the maximum σ_p value. The reduction rates for the worst case during store-release, i.e., the "store in the shear layer" case, are very large with values of 28% and 25% in the maximum mean pressure by using the slanted and "beak" rear walls respectively and 43% and 39% in the maximum σ_p value by the slanted and "beak" rear walls respectively.

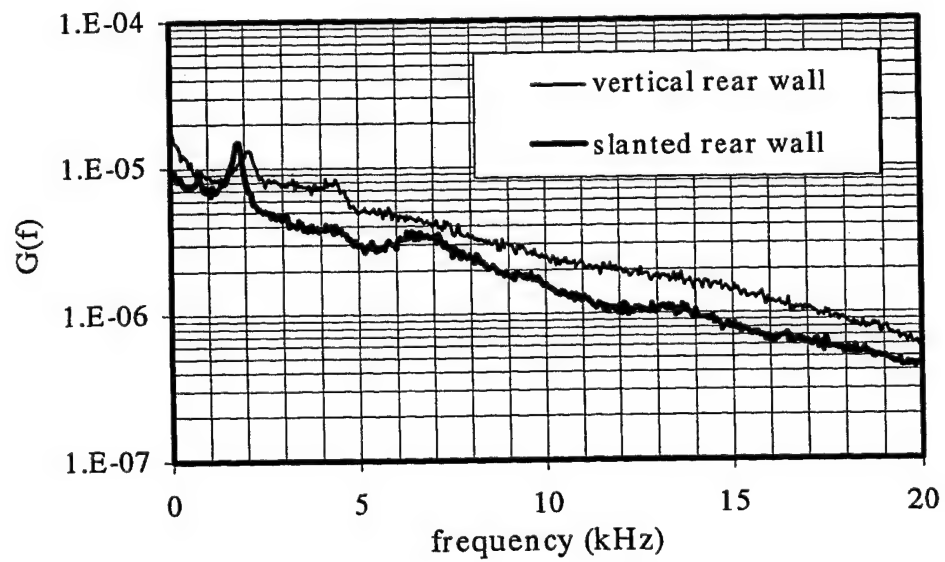
7.3 POWER SPECTRA

The effects of the slanted rear wall on the power spectra for the cases with upstream and downstream shock impingement are shown in Figures 7.5(a) and (b) respectively. The power spectra were measured at FL10. The performance of the slanted rear wall is better for the case with upstream shock impingement than for the case with downstream impingement. For the latter case, the slanted rear wall actually amplifies the 1st mode a little. No satisfactory explanation is available for this result.

Figures 7.6(a) and (b) show the effects of the slanted and "beak" rear walls on the power spectra for the cases with a store at $H/3$ or $2H/3$ respectively. The power spectra are obtained at FL10 too. From Figure 7.6, these passive control rear walls reduce not only the power levels of the mode frequencies but also that of the background noise. The performance of the "beak" rear wall is again better than that of the slanted rear wall. Since the nominal lengths of the cavity with these passive control rear walls are longer (because the shear layer stagnation points are further downstream on the rear wall) than that with the vertical rear wall, the mode frequencies are shifted to lower values for these passive control rear wall cases. Figure 7.6 also shows that these passive control rear walls make several higher modes more obvious. The possible reason is that these rear walls reduce the

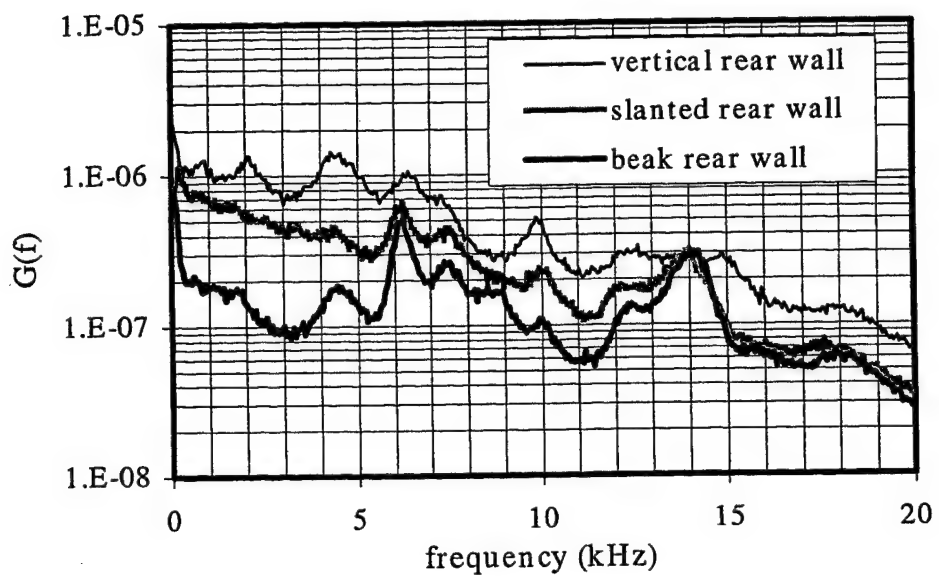


(a) The Cases with Upstream Shock Impingement and Different Rear Walls

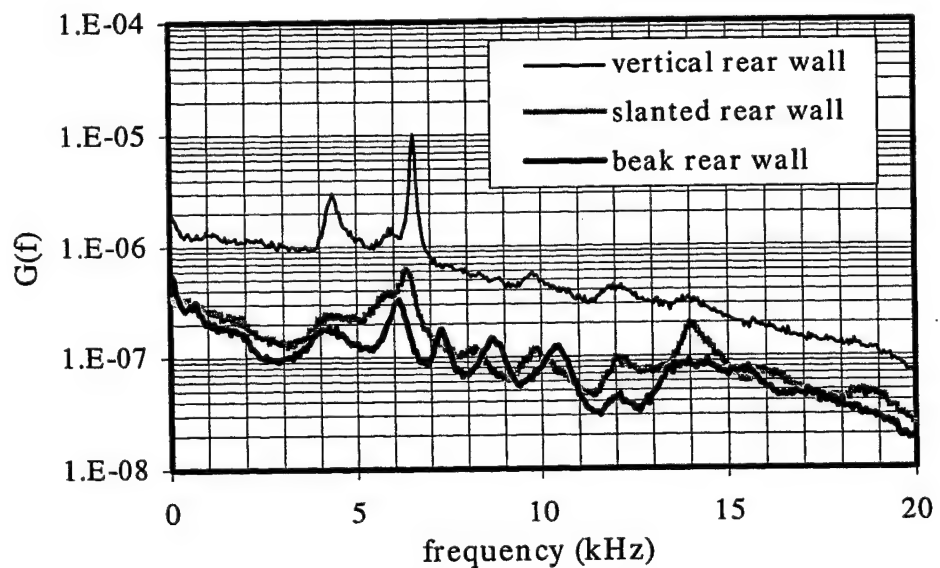


(b) The Cases with Downstream Shock Impingement and Different Rear Walls

Figure 7.5 Power Spectra at FL10 of the Cases with Shock Impingement and Different Rear Walls



(a) The Cases with a Store at $H/3$ and Different Rear Walls



(b) The Cases with a Store at $2H/3$ and Different Rear Walls

Figure 7.6 Power Spectra at FL10 of the Cases with a Store and Different Rear Walls

impingement mass flow rate into the cavity, thus increasing the signal-to-noise ratio of the acoustic waves inside the cavity and rendering the higher modes more obvious. However, the reason for the appearance of the peak frequency at 7.3 kHz and the frequency shift to higher values of its subsequent two modes for the case with a store at 2H/3 and the “beak” rear wall (Figure 7.6(b)) is not known.

Table 7.2 lists the reduction factors of the power spectral levels by using these passive control rear walls. The factor is evaluated from the dominant mode with the maximum power spectral level on the floor and is defined as the ratio of the power spectral levels of the vertical rear wall case to the passive control rear wall case. The experimental results show that no matter which rear wall is used, the maximum power level of the dominant mode on the cavity floor occurs at FL10, i.e., the port nearest to the rear corner. From this table, the dominant frequency might change to another mode from that of the “empty cavity” flow by applying these passive control rear walls. The slanted and “beak” rear walls are generally both effective at reducing the pressure fluctuations inside the cavity although the slanted rear wall increases the fluctuating pressure level of the 1st mode frequency a little for the case with downstream shock impingement as shown in Figure 7.5(b). The reduction factors for the case with a store at 2H/3, which is one of the worst cases during store-release, are about 16 and 31 by using the slanted and “beak” rear wall respectively. Compared to Perng’s (1996) results which showed that the reduction factors for the “empty cavity” case are 2.6 and 3.5 using the slanted and “beak” rear walls respectively, the current results for “disturbed” flowfield are encouraging.

Although these passive control rear walls are shown to be quite effective in reducing the maximum mean pressure and σ_p values and the power spectral level on the cavity floor, it should be expected that the reduction is effective anywhere inside the cavity due to the decrease of the entrainment mass flow rate into the cavity. However, this may not be true near the upper edge of the rear wall. That is because

the mass flow rate through the upper portion (above the mean impingement line) of the rear wall is increased compared to the corresponding vertical rear wall case.

Table 7.2 Reduction of the Power Spectral Level of the Dominant Mode
Obtained at FL10 by Using Passive Control Rear Walls

Dominant frequency (kHz)	Store at H/3	Store at 2H/3	Store in the shear layer	Shock Impingement		
				Leading edge	Upstream	Down-stream
Vertical rear wall, A	4.30 (f_2)	6.54 (f_3)	2.05 (f_1)	4.30 (f_2)	4.25 (f_2)	2.10 (f_1)
Slanted rear wall, B	6.20 (f_3)	6.35 (f_3)	x	x	x	1.81 (f_1)
“Beak” rear wall, C	6.25 (f_3)	6.15 (f_3)				
Power spectral level A/B	2.1	16.3	3.9	4.3	2.6	0.9
Power spectral level A/C	2.6	31.0				

Note: “x” means that the power spectra do not have an obvious peak or the amplitude of the dominant mode is small compared to that of the maximum background noise above 2 kHz. If it is the case, the maximum power spectral level of the background noise above 2 kHz is picked to judge the effectiveness of the passive control rear walls.

7.4 SUMMARIZING REMARKS

The slanted and “beak” rear walls are effective at attenuating the severe pressure environment inside the cavity as shown from either the reductions of the maximum mean pressure and pressure standard deviation or the suppression of the maximum power spectral level of the dominant mode. They worked as expected since the similarity of the cavity flowfields with shock impingement or store-release to that of the “empty cavity” flow is known. Thus, control techniques developed for the

“empty cavity” flow are also effective at improving the pressure environment inside the cavity for cavity flows with shock impingement or store-release.

Chapter 8: Concluding Remarks

The primary objectives of this experimental investigation, which was carried out in a Mach 5 wind tunnel, were: (i) understand the flow structure and dynamics of the Mach 5 "baseline" cavity flow and explore the effectiveness of passive control techniques (front and rear wall geometry changes) on attenuating the amplitude of the cavity pressure oscillations. (ii) determine how the flow structure and feedback process in an empty cavity flow is altered by the presence of generic store on the cavity centerline or by the impingement of a 2-D shock wave, and determine how effective are the passive control techniques developed for the empty cavity flow when the cavity flow is perturbed by stores or shocks. The conclusions from the two phases are presented below.

(i) Cavity Vortex Structure

From pressure measurements and surface flow visualization it was found that all baseline cavity flows ($L/H = 3, 4, \& 5$) were 3-D and symmetric about the longitudinal centerline. Three vortices were recognized, namely, the weak front clockwise vortex, the large trailing-edge counterclockwise vortex, and the small rear corner vortex. A separation line/curve and a saddle (unstable) point were located about $L/3$ downstream of the FW. Away from the center line, two tornado-shape vortices were located near the FW with two stable foci symmetric about the center line. The tornado-shape vortices and the trailing-edge vortex generated this separation line/curve. Near the RW, the flow was dominated by the trailing-edge vortex.

In this study, two models of predicting the oscillation frequencies and effects of L , H , and L/H were examined. Heller and Bliss's model was judged to be better than Rossiter's model for predicting the oscillation frequencies. This provides some support for the view that the acoustic wave instead of the shedding vortex is the cause of the flow impingement event on the RW, although it must be stated that no definitive proof exists showing that the shedding-vortex model is incorrect. The number of the consecutive acoustic waves existing simultaneously

inside the cavity determined the number of the modes and the oscillation frequencies. For a longer cavity the acoustic wave needs more time to travel between the FW and the RW and the oscillation frequencies decrease. The growth of the shear layer disturbance was calculated. The high speed shear layer was very stable and the impingement/shock foot could only penetrate as deep as about 0.12 and 0.16 inches from the top of the RW for cavities with $L/H = 3$ and 4 ($H = 1$ inch) respectively. This penetration distance was also validated experimentally through conditional sampling analysis. Of the three parameters, L is the most important. It not only affects the strength of the pressure oscillations but also determines the oscillation frequencies. With increasing L , the increased shear layer penetration resulted in more impingement flow into the cavity which enhanced the oscillation strength. As L increased from 3 to 4 inches, the rms of the strongest oscillations on the cavity floor was increased by a factor of 3. The importance of the shear layer is that its impingement supplies the energy to sustain the pressure oscillations inside a cavity. The effects of H and L/H were overridden by the larger effects of L .

(ii) Pressure Oscillation Attenuation

Several passive control methods were tested. Changes in geometry were made to the FW, the RW, and the cavity floor. A 2-D vented wall, a 2-D slotted wall, three 2-D slanted walls, and two 3-D walls were tested to examine their effects on attenuating the strength of cavity flow oscillations. The slanted wall #3 and the wall base were also attached to the cavity floor in order to alter the shape of the trailing-edge vortex. Three Wheeler doublet vortex generators (VG's) and a full-span wedge were placed upstream of the cavity to act as spoilers and change the incoming shear-layer characteristics. One combination employing a VG spoiler and the wall base on the cavity floor was also tested. The results are summarized below:

- (a) FW geometry changes:** The vented and slotted FWs were ineffective for the case $L/H = 3$ ($H = 3$ inch). The possible reason is that the stable

compressible shear layer was excited by the irregular top edge of the slotted FW and the upstream porous surface of the vented FW.

- (b) **BL spoilers:** Both kinds of spoilers, the VG's and the wedge, enhanced the pressure oscillations in the cavity. The wedge enhanced the strongest mode on the cavity floor by a factor of 1.7. The VG's and the wedge enhanced the strongest mode on the RW by factors of 6.3 and 1.9 respectively.
- (c) **Internal obstacles:** Two obstacles were put on the cavity floor in order to alter the shape of the trailing-edge vortex for the case $L/H = 3$ ($H = 3$ inch). One obstacle was the wall base and the other one was the slanted wall #3. Of all obstacle methods, the case with the wall base in the middle of the cavity was the best. At the lowest point on the RW, the strongest mode of the baseline case was attenuated by a factor of 2.5. It suggests that not only the acoustic wave but also the trailing-edge vortex can affect the pressure oscillations inside the cavity.
- (d) **RW geometry changes:** For the RW controls, the 2-D vented, 2-D slotted, and 2-D slanted #1 RWs were judged ineffective. They could not effectively attenuate all modes and even enhanced some of them. The 3-D valley RW was more effective than the 2-D slanted RW1 but not by much. The slanted RW2 and RW3 worked well. They attenuated the strongest (the 3rd) mode of the baseline case $L/H = 3$ ($H = 1$ inch) by factors of 2.6 & 2.2 respectively. For the baseline case $L/H = 4$ ($H = 1$ inch), the 2-D slanted RW2 & RW3 attenuated the strongest (the 2nd) mode of the baseline case by factors of 5.5 & 6.4 respectively. Of the 3 slanted RWs, the #3 was the most effective. Of all RW controls, the beak RW was found to be most effective. This geometry attenuated the strongest oscillations by factors of 3.5 & 6.8 compared to the baseline cavity with $L/H = 3$ & 4 respectively.

(iii) Shock Impingement/Store Release

The most important conclusion from this experiment is that the gross features of the empty cavity flowfield (the mean flowfield and the oscillation mode frequencies) are not changed with shock impingement or store-release. No matter where the shock wave impinges on the cavity, no matter where the store is located and what its dimensions are, and even at a large store-to-cavity volume ratio or for asymmetric double store/cavity configurations, the basic mean flow structure and the oscillation mode frequencies of the cavity flow are not changed. These results are inferred from the similarities of the mean pressure and σ_p distributions and the surface flow patterns for all cases for the mean flow, and the nearly unchanged mode frequencies in the power spectra for the dynamics flowfield.

The similarity between the empty and "perturbed" cavity flows implies that the control techniques developed for the empty cavity flow should also be effective on the "perturbed" cavity flows, i.e., the cavity flows with shock impingement or store-release. This inference has been confirmed by applying two passive control rear walls (the slanted and "beak" rear walls) to the "perturbed" cavity flows. They successfully reduced the power spectral level of the dominant mode frequency and the maximum mean pressure and σ_p values on the cavity surface. Some of the reductions for the "perturbed" cavity flows are even larger than for the empty cavity flow.

a) Shock/Cavity Interaction

The mean pressure and σ_p values, and the power spectral levels of the mode frequencies and background noise increase as the shock impingement position moves upstream. Due to the pressure difference caused by the shock impingement, a more upstream shock impingement position results in a larger (though not by much) trailing-edge vortex. This is inferred from the surface flow patterns on the cavity floor.

b) Single Store/Cavity Interaction

During store release the most severe fluctuating pressure environment inside the cavity occurs when the store is in the shear layer or is in the free stream and a shock wave impinges on the cavity. Both the maximum mean pressure and σ_p values, and the maximum power spectral level of the modes inside the cavity are much higher than those when the store is "inside" the cavity. In this experiment the maximum mean pressure and σ_p values are as high as $3.07 \bar{P}_\infty$ and $0.58 \bar{P}_\infty$ respectively when the store is in the shear layer. However, if a store at a medium store-to-cavity volume ratio is located at the opening of the cavity, the 3rd mode frequency is amplified significantly and is comparable to that of the dominant mode of the "store in the shear layer" case.

c) Effects of the Store Dimensions

The store dimensions have little effect on the cavity flow as seen in the mean pressure and σ_p distributions on the cavity surface and the power spectra except when the store-to-cavity volume ratio is large. A relatively large store (compared to the cavity) located "inside" the cavity reduces both the power spectral levels of the mode frequencies and the σ_p values inside the cavity, but not the maximum mean pressure value. The mode frequencies are shifted to slightly lower values at a large store-to-cavity volume ration.

d) Double Store/Cavity Interaction

With an off-centerline store in the cavity alone, the maximum mean pressure and σ_p values are higher than those of its corresponding store-on-the-centerline configuration.

With double stores in the cavity and the centerline store in release, the maximum mean pressure and σ_p values, and the maximum power spectral level of the cavity pressure fluctuations still occur when the centerline store is in the shear layer or in the freestream as for the single

store/cavity configuration. However, these values are about the same as those from the single store on the centerline and in release configurations. No trend in the mean pressure and σ_p values and the maximum power spectral level in the spanwise direction of the cavity was found for these asymmetric store configurations.

References

Barter, J. W., "Prediction and Passive Control of Fluctuating Pressure Loads Produced by Shock-Induced Turbulent Boundary Layer Separation," Ph. D. Dissertation, Department of Aerospace Engineering, University of Texas at Austin, December 1995.

Baysal, O., Yen, G-W, and Fouladi, K., "Navier-Stokes Computations of Cavity Aeroacoustics with Suppression Devices," J. Vibration and Acoustics, Vol. 116, Jan. 1994, pp. 105-112.

Clark, R. L., Kaufman II, L. G., and Maciulaitis, A., "Aeroacoustic Measurements for Mach .6 to 3.0 Flows Past Rectangular Cavities" AIAA Paper, 80-0036, 1980.

Franke, M. E. and Carr, D. L., "Effect of Geometry on Open Cavity Flow-Induced Pressure Oscillations," Air Force Institute of Technology, Ohio, 1976.

Heller, H. H. and Bliss, D. B., "Aerodynamically Induced Pressure Oscillations in Cavities : Physical Mechanisms and Suppression Concepts," AFFDL-TM-74-79-FYA, 1974.

Leu, Y.L., "Experimental Study of Perturbed High Speed Cavity Flow", Ph.D. dissertation, Dept. of Aerospace Engineering and Engineering Mechanics, The University of Texas at Austin, Austin, TX Dec. 1997.

Leu, Y.L., and Dolling, D.S., "Passive Control of Pressure Oscillations in Cavity Flow with Store Release," paper No. 15, CEAS European Forum on Wind Tunnels and Wind Tunnel Test Techniques, Cambridge, UK,. April 14-16, 1997.

Maurer, O. F., "Investigation and Reduction of Open Weapon Bay Pressure Oscillations Expected in the B-1 Aircraft," AFFDL TM 74-101, 1973.

Morgenstern, Jr. A. and Chokani, N., "Hypersonic Flow Past Open Cavities," AIAA Paper, 93-2969, 1993.

Morgenstern, Jr. A. and Chokani, N., "Computation of Hypersonic Flow Over Three-Dimensional Cavities," AIAA Paper, 94-0631, January 1994.

Papamoschou, D. and Roshko, A., "The Compressible Turbulent Shear Layer: An Experimental Study," J. Fluid Mech., Vol. 197, 1988, pp. 453-477.

Pearcey, H. H., "Shock-Induced Separation and Its Prevention by Design and Boundary Layer Control," Boundary Layer and Flow Control: Its Principles and Applications, Vol. 2, edited by G. V. Lachman, Pergamon Press, Inc., New York, 1961.

Perng, S.W., "Passive Control of Pressure Oscillations in Hypersonic Cavity Flow," Ph.D. Dissertation, Dept. of Aerospace Engineering and Engineering Mechanics, The University of Texas at Austin, Austin, TX, Dec. 1996.

Perng, S.W., and Dolling, D.S., "Attenuation of Pressure Oscillations in High Speed Cavity Flow through Geometry Changes," AIAA paper 97-1802, 28th Fluid Dynamics Conference, Snowmass, CO, June 20-July 2, 1997.

Perng, S. W. and Dolling, D. S., "Passive Control of Pressure Oscillations in Hypersonic Cavity Flow," AIAA Paper, 96-0444, January, 1996.

Rizzetta, D. P., "Numerical Simulation of Supersonic Flow Over a Three-Dimensional Cavity," AIAA Journal, Vol. 26, 1988, pp. 799-807.

Rockwell, D. and Knisely, C., "The Organized Nature of Flow Impingement upon a Corner," J. Fluid Mech., Vol. 93, 1979, pp. 413-432.

Rossiter, J. E. "Wind-Tunnel Experiments on the Flow Over Rectangular Cavities at Subsonic and Transonic Speeds," A. R. C. R. & M., No. 3438, 1964.

Shaw, L. L., Clark, R., and Talmadge, D., "F-111 Generic Weapons Bay Acoustic Environment," J. Aircraft, Vol. 25, Feb., 1988, pp. 147-153.

Smith, R. A., Gutmark, E., and Schadow, K. C., "Mitigation of Pressure Oscillations Induced by Supersonic Flow Over Slender Cavities," AIAA Paper, 90-4019, 1990.

Stallings, Jr. R. L., and Wilcox, F. J. Jr., "Experimental Cavity Pressure Distributions at Supersonic Speeds," NASA TP-2683, 1987.

Suhs, N. E., "Computational of 3-D Cavity Flow at Subsonic and Supersonic Mach Numbers," AIAA Paper, 87-1208, 1987.

Tam, C. K. W. and Block, P. J. W., "On the Tones and Pressure Oscillations Induced by Flow Over Rectangular Cavities," J. Fluid Mech., Vol. 89, part 2, 1978, pp. 373-399.

Tam, C-J, Orkwis, P. D., and Disimile, P. J., "Supersonic Open Cavity Flow Physics Ascertained from Algebraic Turbulence Model Simulations," AIAA Paper, 96-0075, 1996.

Zhang, X., "An Experimental and Computational Investigation into Supersonic Shear Layer Driven Single and Multiple Cavity Flowfields," Ph.D. Dissertation, Department of Engineering, University of Cambridge, 1987.

Zhang, X. and Edwards, J. A., "Computational Analysis of Unsteady Supersonic Cavity Flows Driven by Thick Shear Layers," Aeronautical J., 1988, pp. 365-374.

Zhang, X. and Edwards, J. A., "An Investigation of Supersonic Oscillatory Cavity Flows Driven by Thick Shear Layers," Aeronautical J., 1990, pp. 355-364.

Zhang, X. and Edwards, J. A., "Experimental Investigation of Supersonic Flow over Two Cavities in Tandem," AIAA Journal, Vol. 30, 1992, pp. 1182-1190.